Dublin City University

Ultrafast and intense laser interaction with gases and solids

Submitted for the degree of:
DOCTOR OF PHILOSOPHY

Presented to:
School of Physical Sciences

Submitted by
Mossy Kelly

Research Supervisor
Prof. John T Costello

July 2013

Declaration

I hereby certify that this material, which I now submit for assessment on the programme of study leading to the award of Doctor of Philosophy is entirely my own work, that I have exercised reasonable care to ensure that the work is original, and does not to the best of my knowledge breach any law of copyright, and has not been taken from the work of others save and to the extent that such work has been cited and acknowledged within the text of my work.

Signed: _____

ID No.: 54406567

Date: _____

Abstract

A dedicated laboratory has been built in DCU to study the interaction between ultra-short, intense laser radiation with both solid and gaseous materials.

A commercial laser system with high intensity (3 mJ), and short temporal duration (32 fs) has been installed and characterised as part of this project. A static, single shot Nomarski interferometer has been developed and by exploiting the non-linear response of an optical filter, the pulse width of the laser has been measured.

The interaction with high intensity laser radiation with solid materials was also investigated. Experiments using a wire probe to characterise a silicon laser produced plasma were performed. The emission of ions and electrons within the laser plasma as well as the angular distribution of both species has been measured and the effects of laser intensity, laser wavelength and laser polarisation are investigated. In a complementary experiment, the expansion dynamics of the laser plasma are studied with space resolved Langmuir probe measurements. These results are analysed and presented in the context of double layer formations within the plasma plume.

A Wiley-McLaren spectrometer has been built to study the interaction of high intensity laser light with gas jets. The design and construction of the spectrometer is detailed as well as its characterisation. The effects of polarisation are studied with molecular nitrogen as a gas target.

Contents

List of Figures

Chapter 1

Introduction, motivation and structure of thesis

The laser plasma research group is a node of the National Centre of Plasma Science and Technology (NCPST). The group has, for a long time, been involved in studying the physics of the interaction of high powered laser light with matter. However, to date, most of the in house work of the group has focussed on laser pulses of high average power with relatively long durations ($\approx$ 200 ps - 10 ns) [1]. Any work done using high powered lasers of short duration has been completed off site at other research facilities [2, 3]. This thesis is concerned with the first experiments to be performed with a femtosecond laser system now available at DCU.

The work that is presented in this thesis involved the construction of a new experimental laboratory which aims to extend the current research activities of the laser plasma group namely, laser plasma light sources, diagnostics and spectroscopy at DCU and photoionization in intense free electron laser fields at apposite international facilities. The benefits and new opportunities that this laser lab presents, and the motivation behind the work in this thesis are outlined in this chapter:

1.0.1 Ultrafast laser experiments

'Ultrafast Laser' is defined here as a laser whose output pulses are less than 100×10^{-15} s in duration. In 2008, a Coherent Legend Elite Amplifier system was purchased in a collaboration between the National Centre for Plasma Science and Technology (NCPST) and the Research Institute for Network and Communication Engineering (RINCE) research centres in DCU. The DCU amplifier system consists of an oscillator which produces 30 fs pulses with a pulse energy of 42 nJ at 80 MHz repetition rate. This is used to seed a regenerative amplifier (RGA) which produces 35 fs laser pulses at a repetition rate of 1 kHz with 3.5 mJ/pulse energy. The system has been used in three specific projects namely, (a) in the development of an ultrashort pulse measurement technique akin to autocorrelation, (b) in laser plasma generation on silicon surfaces and in the characterisation of a time-of-flight spectrometer for future studies with gaseous targets. These motivations for these studies are summarised below.

1.0.2 Pulse characterisation

The use of interferometric techniques in the laser plasma group has, to date, been confined to the estimation of electron densities at early times of a plasma plume's evolution [4]. Here, the 'Nomarski Interferometry' technique was used in conjunction with a phase retrieval technique based on the continuous wavelet transform to estimate the two dimensional electron density of a laser plasma plume as a function of time.

An ultrafast (femtosecond) laser pulse cannot be characterised by the same means as a long pulse (nanosecond) laser (i.e., by using a fast photodiode). Other means must then be used to determine the pulse width and phase of the laser pulse. In the latter part of Chapter Two, the interferometry principle was adapted to measure the autocorrelation of a femtosecond laser beam. The technique exploited the non-linear interaction of a femtosecond laser beam with a silicon Complementary Metal Oxide Semiconductor (CMOS) chip which contains an infra-red blocking filter. Nomarski

Interferometry uses a Wollaston prism to create a spatially dependent time delay between a replica of a laser pulse with itself. In the setup presented in Chapter Two, this interference pattern is imaged onto a CMOS detector and there is evidence of a non-linear interaction in the detector itself. In this way, the device is used as an interferometric autocorrelator. At the time or writing, to the author's knowledge, there is no published record of a device which measures the pulse width in this way and so this appears to be a new technique

1.0.3 Laser-solid interactions

The DCU femtosecond laser system allows for the study of a whole new aspect of laser-solid interaction. Because the system produces pulses whose temporal duration is shorter than the typical electron-phonon coupling time in most solidsm, the resulting plasma formation and evolution is much different the long pulse counterpart [6]. The intensities achievable with the DCU system allow for electrons to be heated to far above the Fermi energy causing space charge layers to form.

Secondly, the main focus of the laser plasma research in DCU has traditionally focussed on optical diagnostic techniques such as interferometry [4], fast imaging [1], shadowgraphy [7] and spectroscopy [8]. In recent years, there has been some work done on diagnosing plasmas with electrical techniques such as Faraday cups [9].

In Chapter Three, ultrafast laser ablation of silicon is studied using the Langmuir probe technique. It is found that the plasma plume is comprised of a bi-modal structure likely arising from the creation of space charge layers within the plume. The bi-modal structure consists of a high kinetic energy (KE) peak followed at a later time by a broader peak. Fluence measurements reveal that the broad low KE peak is thermal in nature and the high KE peak is non thermal in nature. The low and high KE components of the ions are found to have the same angular distribution. However, the low KE and high KE electron signals show different angular behaviour

namely: the high KE electron signal has a narrower angular distribution. This result is interpreted in the context of different expansion mechanisms for each component of the bi-modal structure. The polarisation dependence of the Si ions is found to vary in a cosinusoidal pattern as one rotates the electric field vector of the laser field from S to P polarisation with respect to the target surface. An unusual shaped pattern is found for the polarisation of the electrons and this is interpreted as being due to resonantly excited electrostatic fields arising in the plume due to resonant absorption.

Finally, estimates of the electron temperature and density are made for a variety of experimental conditions and evidence of double layer formation is found. The appearance of two distinct electron populations simultaneously is interpreted as the existence of a rarefaction shockwave inside the plasma plume. Thus, it is concluded that the bi-modal structure of the plume is due to the violation of quasi-neutrality in the plume over large distances.

1.0.4 Photoionization

The main focus of photoionization studies at DCU has been, to date, on plasma based, table-top XUV sources [10], synchrotron and free electron laser (FELs) [11], [12]. Because the DCU femtosecond laser system can provide intensities on the order of 10^{14} Wcm^2, it can be comparable the Coulombic force between electrons and their nucleus in an atom. Therefore, the laser can be used to directly ionize dilute gaseous samples. One way of studying these ionization processes is by time-of-flight mass spectrometry (TOF-MS). The TOF-MS technique has been used in-house within the laser plasma group before but only on laser-solid interaction [13] using relatively long pulse lasers.

The subject of Chapter Four is the construction of a linear TOF-MS and its use in detecting the ions produced by Coulomb explosion of an ionized nitrogen molecule (pathway: $N_2^{(p+q)+} \rightarrow N^{p+} + N^{q+}$). The angular distribution of these signals are measured and compared directly to previous results taken under similar experimen-

tal conditions [14]. The measured data are found to agree quite well with the previous results and the detector is then concluded to be a useful tool in the extension of the photoionization and TOF-MS work already conducted at DCU [9].

The novelty of this work is as follows: In chapter two, a device for measuring ultrashort pulse widths is described. This device is unique in its optical design and represents a very simple alternative to other measurement devices. Chapter three represents the first detailed study of an ultrafast laser plasma plume with a Langmuir probe. The results presented are compared conceptually to high fluence long pulse laser data. This interpretation is novel and explains a high kinetic energy peak in the time of flight distributions which has been under significant debate in the recent past. Finally, this work presents the first polarisation dependencies of ion and electron emission from an ablated silicon target. The results and consequent interpretation are novel for the experimental parameters used in this work.

Bibliography

[1] H. Luna and J. Dardis and D. Doria and J.T. Costello. Analysis of time-resolved laser plasma ablation using an imaging spectra technique. *Brazilian Journal of Physics*, **37**(4):1301–1305, 2007.

[2] V. Richardson and W.B. Li and T.J. Kelly and J.T. Costello and L.A.A. Nikolopoulos and S. Duesterer and D. Cubaynes and M. Meyer. Dichroism in the above-threshold two-colour photoionization of singly charged neon. *Journal of Physics B-Atomic Molecular and Optical Physics*, **45**(8):085601, 2012.

[3] S. Duesterer and P. Radcliffe and C. Bostedt and J. Bozek and A.L. Cavalieri and R. Coffee and J.T. Costello and D. Cubaynes and L.F. DiMauro and Y. Ding and G. Doumy and F. Gruener and W. Helml and W. Schweinberger and R. Kienberger and A.R. Maier and M. Messerschmidt and V. Richardson and C. Roedig and T. Tschentscher and M. Meyer. Femtosecond x-ray pulse length characterization at the linac coherent light source free-electron laser. *New Journal of Physics*, **13**:093024, 2011.

[4] P. Hough and C. McLoughlin and T.J. Kelly and S.S. Harilal and J-P. Mosnier and J.T. Costello. Time resolved nomarski interferometery of laser produced plasma plumes. *Applied Surface Science*, **255**(10):5167–5171, 2009.

[5] P. Kockaert and M. Haelterman and P. Emplit and C. Froehly. Complete characterization of (ultra)short optical pulses using fast linear detectors. *Ieee Journal of Selected Topics in Quantum Electronics*, **10**(1):206–212, 2004.

[6] E.G. Gamaly. The physics of ultra-short laser interaction with solids at non-relativistic intensities. *Physics Reports-Review Section of Physics Letters*, **508**(4-5):91–243, 2011.

[7] P. Hough and T.J. Kelly and C. Fallon and C. McLoughlin and P. Hayden and E.T. Kennedy and J-P. Mosnier and S.S. Harilal and J.T. Costello. Enhanced shock wave detection sensitivity for laser-produced plasmas in low pressure ambient gases using interferometry. *Measurement Science and Technology*, **23**(12):125204, 2012.

[8] H. Luna and K.D. Kavanagh and J.T. Costello. Study of a colliding laser-produced plasma by analysis of time- and space-resolved image spectra. *Journal of Applied Physics*, **101**(3):033302, 2007.

[9] P. Yeates and J.T. Costello and E.T. Kennedy. The dcu laser ion source. *Review of Scientific Instruments*, **81**(4):043305, 2010.

[10] J.S. Hirsch and O. Meighan and J-P Mosnier and P. van Kampen and W.W. Whitty and J.T. Costello and C.L.S. Lewis and A.G. MacPhee and G.J. Hirst and J. Westhall and W. Shaikh. Vacuum-ultraviolet resonant photoabsorption imaging of laser produced plasmas. *Journal of Applied Physics*, **88**(9):4953–4960, 2000.

[11] C. Banahan and J.T. Costello and D. Kilbane and P. van Kampen. 4p-inner-shell and double-excitation spectrum of Sr II. *Physical Review A*, **79**(2):022509, 2009.

[12] T. Mazza and K.G. Papamihail and P. Radcliffe and W.B. Li and T.J. Kelly and J.T. Costello and S. Duesterer and P. Lambropoulos and M. Meyer. Controlling core hole relaxation dynamics via intense optical fields. *Journal of Physics B-Atomic Molecular and Optical Physics*, **45**(14):141001, 2012.

[13] P. Yeates and J.T. Costello and E.T. Kennedy. Charged particle dynamics in a 'high-pressure' laser ion source. *Journal of Physics D-Applied Physics*, **44**(13):135204, 2011.

[14] C.Y. Wu and H.Z. Ren and T.T. Liu and R. Ma and H. Yang and H.B. Jiang and Q.H. Gong. Field-induced ionization and coulomb explosion of nitrogen. *Applied Physics B-Lasers and Optics*, **75**(1):91–96, 2002.

Chapter 2

The ultrafast laser system

In this chapter, the basic theory of lasing is described and the operating principles of ultrafast laser systems are presented with particular emphasis on the laser system used in this work. Pulse measurement techniques are discussed and a detailed description of the mathematical principles of second order autocorrelation is given. The development of a compact autocorrelator is described. A two dimensional silicon detector with an infra-red filter in front of the sensor is shown to have a strong nonlinear response when exposed to modelocked radiation. This is then used as both the detector and nonlinear medium for measurment of the interferometric autocorrelation of an 80 MHz pulse train. A Nomarski-type interferometer is described using a Wollaston prism to create a spatially dependent path difference between two pulse replicas. It is shown that this optical configuration gives a reliable measurement of the interferometric autocorrelation of the laser pulse.

2.1 The principles of lasing

2.1.1 Conditions for lasing

Consider a two level atomic system interacting with a light source. The system has levels $|a>$ and $|b>$ such that $E_{|a>}$ is less than $E_{|b>}$. An electron may move between the two levels by either absorbing energy and moving from the lower state ($|a>$) to the upper state ($|b>$) or, the electron may lose energy and move from the upper state to the lower one. For example, the electron may be residing in the lower state and then absorb a photon whose energy is equal to the energy difference of the two levels. This will excite the electron into the upper state in a process known as stimulated absorption [1]. Once in the upper state, the electron can move back down to the lower state via two possible pathways. Firstly, the electron may simply spontaneously release energy in the form of a photon and then de-excite to the lower level. In this case, the emitted photon's properties (polarisation, direction, phase etc.) will follow a random distribution. Secondly, the electron may drop to a lower level by interacting with an external electromagnetic field in a process known as stimulated emission. It was postulated in the early days of quantum theory that these three processes were responsible for the formation of spectral lines [1].

In spontaneous emission, the electron will simply decay on its own accord to the lower state, releasing a photon with seemingly random properties. However, in stimulated emission, the electron is encouraged by the presence of an incoming photon (with a photon energy equal to the energy difference between the two levels) to decay to the lower state. In this case, the emitted photon will be an identical copy of the incoming photon. It is this optical replication which underpins the operation of a laser [2].

Each process can be described by a first order rate equation:

$$\left(\frac{dn_a}{dt}\right)_{abs} = -B_{ab}g(\nu)\rho(\nu)n_a \tag{2.1}$$

$$\left(\frac{dn_a}{dt}\right)_{stim} = B_{ba}g(\nu)\rho(\nu)n_b \tag{2.2}$$

$$\left(\frac{dn_a}{dt}\right)_{spon} = A_{ba}g(\nu)n_b \tag{2.3}$$

where:

- B_{ab} = Probability for stimulated absorption
- B_{ba} = Probability for stimulated emission
- A_{ba} = Probability for spontaneous emission
- $\rho(\nu)$ = Spectral power density
- $g(\nu)$ = Transition line shape
- n_a = Fractional population of $|a>$
- n_b = Fractional population of $|b>$

A_{ba}, B_{ba} and B_{ab} are known as the Einstein co-efficients and they depend only on the properties of the atom under consideration [1]. In the steady state, there is an equilibrium between the absorption and emission processes:

$$B_{ba}\rho(\nu)n_b + A_{ba}n_b - B_{ab}\rho(\nu)n_a = 0 \tag{2.4}$$

From Maxwell Boltzmann statistics [3],

$$\frac{n_b}{n_a} = \frac{g_b}{g_a}e^{-E_{ba}/kT} \tag{2.5}$$

Where E_{ba} is the energy difference between $|a>$ and $|b>$ in eV, kT is the temperature, also expressed in eV and g is the degeneracy of the particular energy

level (the number of states with the same energy). Planck's radiation law allows $\rho(\nu)$ to be defined [3].

$$\rho(\nu) = F(\nu)\frac{1}{e^{E_i/kT} - 1}, F(\nu) = \frac{8\pi h\nu^3}{c^3} \tag{2.6}$$

Setting $E_{ba} = h\nu$ and re-arranging gives:

$$A_{ba}(e^{-h\nu/kT} - 1)g_b + B_{ba}g_bF(\nu) = B_{ab}g_aF(\nu)e^{-h\nu/kT} \tag{2.7}$$

Because this result includes no assumptions as to the temperature, by setting $e^{-h\nu/kT} = 0$ and $e^{-h\nu/kT} = 1$ the following can be inferred;

$$\frac{A_{ba}}{B_{ba}} = F(\nu) \qquad \frac{B_{ba}}{B_{ab}} = \frac{g_a}{g_b} \tag{2.8}$$

If the two level system is a physical medium of length dz and cross sectional area dA, the energy lost and gained by the medium will be given by the relevant rate equations. Because the spontaneous emission radiates into a solid angle of 4π, one would expect the photon flux to be much lower than the stimulated flux. The temporal evolution of $|b>$ is then given by:

$$\frac{dn_b}{dt} = -B_{ba}g(\nu)\rho(\nu)\left(n_b - \frac{g_b}{g_a}n_a\right) \tag{2.9}$$

If a beam of intensity I falls on the medium, the beam will gain energy due to emission processes and lose energy due to absorption processes. The rate of change of the intensity as the beam propagates through the medium can be written as:

$$\frac{dI}{dz} = I \times \frac{dn_b}{dt} = -B_{21}g(\nu)\rho(\nu)\left(n_b - \frac{g_a}{g_b}n_a\right)I = \sigma I \tag{2.10}$$

which upon integration gives:

$$I = I_o e^{\sigma z} \tag{2.11}$$

It is seen then, that in order for amplification to occur, σ must be positive implying $n_b > \frac{g_a}{g_b} n_a$. Thus, in order for amplification to occur, the population of the upper state must be greater than the product of the ratio of the degeneracies times the population of the lower state. This is known as population inversion.

2.1.2 Population inversion

So far, the discussion has focussed on a two level atomic system. However, in practice it is inefficient to use an optically pumped two level system in a working laser because the rate of emission will be on the order of the rate of absorption meaning that the gains will be cancelled out by the losses. In practical laser systems, a multi level arrangement is used comprising typically of 3 or 4 levels [1].

In a three level system, three levels $|a>$, $|b>$ and $|c>$ are chosen such that $E_a < E_c < E_b$ (Figure 2.1). The system is then pumped by a resonant optical beam from $|a>$ to $|b>$. From $|b>$ the electrons undergo a fast radiationless transition to $|c>$ whose lifetime is much longer. Population inversion is then achieved between levels $|c>$ and $|a>$. For population inversion to be maintained in a three level system, the lifetime of $|c>$ must be much longer than the lifetime of $|b>$ such that the population of $|b>$ rapidly goes to zero while the population of $|c>$ does not. Secondly, over half the total population of electrons must be pumped into state $|c>$ in order to maintain population inversion between $|a>$ and $|c>$.

This requires a strong pumping mechanism and so a three level system contains drawbacks in terms of the amount of power required to pump the system. To circumvent these issues, a four level scheme is sometimes employed (Figure: 2.1.2). A four level system is arranged with four energy levels ($|a>, |b>, |c>$ and $|d>$) such that $E_{|a>}$ is less than $E_{|d>}$ which is less than $E_{|c>}$ which is less than $E_{|b>}$. Pumping occurs between levels $|a>$ and $|b>$. A fast radiationless transition occurs between

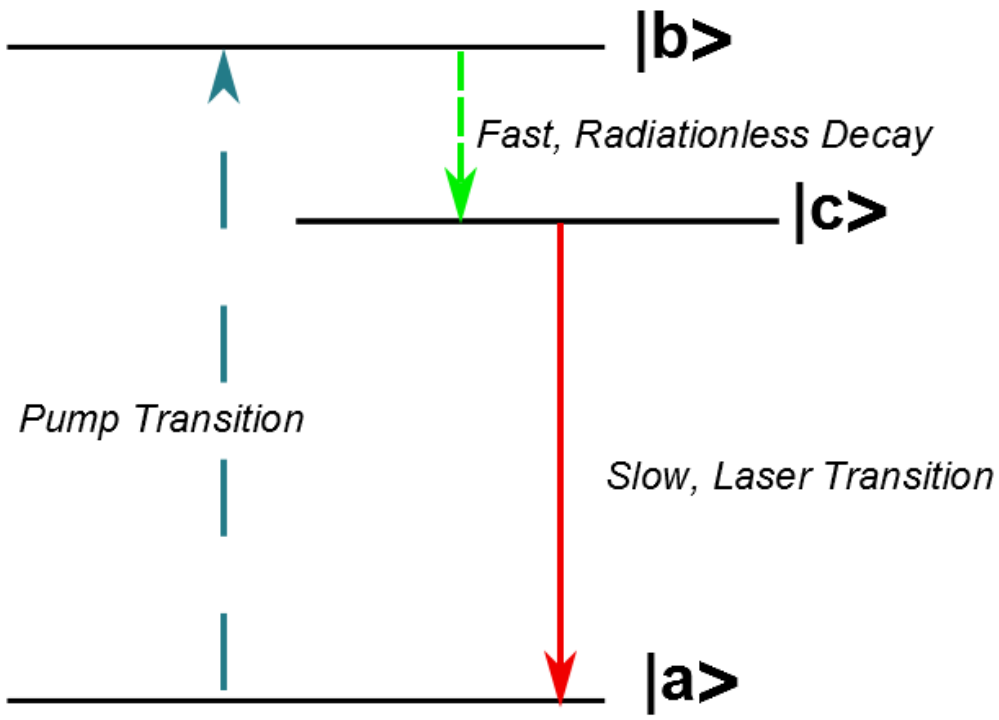

Figure 2.1: Graphical representation of a three level system.

$|b>$ and $|c>$. Population inversion is then achieved between $|c>$ and $|d>$. This eliminates the need for a strong pumping mechanism [1].

Once population inversion is achieved the stimulated emission process can begin. Normally, a set of two mirrors is used to form a cavity around the laser medium. This provides positive optical feedback which facilitates the amplification process. Exponential growth of the intensity cannot be maintained indefinitely and eventually the system will reach saturation. Operating the laser in the saturation region allows the laser beam intensity to remain reasonably stable even if the pumping source varies. Similarly, if the laser is seeded by an external source then operating in the saturation amplification regime will reduce sensitivity to fluctuations in the seed beam [1].

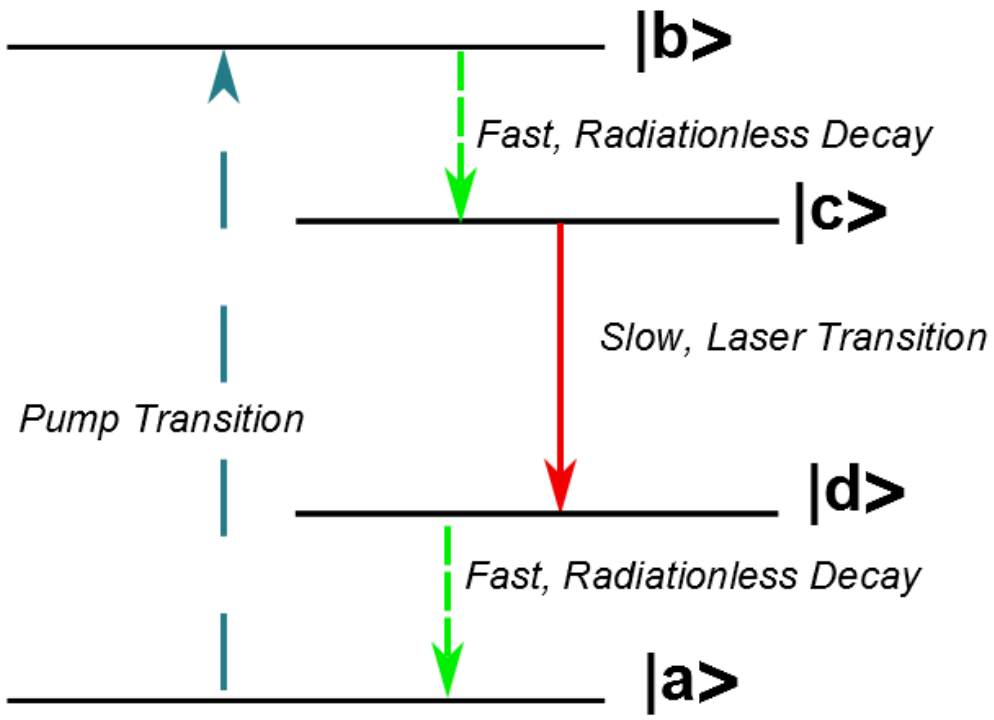

Figure 2.2: Graphical representation of a four level system.

2.2 Ultrafast laser operation

The stimulated emission process results in the production of photons which all share the same properties (i.e, photon replicas with the same frequency, phase and direction). It is with this in mind that the monochromaticity (and coherence) of lasers is championed as their most attractive features. In actual fact, the spectral emission of a laser can never be purely monochromatic. The laser will have a narrow but finite spectral width which is determined by the coherence length of the laser [1]. The relationship between the temporal and spectral profiles of the laser is governed by the well known Fourier relationship $\Delta\nu.\Delta t \geq 1$ where ν is the spectral bandwidth. This means that if a laser pulse is to be very short in time, then it must be very

broad in frequency or wavelength. Therefore, the production of short laser pulses requires a lasing medium capable of amplifying optical pulses over a broad spectral range. A sapphire crystal doped with titanium will allow for the amplification of any wavelength from 660 nm - 1180 nm which is theoretically enough to support a laser pulse as short as 0.2×10^{-15} s [4]. First constructed in 1982 [5], lasers which use Ti:Sapphire (as it is called) as its lasing medium are used to routinely produce laser pulses as short as 5×10^{-15} s or 5 fs [6]. The pumping scheme for a Ti:Sapphire laser is shown in Figure 2.3. A typical Ti:Sapphire laser is pumped by a green light source (usually a Nd:YAG or Nd:YLF laser) and will emit laser radiation with a centre wavelength of 800 nm and a broad spectral width. A laser pulse whose temporal width is the minimum that it can possibly be for a given spectral width is known as a bandwidth limited pulse (BLP) or a Fourier transform limited pulse (FTLP). It is in this situation that the entire laser pulse will have a constant phase difference across all the frequency components. The transform limited pulse width can be calculated from its spectral width by the 'Time-Bandwidth Product' [4] which can be written as:

$$\Delta\nu\Delta t = \alpha \tag{2.12}$$

where alpha is a line-shape dependent parameter. For a Gaussian shaped laser pulse, $\alpha = 0.44$ [4]. This means that a laser pulse of wavelength 800 nm, with spectral width 30 nm can have a minimum pulse duration of 31 fs.

There is an additional concern when attempting to produce ultrashort pulses of moderately high average power. With the exception of perhaps a free electron laser, lasing media can only sustain a certain amount of power before becoming damaged. A short laser pulse will have a very high peak power leading to damage of the crystal. Ti:Sapphire has a damage threshold of $8-10$ J/cm^2 which is relatively high, however it is still too low to amplify short pulses to a high power. To circumvent this issue, the technique of Chirped Pulse Amplification is used [4]. The next section will describe in detail the standard process for generating and amplifiying laser pulses of short

duration. Particular emphasis will be placed upon describing the laser system used in this work.

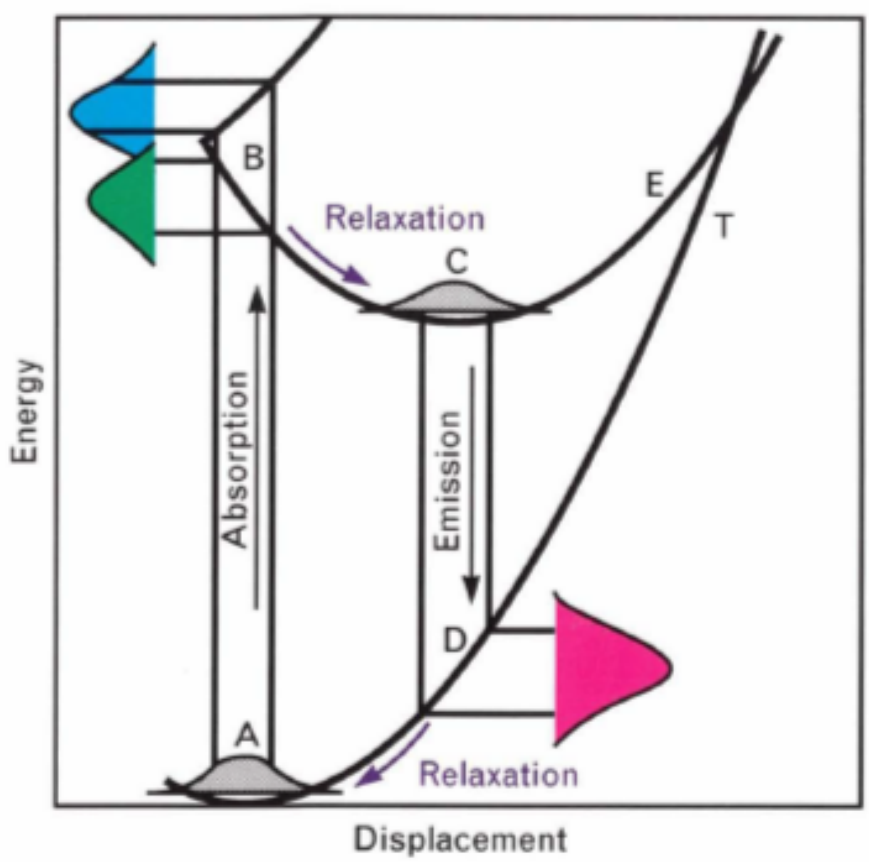

Figure 2.3: Graphical representation of the pumping scheme for a Ti:Sapphire laser. The pump transition (A - B) is achieved with a green light source and the lasing transition occurs from C-D. Image taken from [7]

2.2.1 The Micra oscillator

The first part of the DCU ultrafast laser system is the oscillator which produces the femtosecond laser pulses at low intensity. The pulses are then amplified by other parts of the laser system. The oscillator used in this work is shown in Figure 2.4.

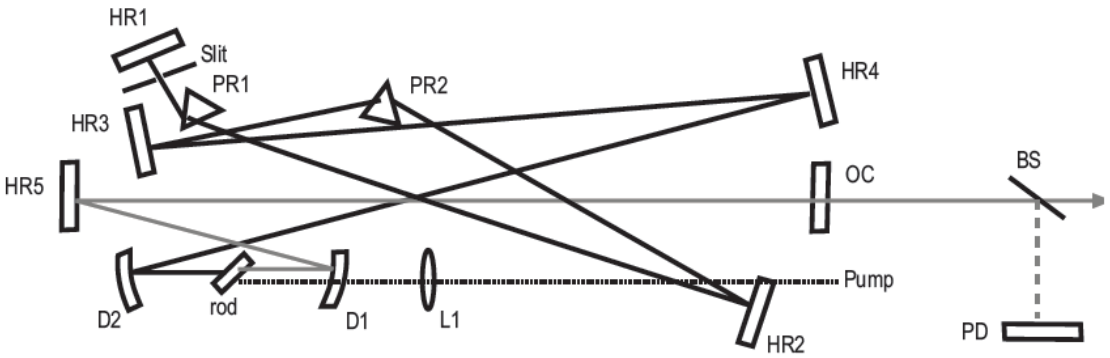

Figure 2.4: Schematic of the oscillator at DCU. Image taken from [8]

The DCU system uses a Coherent Micra 5 Oscillator pumped by a Verdi-18 Nd:YLF continuous wave laser (operated at 4.5 W, 527 nm). The oscillator produces 0.5 W output power at a repetition rate of 80 MHz. The output pulses have a bandwidth of $\sim$ 100 nm and a centre wavelength of 800 nm. Light in the oscillator is then allowed to pass back and forth between HR1 and OC (see Figure 2.4) and each round trip the beam passes through the gain material. This sets up a stable laser cavity which will only allow longitudinal modes satisfying the relation:

$$\nu = \frac{nc}{2L} \tag{2.13}$$

where n is an integer, c is the speed of light and L is the optical path of the cavity

[1]. The only modes which will be amplified however are those whose frequency lies within the amplification bandwidth of the Ti:Sapphire crystal. The cavity length in the DCU oscillator is roughly one meter long which leads to a round trip time of ≈ 12 ns giving a repetition rate of 80 MHz. Having a cavity which amplifies a wide range of frequencies however does not necessarily produce ultrashort pulses. If there is a random phase difference between each mode, the laser will operate in a state of continuous wave lasing [4]. In order to fix the phase difference between each mode, a process known as 'Kerr lens modelocking' (KLM) is used.

The Kerr lens modelocking technique exploits a phenomenon known as 'The optical Kerr effect' where the non-linear refractive index change of a medium depends on the intensity of the light passing through that medium. This means, that the pulsed radiation in the cavity will experience a different refractive index to the continuous wave light in the cavity. The cavity is then arranged to only support the amplification of pulsed radiation. This is achieved either by the use of a hard aperture to spatially filter out the CW light (hard aperture mode-locking), or by aligning the cavity such that the CW and pulsed beams are not co-linear and then fixing the pump radiation to only be aligned with the pulsed beam (soft aperture modelocking - this is the modelocking technique used in the DCU oscillator). These two processes are outlined in Figure 2.5.

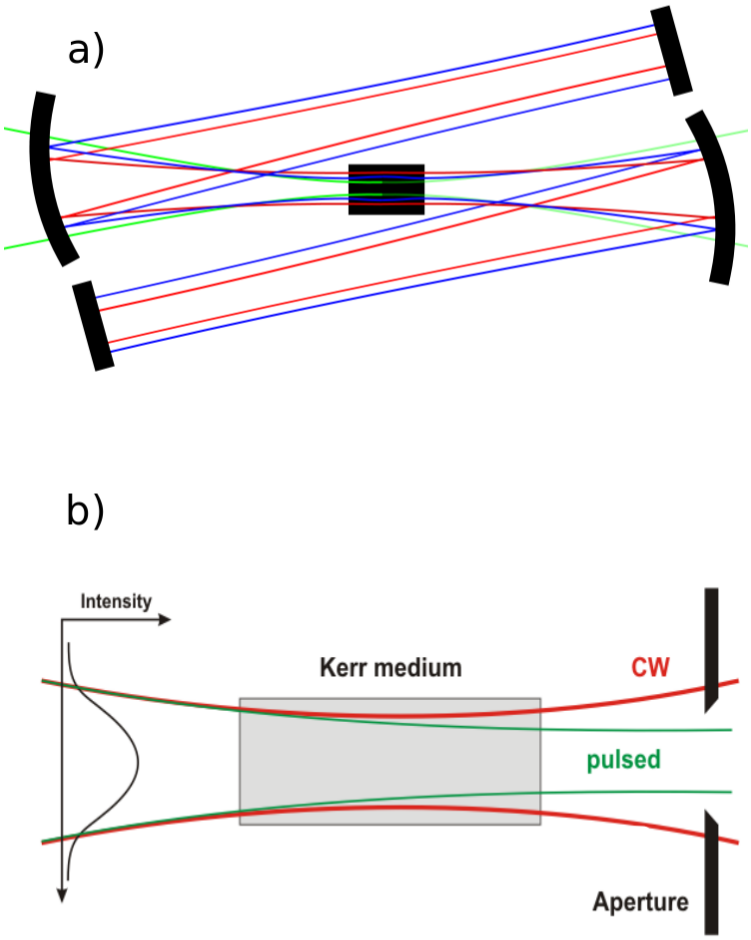

Figure 2.5: a) Soft aperture modelocking where red is the CW beam, blue is the pulsed beam and green is the pump beam. b) Hard aperture modelocking. Images taken from [9]

The laser pulses will undergo dispersion when they pass through the crystal and output coupler and this will broaden their temporal profile. To compensate for this and to ensure that the pulse at the exit port of the laser is a bandwidth limited pulse, a pair of prisms (PR1 and PR2) are used to compensate for the dispersion.

2.2.2 The stretcher

The next phase of the DCU ultrafast laser system is the amplifier which consists of three parts; The stretcher, amplifier and compressor. While the intensity dependent refractive index change is useful when trying to lock the modes of an oscillator laser cavity, the effect becomes troublesome when trying to amplify the laser pulses to a high average energy ($\approx$ 3 mJ). The problem is, that as the beam is amplified more and more, the optical Kerr effect gives rise to another non linear optical effect known as "self focussing" [10]. This self focussing results in very high energy densities generated inside the lasing medium which eventually exceed the damage threshold of the medium causing it to fracture. Traditionally, this problem was circumvented by spatially expanding the output of an oscillator to lower the energy density by increasing the beam area. However, this was a cumbersome method and required the manufacture of high quality large optics which were optically smooth over a large area. The result was very large, very expensive lasers. The invention of Chirped Pulse Amplification (CPA) provided a solution to this problem. The technique was invented in 1982 [5] and uses a pair of diffraction gratings to spectrally chirp the pulse, effectively broadening it in time and hence lowering the power density such that it could be safely amplified.

A schematic of the stretcher is shown in Figure 2.6. The input beam, which is the beam from the oscillator, is incident on a diffraction grating. The beam strikes the diffraction grating at the Littrow angle which means the incident and diffracted beams are at the same angle [12]. The purpose of the diffraction grating is to separate spatially the different frequency components of the laser pulse. Each frequency component is then directed along a different optical path such that when the beam is spatially recombined, the different frequency components will have travelled different distances. This introduces a linear frequency chirp across the temporal structure of the laser pulse. The effect of this is that the pulse has now been broadened in time such that it is safe to amplify without fear of damaging the lasing medium. The other optical components in Figure 2.6 are retroreflectors (SM9 and SM8), spherical mirror (SM6), folding mirror (SM7) or pickoff mirror (SM10). These components are

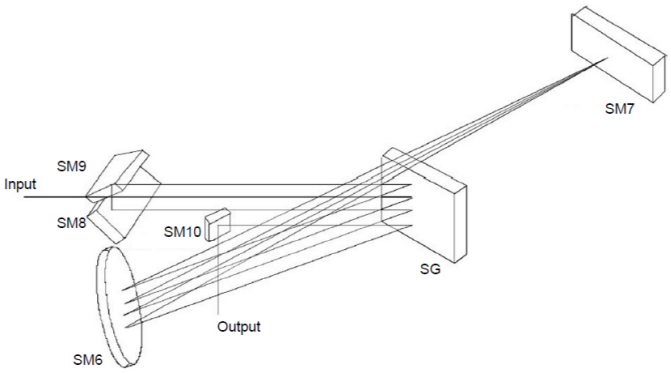

Figure 2.6: Schematic of the pulse stretcher in the DCU laser system. Image taken from [11]

used to make of the stretcher more compact and to allow the stretching technique to be accomplished with a single grating [13].

In an attempt to calculate the effect of the stretcher, it is perhaps useful to look at the behaviour of the laser pulse in the frequency domain. The electric field of the laser pulse can be written as;

$$E(\omega - \omega_o) = A(\omega - \omega_o)e^{i\phi(\omega-\omega_o)} \tag{2.14}$$

where $A(\omega - \omega_o)$ is the spectral amplitude and $\phi(\omega - \omega_o)$ is the spectral phase. ω_o is the centre frequency of the laser. Assuming that the phase varies slowly with frequency, a Taylor expansion can be used;

$$\phi(\omega) = \phi(\omega_o) + \phi'(\omega_o)(\omega - \omega_o) + \frac{1}{2}\phi''(\omega_o)(\omega - \omega_o)^2 + \frac{1}{6}\phi'''(\omega_o)(\omega - \omega_o)^3 \tag{2.15}$$

where $\phi(\omega_o)$ is the carrier phase which relates the electric field to the pulse envelope. The higher order terms are representative of the dispersion of the pulse. $\phi'(\omega_o)$

represents the group delay, $\phi''(\omega_o)$ represents the group delay dispersion and $\phi'''(\omega_o)$ is the third order dispersion [14]. The group delay dispersion is the most critical when discussing the stretcher. The group delay dispersion (GDD) introduces a linear chirp between the frequency components of the laser pulse. A pulse with a linear chirp has a non -zero GDD and it is the job of the stretcher to introduce a linear chirp while keeping the third order dispersion to a minimum. This is because, in order to achieve a high intensity short laser pulse, the broadening by the stretcher must be done in a reversible manner. Introducing cubic or other high order dispersions will make re-compression of the pulse difficult. The amount of GDD in a stretcher can be calculated from the following equation.

$$\phi'' = \frac{\lambda^3}{\pi c^2 \cos^2(\Theta_d)}(2f - L_1 - L_2) \tag{2.16}$$

where L_1 (measured to be 1.2 m) is the distance from the spherical mirror to the grating and L_2 (0.9 m) is the distance from the spherical mirror to the folding mirror. Θ_d (39^o) is the Littrow angle for the diffraction grating, λ is the centre wavelength (800 nm) and f is the focal length of the spherical mirror (1.2m); c is the speed of light. An input pulse of duration t_o with a Gaussian pulse shape will be stretched by an amount;

$$t \simeq \frac{(t_o^4 + (4\ln(2)\phi'')^2)^{1/2}}{t_o} \tag{2.17}$$

Assuming a transform limited 30 fs pulse will result in an output from the stretcher of $\approx$ 200 ps which is stretching factor of 6667.

2.2.3 The Legend Elite amplifier

Once the pulse is stretched, it is then safe to amplify it. There are two main types of amplifier design for ultrafast lasers. The first is a multipass amplifier which uses a series of mirrors to pass the beam through the crystal multiple times to incrase

the intensity. The second design, which is the design of the DCU system, is the regenerative amplifier [13]. In this configuration, electro-optic devices such as Pockels cells are used to trap the beam inside a laser cavity for a specified number of round trips and once the required amplification has occured, the pulse is then dumped from the cavity.

A Pockels cell is an electro optic device which has a voltage dependent birefringence [15]. By applying a particular voltage to the Pockels cell, it is possible to introduce a phase difference between the two perpendicular linear polarisation states of a laser beam. At a particular voltage (called the half-wave voltage) the phase difference introduced between the two states will be π radians and the Pockels cell will act as a half wave plate. A schematic of a Pockels cell is shown in Figure 2.7.

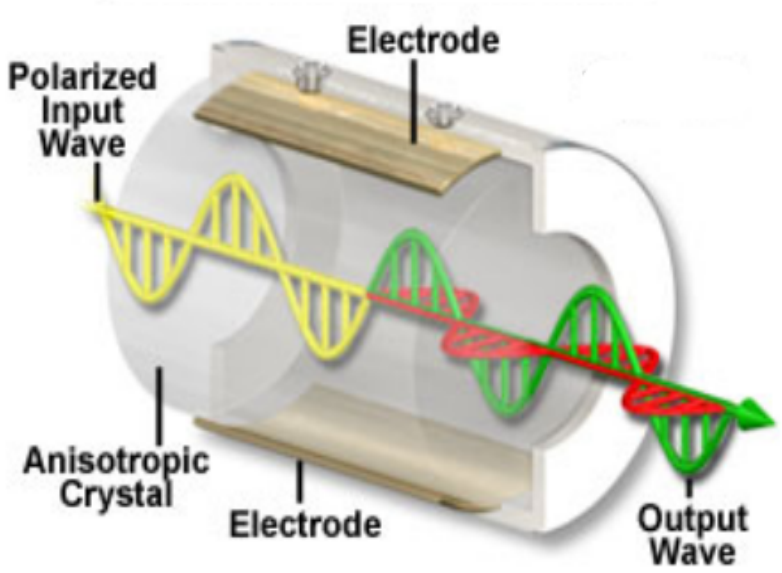

Figure 2.7: Schematic of a Pockels cell. Image taken from [16]. A polarised wave (yellow) will pass through the Pockels cell unaffected if there is no voltage applied (This is the green wave). However, if the appropriate voltage is applied, the Pockels cell will act as a half wave plate and rotate the polarisation by 90^o (This is the red wave)

Regenerative amplifiers generally use either a one or two Pockels cell design. In

either case, the cavity is designed such that the beam will be trapped inside for a given polarisation state. An outline schematic of the regenerative amplifier used at DCU is shown in Figure 2.8.

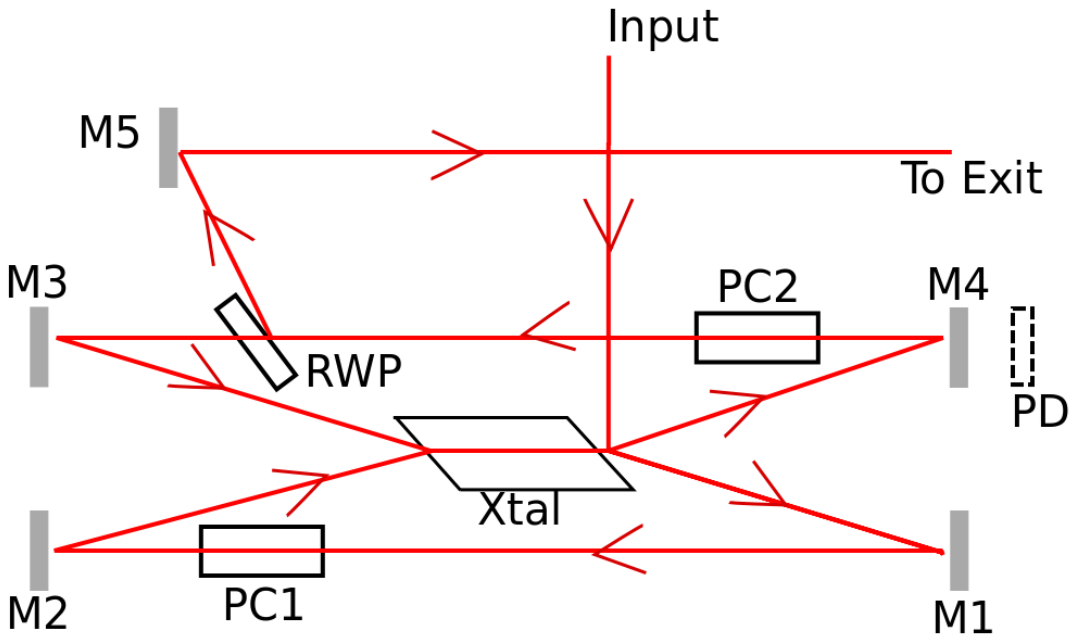

Figure 2.8: Schematic (not to scale) of the regenerative amplifier. Pump laser not shown.

The Ti:Sapphire crystal in the amplifier is pumped by a Coherent Evolution Nd:YLF laser. This laser has an output power of 19 W at a repetition rate of 1 kHz at 527 nm. The output pulses from the Evolution are $\approx$ 100 ns in duration. Because the amplifier is designed to produce 3 mJ of pulse energy, this creates an excessive heat load on the crystal requiring the crystal to be cooled externally to -10^{o} C using a thermo-electric cooling device. The input seed beam which comes from the stretcher is polarized linearly in a plane perpendicular to the optical bench. When it enters the regen it is Brewster reflected off the laser crystal and subsequently

off mirrors M1 to M2. If there is no voltage applied to PC1, the beam will simply re-trace its path and exit the cavity. By applying a quarter wave voltage pulse to PC1, the seed beam will rotate 90^o in polarisation and will no longer exit the regen upon its second reflection on M1. Instead, it will travel through the crystal to M3 and then M4 from where it will re-trace its path and bounce back and forth through the cavity (if no voltage is applied to PC2). RWP is a rotating wave plate which will either reflect or transmit the beam depending on its polarisation. As the voltage is PC2 is off, and the beam bounces around in the cavity between M1 and M4 it becomes amplified at each pass through the amplifier. The "amplification buildup" can be monitored on a photodiode placed behind M4. A quarter wave voltage pulse is then applied to PC2 at a time chosen to correspond to the maximum of the amplified build up in the cavity. This rotates the polarization by 90^o where RWP now acts as a reflector and the pulse is sent out of the cavity for recompression. A typical photodiode signal showing the amplification buildup is shown in Figure 2.9.

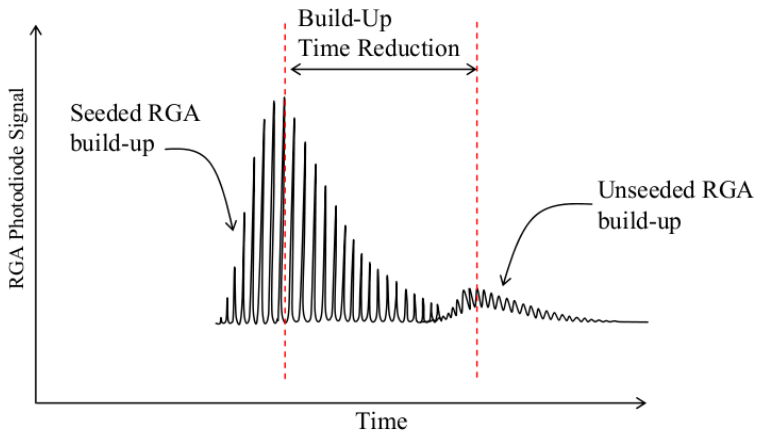

Figure 2.9: Typical photodiode build up trace showing amplification of both the seeded and unseeded emission in the regenerative amplifier (RGA). The "build up reduction time" is necessary to ensure that when the emission from the seeded buildup exits the cavity, no unseeded buildup is present. Image taken from [11]. A typical value for "buildup reduction time" is 45 ns. This pattern is seen when no voltage is applied to PC2.

2.2.4 The compressor

The compressor is a single grating device which has a very similar optical layout to the stretcher. It is comprised of retro-reflecting mirrors and diffractive optics. However, the function of the compressor is to reverse the linear chirp introduced by the stretcher and also to compensate for any dispersion effects caused by the regen. The concept of a grating compressor was first introduced a long time before the invention of CPA as a device used to compensate for dispersion through transmissive optics [17]. The input beam to the compressor can be carefully aligned remove any high order dispersion contributions also. It is important that both the stretcher and compressor gratings are aligned parallel such that the linear chirp can be completely removed without the introduction of higher order dispersions. Both the stretcher and compressor gratings are mounted on precision controlled motors such that their position and angle can be changed from outside the cavity in order to optimise the pulse width and spectrum. In order to optimise the compressor, two methods were used. The first is a technique known as "white light generation" where the beam is tightly focussed in free space creating a super-continuum which manifests itself as a bright white light. By changing the position of the compressor, the white light signal is maximised indicating the shortest pulse width has been acheived. The second technique to optimise the compressor was to study the ionization signal in a time of flight mass spectrometer of a noble gas (namely argon). The position of the compressor was then adjusted and then optimised by observing the yield of Ar^{3+}.

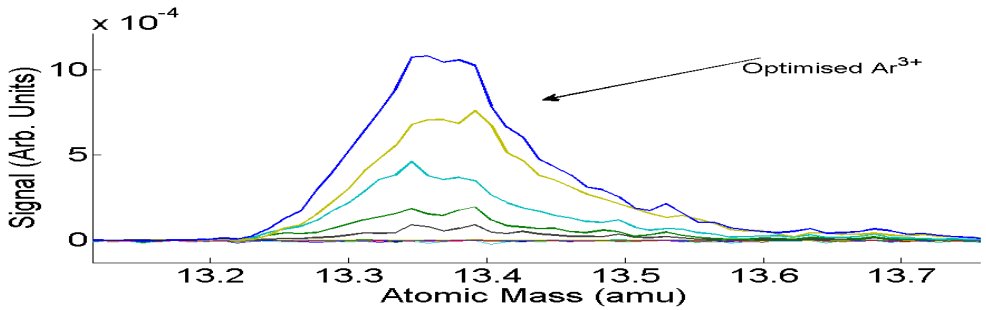

Figure 2.10: Plot of triply ionized argon (Ar^{3+}) as the compressor is optimised.

2.2.5 Second harmonic generation

Some of the work presented in this thesis was performed using the second harmonic of the output of the amplifier. Frequency doubling is achieved by using a BBO crystal which has a non-linear polarisation response to an input electric field [15]. This response can be written in the form;

$$P = \epsilon_o(\chi_1 E(t) + \chi_2 E^2(t) + \chi_3 E^3(t) + ...) \tag{2.18}$$

where χ_2 is the second order susceptibility and χ_3 is the third order susceptibility and so on. Ignoring any terms other than the second term gives;

$$P_2 = \epsilon_o \chi_2 E^2(t) \tag{2.19}$$

Consider an input wave consisting of two equal amplitude waves with frequencies ω_1 and ω_2 respectively.

$$E(t) = Ae^{-i\omega_1 t} + Ae^{-i\omega_2 t} \tag{2.20}$$

Substituting Equation 2.20 into Equation 2.19 and setting $\omega_1 = \omega_2 = \omega$ gives:

$$\frac{P_2}{\epsilon_o} = 2\chi_2 |A_1|^2 + 4\chi_2 A_1^2 e^{-i2\omega t} \tag{2.21}$$

From Equation 2.21 it is seen that combining two waves of equal amplitude and frequency in a non-linear optical medium with a non zero χ_2 value will produce a two termed signal in the second order. The first term contains no electromagnetic wave generation and is manifested as a static transient electric field across the crystal. The second term is an electromagnetic wave whose frequency is twice the input frequency. The SHG signal can then be considered as a process which involves three waves (two

input waves of frequency ω and one output wave of frequency 2ω. In order for successful SHG generation, the phase velocity of the input and output waves must be matched such that the sum of the wave vectors of all three waves is zero.

The BBO crystal used for SHG at DCU was a Type I BBO crystal. Typically, these crystals are cleaved along a particular crystallographic plane to satisfy the phase matching conditions. The two input waves will have the same polarization (ordinary with respect to the optic axis) and will produce a wave with extraordinary polarization. In the DCU SHG system, the input power was typically 1 W which produced 600 mW of power at the second harmonic. This gives a conversion factor of ca. 60 %.

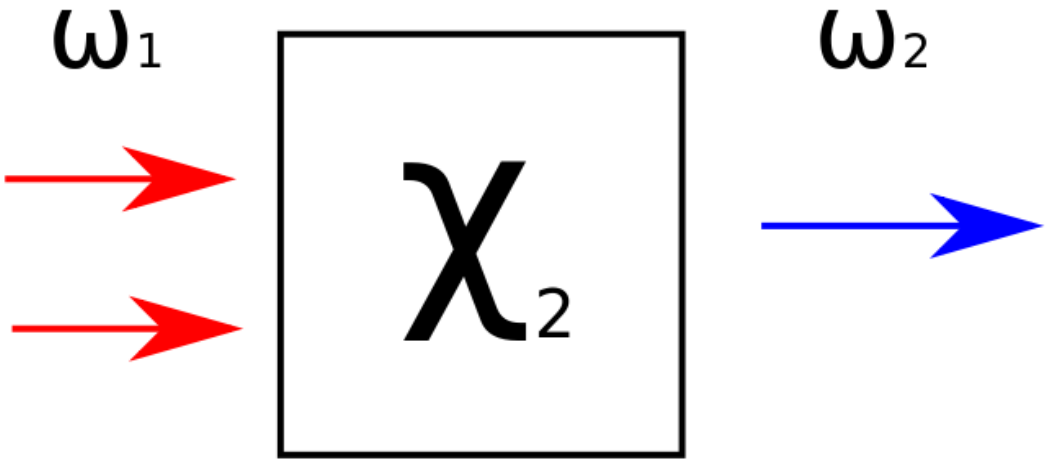

Figure 2.11: Schematic of SHG process.

The intensity of the SHG signal will be maximised when the sum of the wave vectors is equal to zero [10]. That is, $\Delta k = 0$. If Δk is not zero, the polarisation wave $P(2\omega)$ will oscillate in and out of phase with the emitted second harmonic electric field $E(2\omega)$. In this situation, the signal will oscillate as $\sin(\Delta k l/2)$ where l is the length of the crystal. Because the coherence length of the second harmonic signal is equal to $l_c = \pi/\Delta k$, it is not useful to have a BBO crystal that is much longer than the coherence length [15].

2.3 Pulse characterisation methods

2.3.1 Spectral diagnostics

It was necessary to measure the spectral output at different points within the laser to ensure stable and optimised operation. A fibre optic coupled Stellarnet grating dispersing spectrometer was used to make spectral measurements of the beam, The Stellarnet spectrometer had a resolution of $\approx$ 1 nm and a spectral range of 200 nm - 1000 nm. Below are typical optimised spectral outputs of each part of the laser system; The oscillator output, the stretcher output and the compressor output. All spectra were recorded with an integration time of 15 ms meaning that each spectrum is an average of 15 pulses for the amplifier and $\approx$ 1.2 million pulses for the oscillator.

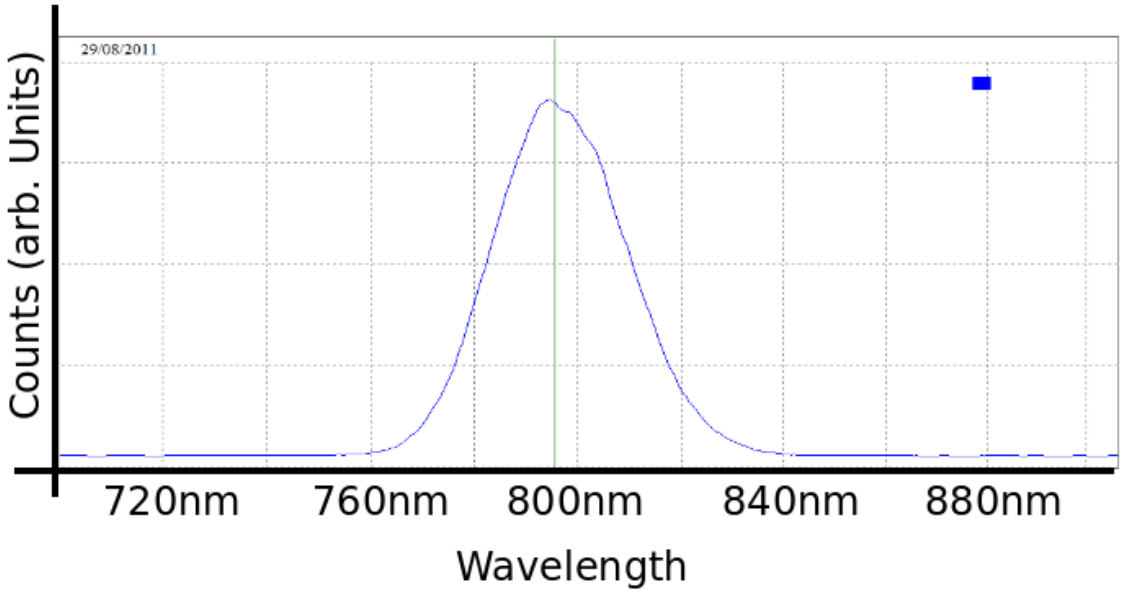

Figure 2.12: Output spectrum of the Legend Elite amplifier. The bandwidth at FWHM is 12 nm.

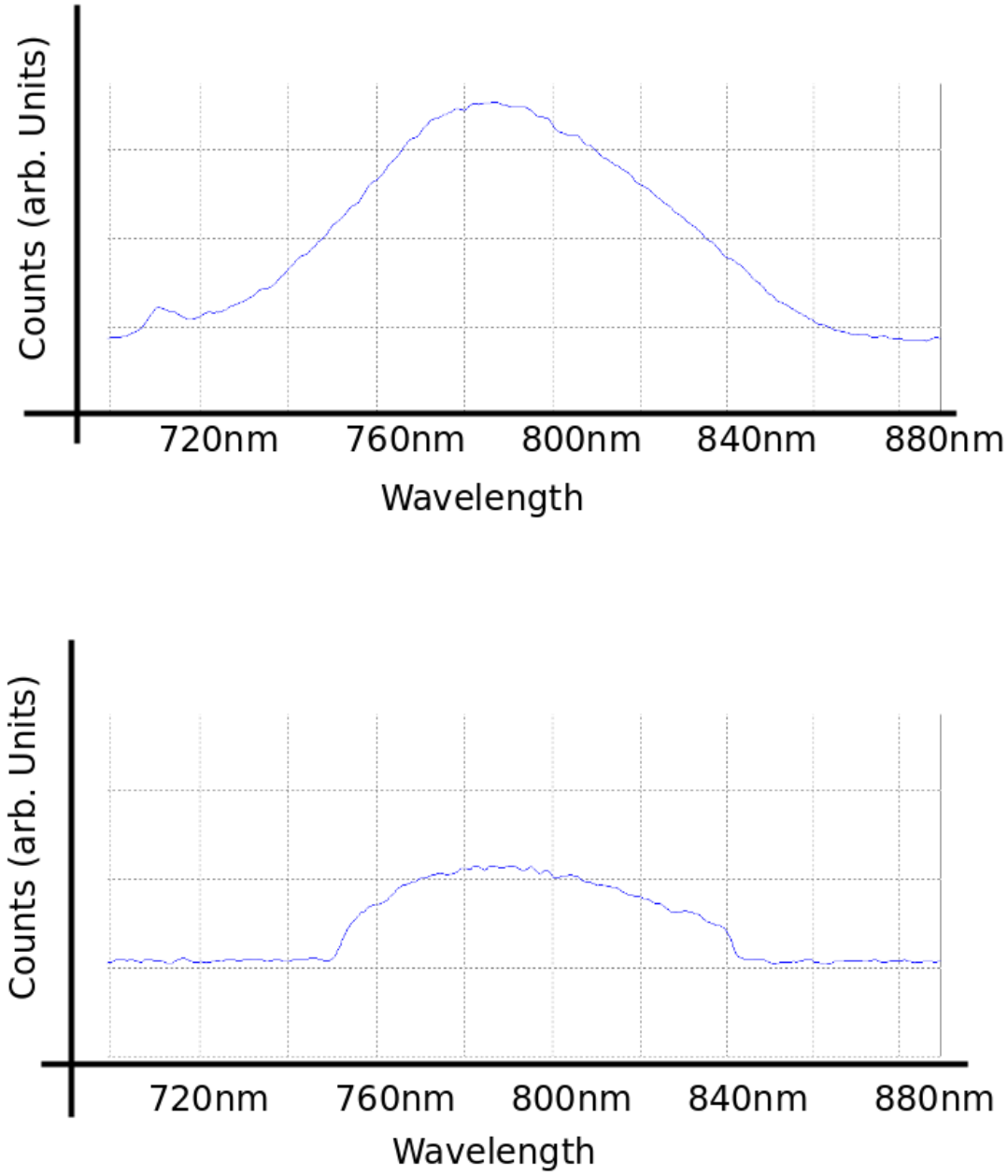

Figure 2.13: Output spectrum of the oscillator (top panel) and the stretcher (bottom panel). It was necessary to measure the stretcher spectrum to ensure that the portion of the stretched beam that entered the regenerative amplifier had sufficient bandwidth to ensure adequate re-compression.

2.3.2 Intensity autocorrelation

To measure the temporal width of the pulse, a technique called second order autocorrelation was used (Figure 2.14). The device used to measure the pulse width was a commercial APE Pulsecheck autocorrelator (sample trace shown in Figure 2.15). An autocorrelator works by splitting the laser beam into two parts using and, using an interferometer, delaying one beam with respect to the other [18]. The two beams are then focussed into a non-linear crystal (such as a BBO crystal described above) and the SHG signal is measured as a function of optical delay. The electric field of the SHG signal will produce an intensity profile which is related to the intensity profile of the original laser pulse by the equation:

$$I_{SHG}(\tau) = \int I(t)I(t-\tau)dt \tag{2.22}$$

Thus, the FWHM of the SHG signal as a function of delay can be related to the temporal width of the original pulses. For a Gaussian beam, the FWHM of the SHG signal will be a factor of $\sqrt{2}$ greater than the original pulse width [18].

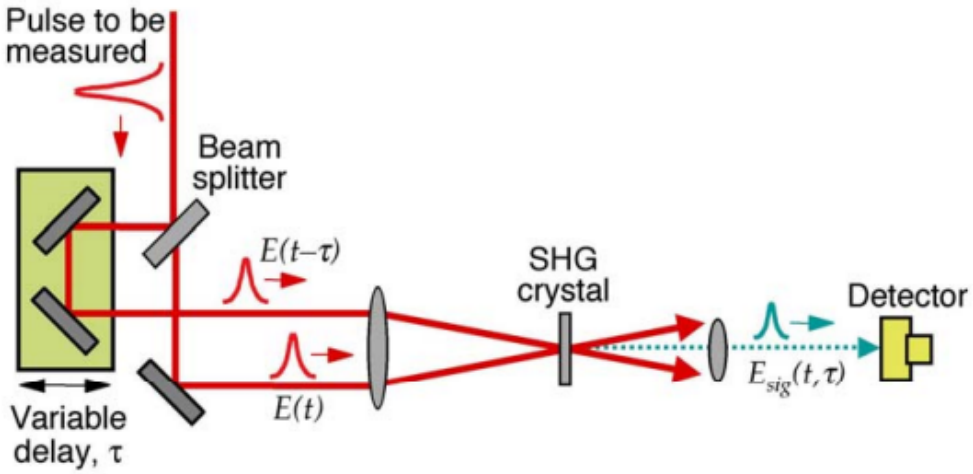

Figure 2.14: Schematic of the intensity autocorrelation setup. Image taken from [18]

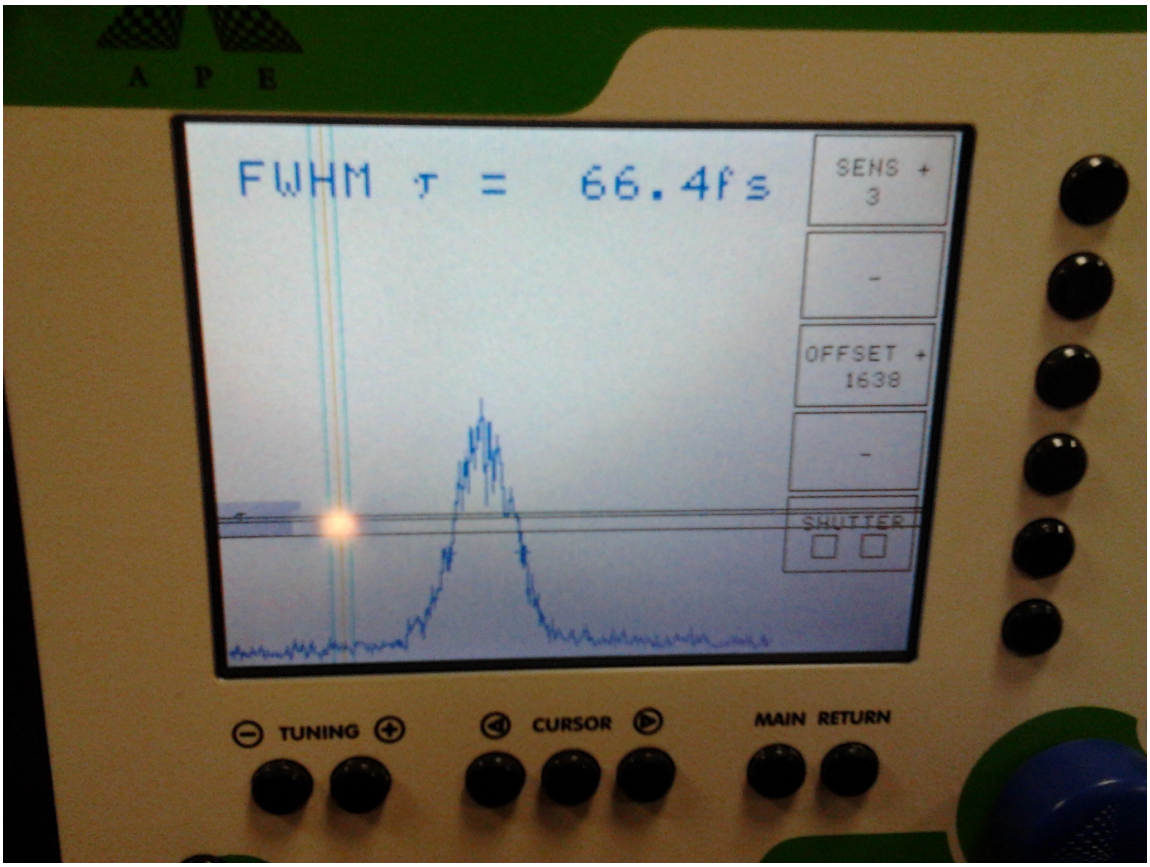

Figure 2.15: Sample photograph taken from APE Pulsecheck autocorrelator

2.3.3 Development of a compact interferometric autocorrelator

Mathematically, the cross correlation of two square integrable functions is given by:

$$f(t) \star g(t) = \int_{-\infty}^{\infty} f^*(t)g(t+\tau)dt \tag{2.23}$$

If the functions are equal ($f(t) = g(t)$) and real ($f^*(t) = f(t)$), the cross-correlation is simply the autocorrelation of $f(t)$.

$$A(t) = \int_{-\infty}^{\infty} f(t-\tau)f(t)dt \tag{2.24}$$

The function $A(x)$ simply describes how similar a function is to a time delayed copy of itself. In the case where a pulse is mixed with a time delayed replica of itself in a non-linear medium (such as a SHG crystal), a second harmonic signal is generated that is proportional to the polarisation of the crystal. That is, the radiated field will depend on the square of the input field. Thus, the second harmonic signal is proportional to $(E(t) + E(t-\tau))$. This expression can be expanded into the form:

$$E_{SHG}(t) = E(t)^2 + E(t-\tau)^2 + 2[E(t)E(t-\tau)] \tag{2.25}$$

However, whereas the terms $E(t)^2$ and $E(t-\tau)^2$ correspond to fields which radiate in the direction of their respective input field, the $E(t)E(t-\tau)$ term will radiate in the direction of the resultant of these two fields. If, as in the case in Figure 2.14, the two beams are made to combine in a non-collinear fashion in the crystal and if a detector is placed on the optic axis, only the cross term is retained in the measured signal and the intensity autocorrelation relation in Equation 2.22 is retrieved.

Consider now the case where, unlike above, the laser pulse is collinear with its replica. In this case, the SHG output will be generated by the superposition of two

electric fields. The electric field of the laser pulse that generates the second harmonic is written as:

$$E(t) = E(t) + E(t-\tau) = A(t)e^{j\omega t}e^{j\phi} + A(t-\tau)e^{j\omega(t+\tau)}e^{j\phi} \tag{2.26}$$

The detector then measures the intensity auto-correlation corresponding to this superposed electric field. Carrying through the calculation shows that the intensity of the second harmonic signal in a collinear case becomes:

$$\begin{aligned} I(\tau) \;=\; & \int_{-\infty}^{\infty} [|A(t-\tau)|^4 + 4|A(t-\tau)|^2|A(\tau)|^2 + |A(t)|^4 \\ & +2A(t-\tau)|A(t)|^2A^*(t)e^{-j\omega\tau} + c.c \\ & +2A(t)|A(t-\tau)|^2A^*(t-\tau)e^{j\omega\tau} + c.c \\ & +A^2(t-\tau)(A^*(t))^2e^{-j2\omega\tau}]dt \end{aligned} \tag{2.27}$$

It is seen then that the intensity autocorrelation in the collinear case will consist of four terms. The first is a background DC intensity given as

$$I_{back} = \int_{-\infty}^{\infty} |A(t-\tau)|^4 + |A(t)|^4 dt = \int_{-\infty}^{\infty} I^2(t)dt \tag{2.28}$$

The second term is the intensity autocorrelation:

$$I_{int} = \int_{-\infty}^{\infty} |A(t-\tau)|^2|A(\tau)|^2 dt = \int_{-\infty}^{\infty} I(t)I(t-\tau)dt \tag{2.29}$$

The third term is an oscillating term at the fundamental frequency ω.

$$I_{\omega}(\tau) = 4Re\int_{-\infty}^{\infty} (I(t) + I(t-\tau))A(t)A^*(t-\tau)e^{j\omega\tau}dt \tag{2.30}$$

Finally there is an oscillatory term at the second harmonic which is given as:

$$I_{2\omega}(\tau) = 2Re \int_{-\infty}^{\infty} (A^2(t-\tau)(A^*(t))^2 e^{-j2\omega\tau} dt \tag{2.31}$$

It is seen then in the case where there is no overlap between the pulses ($\tau = \pm\infty$) then the intensity autocorrelation term and the oscillating terms go to zero and the measured signal is equal to I_{back}. In the case where the pulses are exactly overlapped ($\tau = 0$) then all integrals are equal to the background integral and the total signal will be equal to $I(0) = 8I_{back}$. The non collinear (often called intensity autocorrelation) and the collinear (known as interferometric autocorrelation) cases are distinguished by a number of features. Firstly, an intensity autocorrelation signal will go to zero at large delays between the pulses whereas the interometric autocorrelation signal contains a nonzero background. Secondly, the interferometric autocorrelation signal contains oscillations due to the interference of the two input waves and is also characterised by a clear 8:1 signal to background ratio [19].

Detailed studies of both the intensity and interferometric autocorreleation methods [19] have shown that both methods produced fairly accurate estimates of the laser pulse duration once a pulse shape is assumed. However, interferometric autocorrelation has also been shown to allow for estimates of the pulse shape, the pulse phase and, if taken together with the pulse spectrum, measurements of spatial chirp, spectral chirp, group velocity dispersion and group velocity mismatch.

In principle, the only components necessary for an interferometric autocorrelation measurement are a component which will split a laser pulse into two replica pulses, a method to introduce a controlled delay into those pulses, a non-linear optical medium (to now, the only non linear interaction considered has been second harmonic generation, but in general any instantaneous non linear interaction will work) and a detector. With this in mind, an attempt was made to develop an interferometric autocorrelator. The device was designed and constructed with the aim of being easy to align and also cost effective. The next sections outline the design and construction of the device.

Optical Setup and principle of operation

The optical setup for the interferometric autocorrelator is shown in Figure 2.16.

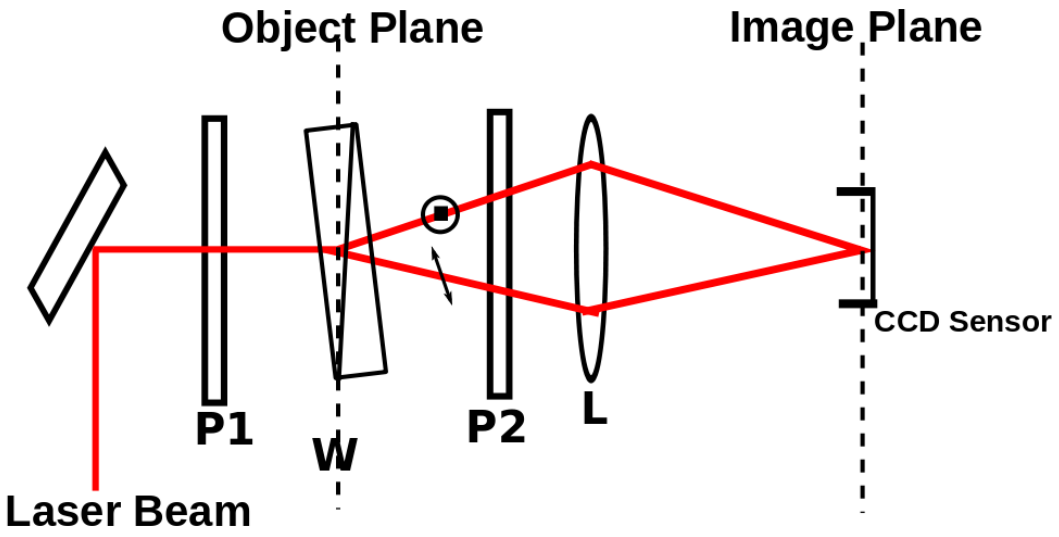

Figure 2.16: Optical setup for interferometric autocorrelator.

The interferometric autocorrelator is comprised of 5 optical components; A lens (L), two polarisers (P_1, P_2) a camera (CMOS Sensor) and a Wollaston prism (W). Traditionally, the pulse splitting and optical path delay are realised by the use of Michelson or Mach-Zehnder interferometers [13],[18]. However, in this set up, the interferometer is replaced by a Wollaston prism. A Wollaston prism is made of two wedges of Calcite joined at their hypotenuse faces. They are joined in a way such that their optic axis is perpendicular to both each other and the intended beam propagation direction. Calcite is highly birefringent in the optical wavelength region and hence, a beam propagating through the prism will experience one of two refractive indices depending on its relative orientation to the optic axis of the part of the crystal [20]. Thus, any linearly polarized beam incident upon the crystal will be resolved into orthogonally polarized components and each component will experience a different refractive index [12]. The speed of propagation will then be different for each component. At the interface between the two wedges, the optic axis will rotate

90^o and both beams experience a refraction. The deviation of the two beams leads to the principal use of a Wollaston prism as a polarising beam splitter. The divergence angle of the two beams is given by:

$$\alpha = 2(n_e - n_o)\tan\theta \tag{2.32}$$

where θ is the angle of the interface of the two wedges and n_o and n_e are the refractive indices experienced by electric field components perpendicular and parallel to the optic axis respectively (called the ordinary and extraordinary refractive indices). By considering the fact that the wedge thickness changes as a function of the perpendicular distance from the centre of the prism, the path difference between each component is written as:

$$\Delta = 2x(n_e - n_o)\tan\theta \tag{2.33}$$

Where x is the lateral displacement from the centre of the crystal. Refraction will occur both inside the prism (due to the flip of the optic axis) and at the exit face of the prism. Thus, the effective divergence point between the two beams will occur in a plane inside the prism [21]. The angle of this plane with respect to the faces of the prism is given as:

$$\Psi = (n_e + n_o)\theta/2n_e n_o \tag{2.34}$$

For the development of an interferometric autocorrelator, the Wollaston prism was rotated such that this plane was perpendicular to the beam direction. This plane was also imaged onto a CMOS sensor using a 100 mm focal length bi-convex lens positioned to give a magnification of 1. The function of P_1 is to align the polarisation of the input beam to 45^o to the optic axis of the prisms so that the ordinary and extraordinary components have the same amplitude. Because the beams that

diverge out of the Wollaston are orthogonally polarised, P_2 acts to align their polarisations such that interference will be observed. In this way, the device acts as an interferometer where the beam delay is created across the face of the laser beam itself. For this system, a Wollaston prism with a wedge angle of 7.3^o with dimensions $(L \times B \times H)$ of $(2 \times 20 \times 20)$ mm is used. From Equation 2.33 it is seen that a path difference of ± 1.4 ps across the full face of the prism is achievable.

The Wollaston prism belongs to a family of devices which create a delay across the face of the beam. Their use in autocorrelation systems has been documented before and is not novel [21]. Similarly, the optical setup shown in Figure 2.16 has been used before in autocorrelation. However, in [21], the system required the Wollaston prism to be manually scanned across the focus of the laser beam. In this optical setup, the beam remains unfocussed and there are no moving parts. This not only allows for single shot detection but also makes use of the 'Fellgett advantage' [12] to increase the signal to noise ratio.

The 'Fellgett advantage' results in a gain in the signal to noise ratio in this device over traditional Michelson based autocorrelators. Because traditional Michelson autocorrelators use a moveable mirror to capture the autocorrelation signal, there is an associated dwell time with each delay point. This dwell time governs the signal to noise ratio. In this device, all delay points are measured at once meaning that for the same signal for noise ratio, the total acquisition time is reduced or that, for a particular acquisition time, the dwell time is reduced.

The detector

In our system, a 352×288 pixel webcam with 8-bit resolution was used. Since most webcams come equipped with an IR filter to block radiation above 700 nm, this webcam is used as the non linear medium as well. The transmission curve for the IR filter is shown in Figure 2.17 and from this it is seen that the detector is blind to 800 nm radiation. However, if the laser pulses are of sufficient intensity, a non-linear process can occur in this filter to enable interferometric autocorrelation to be

realised.

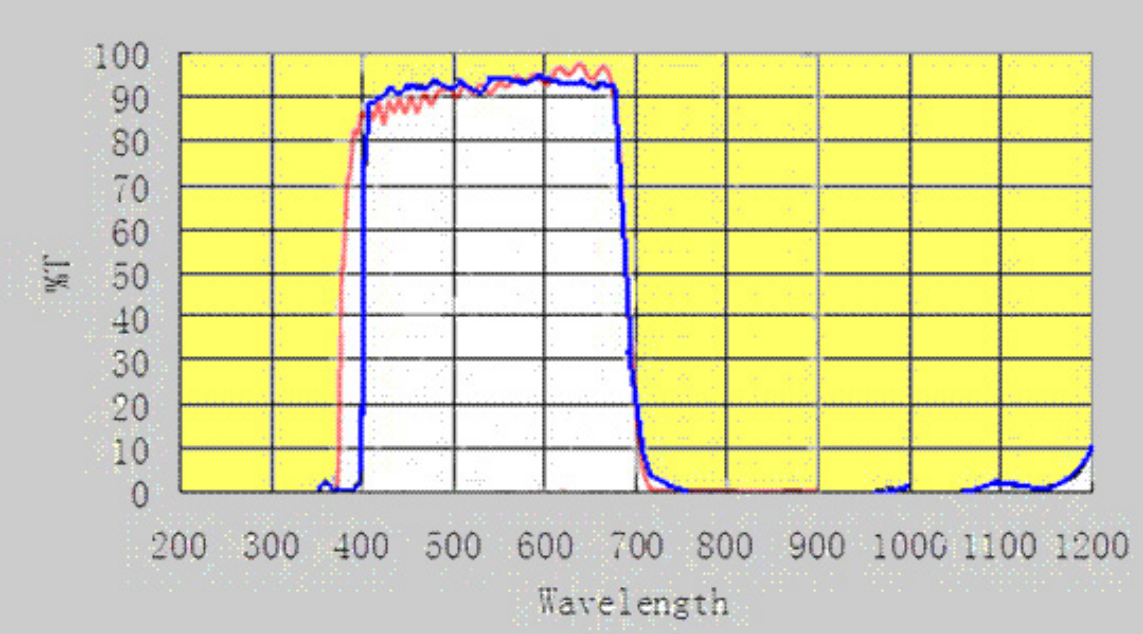

Figure 2.17: Transmission of the IR filter on the webcam. Image taken from [22]

Figure 2.18 shows that the response of the camera to modelocked radiation is orders of magnitude higher than to CW radiation. There is a negligible signal registered for CW emission of the oscillator which is most likely due to very inefficient response to light of wavelength 800 nm by the camera. A quadratic fit to both datasets of the form $f(x) = Ax^2 + Bx + C$ reveals that the non-linear component in the modelocked case is two orders of magnitude higher than in the CW case. The ratio of the non linear to linear components (A/B) is calculated to be ≈ 2 for the modelocked case and ≈ 0.2 for the CW case. Another interesting feature is the voltage at which saturation occurs for the modelocked case. 1.4 V corresponds to the difference in Fermi energies for the p-type and n-type channels in the silicon pixels of the webcamera. This has been noticed and reported before [23]. It was not possible to determine the exact nature of the non-linear interaction present in the detector that was used. However, of the two most likely candidates (two photon fluorescence within the filter or two photon absorption within the Silicon detector) it seems that

two photon fluorescence is the most probable. The band gap of the silicon in the webcam (1.1 eV) is below the photon energy of the laser (1.55 eV) meaning that for 800 nm radiation, a silicon detector cannot act as a purely non-linear medium even though the two photon cross section is relatively high [24], [25], [26]. This coupled with the negligible response to CW radiation leads to the conclusion that two photon fluorescence takes place in the IR filter and this flourescence is detected by the silicon CMOS chip.

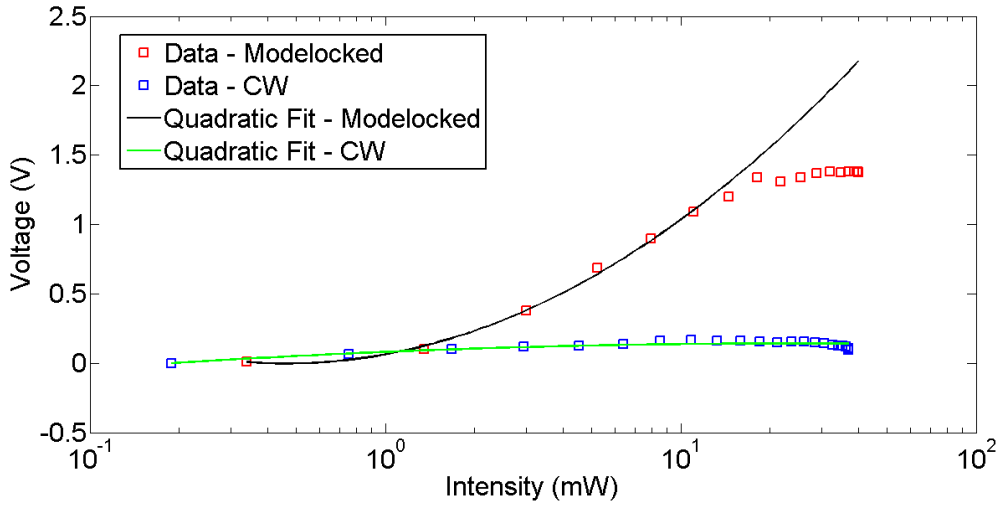

Figure 2.18: Spatially integrated response of the detector to both modelocked and CW radiation. Both datasets were fitted with a function of the form $f(x) = Ax^2 + Bx + C$

Figure 2.19 shows the signal detected on the webcamera showing interferometric autocorrelation signal. This image is averaged in the vertical direction. As seen in Figure 2.20 the periphery of the signal contains a slowly varying structure on top of which the interference pattern sits. A composite background signal is formed by adding together images taken with P_2 set to 0^o and 90^o and subtracting this from the raw interferometic image. The processed interferometric autocorrelation image is presented in Figure 2.21.

Figure 2.21 shows a signal to background ratio of 7:1 which is close to the theoretical value of 8:1. Signal to background ratios as low as 5:1 have been reported

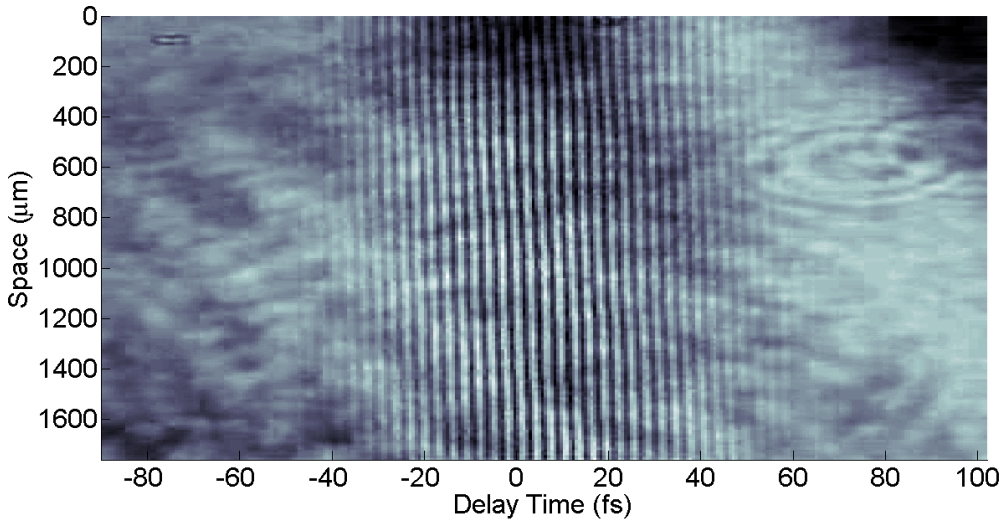

Figure 2.19: Raw image observed with the optical setup presented in Figure 2.16

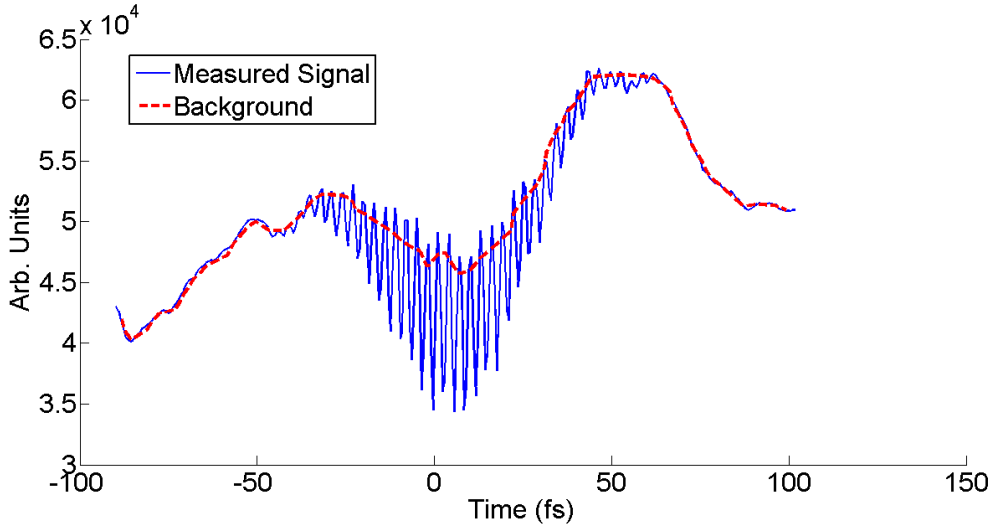

Figure 2.20: Averaged signal and background.

in the literature [20]. One possible explanation for the slightly less than ideal ratio would be if the polarisation of the input beam was not exactly 45^o leading to an amplitude mismatch between the two interfering beams inside the Wollaston prism.

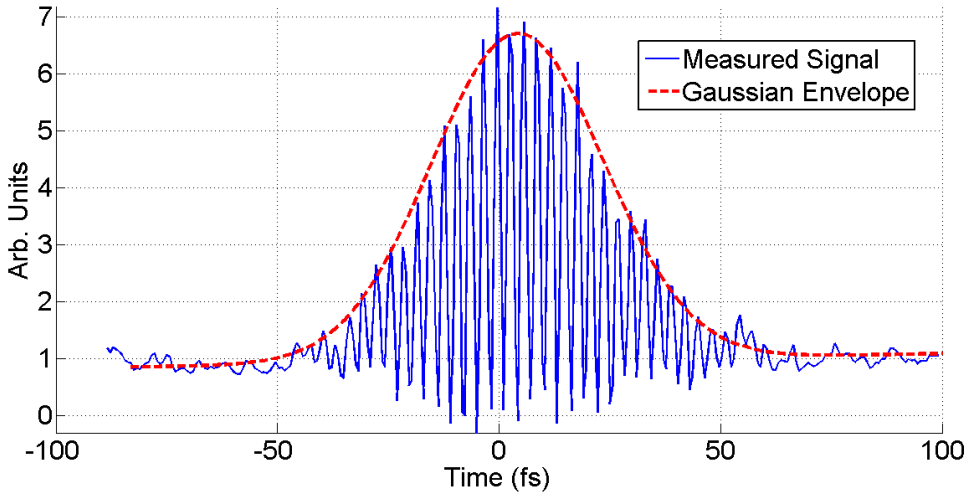

Figure 2.21: Processed interferometric autocorelation signal showing good agreement with the theoretical 8:1 signal to background ratio. A Gaussian fit to the overarching pulse envelope is shown in red.

In Figure 2.21, a Gaussian fit to the overarching envelope (shown in red) gives a full width half maximum of 63 fs. The goodness of fit between the Gaussian and experimental data points (adjusted r-squared = 0.9959) is an indication of a Fourier transform limited pulse. Multiplying the measured full width half maximum of the signal by the deconvolution factor for interferometric autocorrelation (1.53 for an assumed Gaussian pulse) leads to a pulse width measurement of 41 fs. The measurement in Figure 2.15 gives a pulse width value of 46 fs. These results are in general agreement however it is typical for interferometric autocorrelations traces to give larger autocorrelation widths than intensity autocorrelation for a transform limited pulse. An interferometric auto-correlation width which is lower than its corresponding intensity autocorrelation width is a possible indication of a linear phase chirp on the pulse [19]. To account for broadening through the optics in the Wollaston prism autocorrelator, a similar thickness of glass was placed in the beamline of the commercial intensity autocorrelator to achieve similar broadening. It is assumed that the commercial intensity auto-correlator provides no broadening to the pulse [18].

2.4 Summary and future work

In this chapter, the basics of lasing were described. Particular attention was paid to describing how ultrafast lasers operate using the techniques of modelocked oscillators, chirped pulse stretching, regenerative amplification and grating compression. Pulse characterisation methods are then described and the development of a non moving interferometric autocorrelator is discussed.

Bibliography

[1] W. Silfvast. *Laser Fundamentals.* Cambridge University Press, 1996.

[2] A. Einstein. On the quantum theory of radiation. *Physika Zeitschrift*, **18**:121, 1917.

[3] H.D. Young and R. Freeman and F. Lewis. *University Physics with Modern Physics*. Pearson, 12th edition, 2007.

[4] J.C. Diels and W. Rudolph. *Ultrashort Laser Pulse Phenomena*. Academic, 2nd edition, 2006.

[5] D. Strickland and G. Mourou. Compression of amplified chirped optical pulses. *Optics Communications*, **56**:219, 1985.

[6] D. Qiang and Z. JiangFeng and T. Hao and Y. ChenXia and W. ZhiYi. Carrier-envelope phase locking of 5 fs amplified ti : sapphire laser pulse at 1 khz repetition rate. *Chinese Science Bulletin*, **53**(5):671–675, 2008.

[7] http://www.accessscience.com.

[8] Coherent Inc. Coherent micra user manual.

[9] http://en.wikipedia.org/wiki/kerr-lens-modelocking.

[10] R.W. Boyd. *Nonlinear Optics*. Elsevier., 3rd edition, 2008.

[11] Coherent Inc. Coherent legend elite user manual.

[12] E. Hecht. *Optics*. Optics. Harlow :Addison Wesley, 3rd edition, 1998.

[13] I.N. Ross and A.J. Langley and P. Taday. A simple achromatic pulse stretcher. page, 201, 1999.

[14] S. Backus and C.G. Durfee and M.M. Murnane and H.C. Kapteyn. High power ultrafast lasers. *Review of Scientific Instruments*, **69**(3):1207–1223, 1998.

[15] Y.B. Band. *Light and Matter: Electromagnetism and Optics and Spectroscopy and Lasers.* John Wiley and Sons, 2006.

[16] http://www.olympusconfocal.com/java/pockelscell/.

[17] E.B. Treacy. Optical pulse compression with difraction gratings. *IEEE J. Quantum Electronics*, **5**:454, 1969.

[18] R. Trebino. Intensity autocorrelation. *www.swampoptics.com/PDFs/tutorials-autocorrelation.pdf*.

[19] F. Hache and T.J. Driscoll and M. Cavallari and G.M. Gale. Measurement of ultrashort pulse durations by interferometric autocorrelation: Influence of various parameters. *Applied Optics*, **35**(18):3230–3236, 1996.

[20] C. Chen and J.Y. Huang and C. Pan. Pulse retrieval from interferometric autocorrelation measurement by use of the population-split genetic algorithm. *Optics Express*, **14**(22):10930–10938, 2006.

[21] D.A. Reid and S.G. Murdoch and L.P. Barry. Stepped-heterodyne optical complex spectrum analyzer. *Optics Express*, **18**(19):19724–19731, 2010.

[22] http://www.speedflameout.talktalk.net/ir-filter.html.

[23] D.T. Reid and M. Padgett and C. McGowan and W.E. Sleat and W. Sibbett. Light-emitting diodes as measurement devices for femtosecond laser pulses. *Optics Letters*, **22**(4):233–235, 1997.

[24] D.H. Reitze and T.R. Zhang and W.M. Wood and M.C. Downer. 2-photon spectroscopy of silicon using femtosecond pulses at above-gap frequencies. *Journal of the Optical Society of America B-Optical Physics*, **7**(1):84–89, 1990.

[25] A.D. Bristow and N. Rotenberg and H.M. van Driel. Two-photon absorption and kerr coefficients of silicon for 850-2200 nm. *Applied Physics Letters*, **90**(19):191–104, 2007.

[26] D. Panasenko and Y. Fainman. Single-shot sonogram generation for femtosecond laser pulse diagnostics by use of two-photon absorption in a silicon ccd camera. *Optics Letters*, **27**(16):1475–1477, 2002.

[27] J.C. Dainty and M.A. Fiddy. The essential role of prior knowledge in phase retrieval. *Optica acta*, **31**(3):325–330, 1984.

[28] R. Trebino and D.J. Kane. Using phase retrieval to measure the intensity and phase of ultrashort pulses - frequency-resolved optical gating. *Journal of the Optical Society of America A-Optics Image Science and Vision*, **10**(5):1101–1111, 1993.

[29] A.E. Yagle. Divide-and-conquer 2-d phase retrieval using subband decomposition and filter banks. *IEEE Transactions on Signal Processing*, **46**(4):1152–1154, 1998.

[30] K.W. Delong and R. Trebino and D.J. Kane. Comparison of ultrashort-pulse frequency-resolved-optical-gating traces for 3 common beam geometries. *Journal of the Optical Society of America B-Optical Physics*, **11**(9):1595–1608, 1994.

[31] D.J. Kane and R. Trebino. Single-shot measurement of the intensity and phase of an arbitrary ultrashort pulse by using frequency-resolved optical gating. *Optics Letters*, **18**(10):823–825, 1993.

[32] T. C. Wong and J. Ratner and V. Chauhan and J. Cohen and P.M. Vaughan and L.X. and A. Consoli and R. Trebino. Simultaneously measuring two ultrashort laser pulses on a single-shot using double-blind frequency-resolved optical gating.

Journal of the Optical Society of America B-Optical Physics, **29**(6):1237–1244, 2012.

[33] J. Cohen and D. Lee and V. Chauhan and P. Vaughan and R. Trebino. Highly simplified device for measuring the intensity and phase of picosecond pulses. *Optics Express*, **18**(16):17484–17497, 2010.

[34] E.P. Power and A.M. March and F. Catoire and E. Sistrunk and K. Krushelnick and P. Agostini and L.F. DiMauro. Xfrog phase measurement of threshold harmonics in a keldysh-scaled system. *Nature Photonics*, **4**(6):352–356, 2010.

[35] C. Iaconis and I.A. Walmsley. Spectral phase interferometry for direct electric-field reconstruction of ultrashort optical pulses. *Optics Letters*, **23**(10):792–794, 1998.

[36] D. Bigourd and J. Luce and E. Mazataud and E. Hugonnot and C. Rouyer. Direct spectral phase measurement with spectral interferometry resolved in time extra dimensional. *Review of Scientific Instruments*, **81**(5):53–105, 2010.

[37] I. Amat-Roldan and I.G. Cormack and P. Loza-Alvarez and D. Artigas. Measurement of electric field by interferometric spectral trace observation. *Optics Letters*, **30**(9):1063–1065, 2005.

[38] S. Yang and C. Hsu and S. Lin and Y. Lin and C. Langrock and M. M. Fejer. Ultrasensitive direct-field retrieval of femtosecond pulses by modified interferometric field autocorrelation. *Optics Letters*, **34**(20):3065–3067, OCT 15.

[39] B. Tsermaa and B.K. Yang and K. Myung-Whun and J . S. Kim. Characterization of supercontinuum and ultraviolet pulses by using xfrog. *Journal of the Optical Society of Korea*, **13**(1):158–165, 2009.

[40] J.L.A. Chilla and O.E. Martinez. Direct determination of the amplitude and the phase of femtosecond light-pulses. *Optics Letters*, **16**(1):39–41, 1991.

[41] http://en.wikipedia.org/wiki/file:grenouille-long.jpg.

[42] P. Kockaert and M. Haelterman and P. Emplit and C. Froehly. Complete characterization of (ultra)short optical pulses using fast linear detectors. *IEEE Journal of Selected Topics in Quantum Electronics*, **10**(1):206–212, 2004.

[43] P. Tomassini and A. Giulietti and L.A. Gizzi and M. Galimberti and D. Giulietti and M. Borghesi and O. Willi. Analyzing laser plasma interferograms with a continuous wavelet transform ridge extraction technique: the method. *Applied Optics*, **40**(35):6561–6568, 2001.

Chapter 3

Ultrafast laser ablation of solids

This section begins with a historical perspective on the research field of ultrafast laser ablation. Basic theoretical models of ultrafast laser ablation are then presented. The operating principles of a Langmuir probe and its use as a plasma diagnostic are presented. The design of a vacuum chamber to perform ultrafast laser ablation experiments is then presented. Time-of-flight measurements on the ions and electrons emitted from a silicon laser produced plasma are investigated. It is found that the plume contains three main regions: a fast oscillating region, a thermal component and a suprathermal component. It is shown through Langmuir probe analysis that there is strong indication of double layer formation within the plume and that the expansion of the plume is dependent on the ablation wavelength. Polarisation studies show that there is an indication of resonantly excited electrostatic fields within the plume which cause a reduction in thermal transport and electron conductivity.

3.1 Introduction

The ablation of solid material with pulsed laser radiation is a field of investigation that is as old as the laser itself [1]. The invention of chirped pulse amplification [2] in the mid 80's opened up a whole new subfield of laser ablation research. The pulses that these lasers produce are of such short temporal duration that material can be ablated much faster than the electron/phonon coupling time in most solids. The resulting plasma formation has been found to be very different from its long pulse counterpart. These Ultrafast laser ablation (ULA) plasmas have been studied from both a fundamental and applications based perspective [3],[4].

From a fundamental perspective, it has been shown that the plasma plume formation in the short pulse regime is well described by treating the electrons and ions as having separate temperatures [5]. The dynamics of the plasma expansion was studied in some detail by the group of Amoruso [6]. One important conclusion of their studies was that the plasma plume consisted of both thermal and non thermal components and that the ion emission was influenced by the polarisation state of the laser [7]. It was also shown that the expansion of the plume is described quite well by the hydrodynamic models of Anisimov et al [8]. Similarly, studies of the ULA plume have shown that the average charge state of the resulting plumes is quite low, that the ion emission depends on the pre-pulse main-pulse contrast ratio and that the ion emission varies with pulse width. Comparisons of ion emission in ULA have been made with corresponding long pulse plasmas in terms of plume expansion and fluence dependance [9].

From an applications perspective, ULA has shown to be useful in terms of micro/nano machining [10], nano particle production [11] and pulsed laser deposition [12, 13]. It has been shown that a ULA plume contains a significant nanoparticle population. The angular distribution of these species has been studied as has their size distributions for different metals [13]. ULA has also been used for studying structural changes in different metals during ablation and it has been found that ULA offers a significant improvement in controlling the depth of ablation due to the

lower amount of melted material produced in the ablation [14]. Other key application areas of ULA include colloidal suspension generation [15], etching [16] and plasmon generation [17]. The effects of surface contamination on ULA have also been investigated [18].

The first theoretical models of ULA were descibed by Anisimov et al [8]. This model described the expansion of a plasma plume produced by ULA and considered the competition between the non-thermal (photoelectric, electrostatic) and thermal (thermionic) emissions. It showed that at high intensities, the emission is dominated by a thermal component. This model also hypothesised that the thermal emission from a ULA plasma could be used to determine electron/phonon relaxation kinetics. This was later further expanded on and experimentally confirmed [5]. The two temperature model has received significant attention in the literature and various solutions and extensions of the initial model have been subsequently reported [19]. Investigations into the formation and investigation of the plasma have been performed using molecular dynamics [20] and hydrodynamic simulations [13]. To date, the most complete and detailed of these efforts is the freely available "Multi-fs" code [21]. Analytical models to describe the formation of the plasma have been developed most prolifically by Gamaly et al [22].

The purposes of using a Langmuir probe over other diagnostic techniques is two fold. Firstly, while spectroscopic and other optical diagnostics have the benefit of being non-invasive, they suffer from experimental complications. Namely, the high repetition rate of the laser makes synchronisation and acquisition difficult. Other electrostatic detection means such as Faraday cups suffer from a loss of spatial localisation. Secondly, there is an abundance of spectroscopic data and Faraday cup data present in the literature. Very few studies could be found where a langmuir probe is used to characterise the plasma. This ensures the novelty of the results.

3.1.1 Using a Langmuir probe to study laser plasmas: A historical perspective

As will be discussed later, using Langmuir probes to diagnose laser plasmas is not the favoured method due to the dynamic nature of the plasma. In fact, restrictions set by well established validity conditions must be adhered to in order to ensure that the Langmuir probe is a suitable diagnostic techique. Because of this, much of the literature concerned with Langmuir probes in laser ablation studies is confined to their use as a time of flight detector as opposed to their traditional use as an electrostatic ion/electron probe [7]. Nonetheless, experiments have been reported where Langmuir probes have been used as diagnostic tools in their traditional sense. Namely, the groups of Torrisi and Lunney have used Langmuir probes to diagnose the density and temperature of laser plasmas albeit in the long pulse regime [23, 24]. Some studies have reported the use of Langmuir probes as diagnostic tools for ULA densities and temperatures where their validity in ULA has been established [25]. One interesting result of Langmuir probe analysis has been in the demonstration of double layer electron plumes in laser plasmas [26]. It has been shown through Langmuir analysis that laser plasmas at high fluence have been found to contain two separate electron species each with its own temperature. This effect has been accounted for in various theoretical investigations using hydrodynamic expansion models. [27]

In the next section, the process of plasma formation is discussed in more detail. Following that, the particulars of the ultrafast laser ablation experiment are outlined including the main diagnostic tool used; the Langmuir probe. The results of these experiments are subsequently presented along with a discussion in the context of the outlined theories.

3.2 Simple analytical models of laser ablation

In order to remove an electron from a solid, an amount of energy must be applied which is in excess of the binding energy of that solid. A high powered pulsed laser can be used to remove a large amount of matter from a solid material in a process known as ablation. A consequence of this ablation, is the formation of an partially ionized gas known as a plasma. The mechanism underlying this ablation, and indeed the expansion of the consequential plasma are governed by the specific laser parameters used.

In laser ablation, the laser field will penetrate into the material (to a depth known as the optical skin depth, δ or l_s) and strip electrons from the surface. After this initial ionization phase, energy is absorbed from the laser field by the free electrons through the inverse Bremsstrahlung process. This part of the ablation tends to be almost independent of the initial state of the solid material and depends mostly on laser pulse parameters such as peak intensity [22]. The next processes that occur in the ablation of materials are Coulomb collisions between electrons and ions. In this phase of the plasma formation, it is important to consider the temporal duration ($\Delta\tau$) of the laser pulse. For example, the typical time scale for energy transfer due to these collisions (τ_c) is on the order of picoseconds. Thus, the formation of a plasma in the presence of the laser pulse whose temporal duration is longer than the collision time will differ from a laser pulse whose temporal duration is shorter than the collision time [3].

In the long pulse case, the laser field will initially ionize the material on the rising edge of its intensity envelope. Once the ionization has occurred and electrons have been liberated from the solid, a process known as inverse Bremsstrahlung occurs whereby the electrons receive a gain in kinetic energy by absorbing energy from the laser field. This gain in kinetic energy results in an increased collision frequency between electrons and ions which further increases the degree of ionization causing an increase of electron density. This continues until the electron density reaches

a value known as the critical density where the plasma becomes opaque to laser light. However, at this point in time, the plume is expanding into the surrounding environment and the laser field is still present. This expansion causes a reduction in electron density to below the critical density and the laser field is now able to propagate into the plume. The propagation causes further inverse Bremsstrahlung absorption which increases the density again to the critical density. This cyclical process continues until the laser pulse terminates and once that happens, the plume expands into its surrounding environment.

In the short pulse case, the laser pulse has terminated before collisions can occur. In this case, where the laser field is intense enough, the initial ionized electrons are heated to energies well in excess of the Fermi energy where they can escape far from the surface of the target. These electrons result in the development of an electric field which causes the rapid ejection of ions from the target surface. The resulting recoil will be distributed by phonons in the target lattice. Also, the ponderomotive shift induced by the laser field penetrating into the solid will cause electrons to be pushed further into the solid which will displace ions. The resulting distribution of energy will cause thermalisation of the lattice resulting in a second plasma plume which generally behaves like a thermal fluid [7, 9]. The plasma formation is outlined below in Figure 3.2

3.2.1 Initial ionization of solids

The removal of an electron from the atoms in a solid can only occur if the electron gains an energy in excess of the binding energy of the atoms in the material, or if the binding energy of the material is lowered artificially. However, the processes by which the electron receives this energy can be quite different. In the case of ionization by a laser, two principal methods can be defined.

The first is the case of photoionization, where the electron gains all of its energy

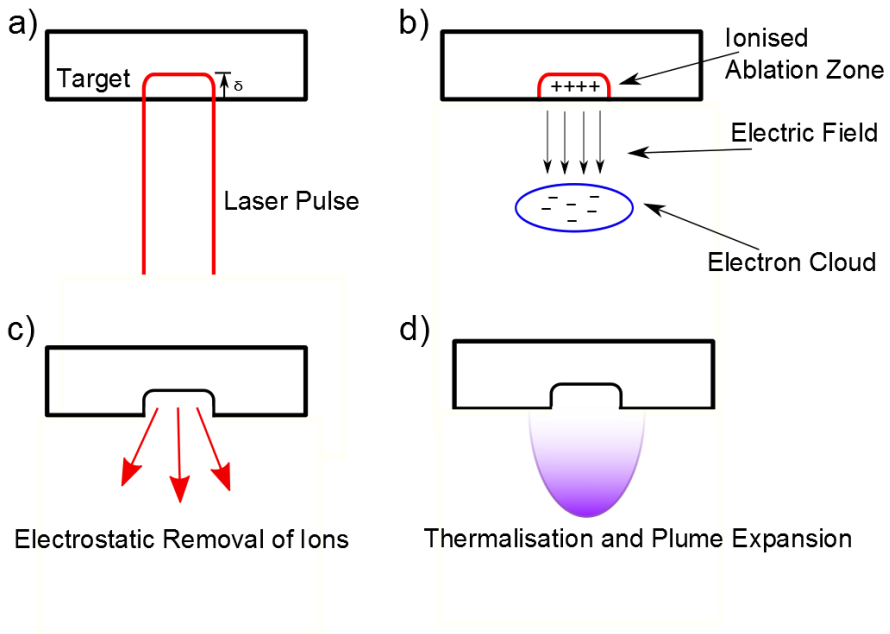

Figure 3.1: Illustration of plasma formation process by ultrafast laser ablation. a) the laser irradiates and penetrates into the material. b) highly excited electrons escape far from the target surface. c) ions are pulled from the target surface by the Coulombic force of the electrons. d) after the laser pulse, remaining electrons transfer energy and momentum to the target, heating it up and creating an expanding plume.

directly from the field of the laser. Even in this case, several sub-classes of ionization can be defined similar to those presented in chapter 4, section 4.3. The first is direct photoionization whereby a photon whose energy is greater than the binding energy of the atoms in the solid transfers all of its energy to an electron which becomes liberated from its parent atom. The number of electrons produced by this process will be directly proportional to the laser intensity. In multiphoton ionization, several photons collectively transfer their energy to a single electron such that it can be liberated. The probability of an electron absorbing N photons is proportional to I^N where I is the intensity of the laser field [28]. At very high intensities, the potential barrier between the solid and the continuum can be lowered by the laser field so that the electron can tunnel through it. This is known as 'tunnel ionization' and is proportional to both the intensity and the wavelength of the laser source [29].

A second principal method by which the electron becomes ionized exists and this employs collisions between the target and particles, principally electrons in the current context. That is, the electron gains initial energy from the laser field and then through collisions with other electrons in the solid, liberates other electrons. While the importance that this ionization scheme plays compared to conventional multiphoton ionization is the source of significant debate in the literature, a consensus seems to be that in the case of ultrafast laser ablation, the contribution of avalanche ionization is inversely proportional to the laser pulse duration [30].

3.2.2 Penetration of the laser field into the solid: The skin effect

No transfer of energy between ionized electrons and ions occurs during the laser field and so the laser pulse effectively interacts with a material of constant density. Thus, the penetration of the electromagnetic wave of the laser field into the material can be found by solving Maxwell's equations in the appropriate way. Inside the material, the laser field decays exponentially in the form [22]:

$$E(z) = E_o e^{-z/\delta}$$

where z is the target normal direction, $z = 0$ represents the target surface and E_o is the maximum field strength. This equation holds for all $z < 0$. δ is a parameter known as the skin depth and is typically given by:

$$\delta = \frac{c}{\omega\kappa}$$

where ω is the laser frequency and κ the extinction co-efficient (the imaginary component of the complex refractive index).

3.2.3 Electrostatic ion removal from the lattice

Electrons with a kinetic energy in excess of the Fermi energy will escape far from the target surface. A strong electric field will then be set up between those electrons and the parent ions left behind in the cratered lattice. The strength of this ambipolar electric field will be governed by the electron kinetic energy (ϵ_e) and the gradient of the electron density direction normal to the target [3].

$$E_a = -\frac{\epsilon_e}{e}\frac{dn_e}{dz} \tag{3.1}$$

Also, the ponderomotive force due to the electric field can be written as:

$$F_p = -\frac{2\pi e^2}{m_e c\omega^2}\Delta I \tag{3.2}$$

However, at traditional laser ablation intensities ($\approx 10^{14}$ Wcm^{-2}), the electrostatic force is much higher than the ponderomotive force. If the electrostatic field is higher than the binding energy of the material, ions will be pulled out of the surface. These ions will reach a maximum kinetic energy given by [22]:

$$\epsilon_i = Z\epsilon_e \tag{3.3}$$

The time taken to accelerate the ions to their maximum kinetic energy can be found from the equation:

$$t_{acc} = \frac{l_D}{v_i} \tag{3.4}$$

where l_D is the characteristic Debye length given by $\frac{1}{\omega_p}\left[T_e - \epsilon_{esc}/m_e\right]^{1/2}$ and v_i is the ion velocity found from Newton's 2^{nd} law.

$$\frac{dp}{dt} = eE_a \tag{3.5}$$

$$t_{acc} = \frac{2}{\omega_{pe}} \left(\frac{m_i}{m_e}\right)^{1/2} \left(\frac{T_e - \epsilon_{esc}}{T_e - \epsilon_{esc} - \epsilon_b}\right)^{1/2} \tag{3.6}$$

There are now two situations to be considered. One, where the t_{acc} term is longer than the temporal pulse duration $\Delta\tau$ and one where the acceleration time is shorter than the pulse duration. The former case occurs when the intensity of the laser pulse is below what is known as the ablation threshold. To fully define the ablation threshold for metals and semi-conductors, it is necessary to first discuss the electron temperature in the ablation region after the laser pulse. Because the pulse width is so short, the electrons do not conduct heat to the lattice during the laser pulse. Just after the laser pulse, the electrons and ions have not reached thermal equilibrium and so each species has a separate temperature [19]. This is the basis for the well established 'Two temperature' model. This model treats the evolution of the ion temperature as being linearly related to the temporal evolution of the electron temperature. It can be shown from this model (section 3.2.4) that at laser intensities well above the ablation threshold, there is a lowering of the electron temperature due to losses from ion heating.

3.2.4 Electron heating in the skin layer: The two temperature model

Given the fact that the electrons have no time to conduct heat to the lattice during the laser pulse, and that the electronic heat capacity is lower than the lattice heat capacity, the electrons can be heated very quickly to a high temperature in the skin layer (well in excess of the Fermi energy). The spatial and temporal evolutions of the temperature in the skin layer can then be described by the following one-dimensional,

two temperature heat conduction equations [19]:

$$C_e \frac{\partial T_e}{\partial t} = -\frac{\partial Q(z)}{\partial z} - \gamma(T_e - T_i) + S \tag{3.7}$$

$$C_i \frac{\partial T_i}{\partial t} = \gamma(T_e - T_i) \tag{3.8}$$

where $Q(z)$ and S are given by:

$$Q(t) = -k_e \frac{\partial T_e}{\partial z}, S = I(t) A \alpha e^{-\alpha z} \tag{3.9}$$

and γ is a parameter characterising the electron-lattice coupling strength and k_e is the electron conductivity. $Q(z)$ is the heat flux and S is the laser based source term in the partial differential equation. C_e and C_i are the electron and ion heat capacities (per unit volume), A and α are the surface absorptivity and the material absorption co-efficient respectively.

During the rising edge of the laser pulse, the electrons are heated to the Fermi temperature and so the heat capacity of the electrons can be considered constant [19]. The evolution of the electron temperature is given by:

$$\frac{\partial T_e}{\partial t} = \frac{\partial}{\partial z} D \frac{\partial}{\partial z} T_e - \frac{T_e - T_i}{\tau_e} + \frac{I A \alpha}{C_e} e^{\alpha z} \tag{3.10}$$

$$\frac{\partial T_i}{\partial t} = \frac{T_e - T_i}{\tau_i} \tag{3.11}$$

where D is the electron thermal diffusivity, $\tau_e = C_e/\gamma$ is the electron heating time

and $\tau_i = C_i/\gamma$ is the ion cooling time. The following initial and boundary conditions are used:

$$T_e(z, t = -\infty) = T_i(z, t = -\infty) = T_o = 0 \tag{3.12}$$

$$\frac{\partial T_e(z=0)}{\partial z} = \frac{\partial T_e(z=\infty)}{\partial z} = 0 \tag{3.13}$$

An analytical solution to these equations describing the thermalization after the laser pulse is given by [19]:

$$T_e = T_{eq} + \Delta T \left(\frac{\tau_L}{\tau_e + \tau_i}\right) e^{-t/\tau_{eq}} \tag{3.14}$$

$$T_i = T_{eq} - \Delta T \left(\frac{\tau_L}{\tau_e + \tau_i}\right) e^{-t/\tau_{eq}} \tag{3.15}$$

where $\tau_{eq} = \tau_i\tau_e/(\tau_e + \tau_i)$ and $T_{eq} = \frac{\tau_e T_e(0) + \tau_i T_i(0)}{(\tau_i + \tau_e)}$. T_{eq} is known as the equilibrium temperature and ΔT is the initial temperature difference. The initial temperatures are given by:

$$T_e(0) = \frac{I_o A \alpha}{DC_e} \frac{1}{\beta^2 - \alpha^2} \left[e^{-\alpha z} - \frac{\alpha}{\beta} e^{-\beta z}\right] \tag{3.16}$$

$$T_i(0) = \frac{F_o \alpha}{DC_e} \frac{1}{\tau_L + \tau_i} \frac{1}{\beta^2 - \alpha^2} \left[e^{-\alpha z} - \frac{\alpha}{\beta} e^{-\beta z}\right] \tag{3.17}$$

where β is a term that depends on D. F_o is the laser fluence.

3.2.5 Ablation thresholds for metals

The minimum energy required for an electron to escape a solid material is known as the work function. In order for that electron to electrostatically pull an ion from the remaining lattice, it must gain an additional energy that is greater in magnitude than the atomic binding energy of the ion. It has also been stated, that during the rising edge of the laser pulse, electrons that escape are those that have been heated to a temperature in excess of the Fermi energy [3]. Thus, the ablation threshold is defined as the point at which electrons have been heated to exactly the Fermi energy. After the laser pulse, thermalisation occurs and heat is conducted from the electrons to the lattice. There are two situations that can be considered. One is where the heat penetration depth l_s is less than the optical penetration depth δ. The other is the reverse situation (i.e $l_s > \delta$). In general, there are two conditions for the absorbed laser energy per unit area can be expressed as follows [22]:

$$F_{th} = \frac{3}{4}\frac{\delta n_e}{A}(\epsilon_b + \epsilon_{esc}) = n_e \Omega \delta \qquad \delta \gg l_s \tag{3.18}$$

$$F_{th} = \frac{3}{4}\frac{l_s n_e}{A}(\epsilon_b + \epsilon_{esc}) = n_e \Omega l_s \qquad \delta \ll l_s \tag{3.19}$$

The distribution of absorbed energy inside the penetration layer of the material is given by:

$$F_o = F_{th} e^{-\delta z} \qquad \delta \gg l_s \tag{3.20}$$

$$F_o = F_{th} e^{-l_s z} \qquad \delta \ll l_s \tag{3.21}$$

From this, it can be seen that there are two separate sub-linear dependances of

the depth of the ablated mass on laser fluence.

3.3 Langmuir probe operation

A biased wire tip can be immersed into a laser plasma and used as a diagnostic tool. The general procedure is to put the wire at a bias relative to some ground reference and to measure the current that flows from the plasma to the probe as a function of time. This current will be affected by the bias voltage and the probe response will allow for the calculation of plasma parameters such as plasma potential [31], electron temperature [32], electron density [33] and ion density [18]. The applicability of an electrostatic probe varies over a large range of background pressures [34] and offers the benefit of a highly localised, temporally resolved measurement of important plasma parameters. An additional benefit of the electrostatic probe method is its experimental simplicity. However, the benefits of using probes is offset somewhat by the complexity in the post-analysis of data. Under certain conditions, the electic field of the probe itself will disturb the plasma and in post analysis, correction factors are needed for a proper interpretation of the data [35].

The use of electrostatic probes dates back to the work of Crookes in the late 19th and early 20th centuries. Here, probes were used to measure the temperature and density of electrons in a gas discharge. The analysis that accompanied these experiments however tended to underestimate the space potential of the discharge. In the 1920s, Irving Langmuir created a new, more robust analysis which is still used today. Hence, electrostatic probes used in plasma experiments are known as 'Langmuir probes'. The analysis of Langmuir is confined to low temperature plasma and to parameters whose velocity distribution is Maxwell-Boltzmann [36]. Advances such as double probes and improved analysis have allowed in recent times for more reliable measurements to be made with probes. However, in order for probes to be useful, assumptions are placed on the plasma with and without the probe in place. To start with, the plasma is considered to be infinite in extent and quasi-neutral when the probe is not there. The mean free paths of the electrons and ions must be

much longer than any other lengths considered in the experiment. Also, the extent of the region in the plasma that the probe disturbs is known as the sheath and its boundary is well defined [1].

The analysis of Langmuir was confined to plasmas with large spatial extent (large volume) and ones which were steady state in nature. A laser produced plasma however is small in extent and is highly energetic and transient in nature. Added to this is the flowing, expanding nature of the plasma plume. The result of all this is a deviation in the calculated values from the real ones [36]. For the most part of this work, measurements were made in the far field where the expansion and transient nature of the plasma is not expected to influence the calculated parameters too much [23]. Given the right conditions, Langmuir probe analysis can be applicable to the near field region of the plasma plume which is highly transient [33].

3.3.1 The I-V Characteristic

The quasi-neutrality conditions exists if the plasma is considered over its whole volume. If looked at closer, particularly on a length scale comparable to a parameter known as the Debye length, charge imbalance can occur [1]. If the plasma is considered on this length scale, it can have an associated potential known as the plasma potential. The flow of current from plasma to probe will be influenced by the difference between the potential applied to the probe and the plasma potential. If the plasma potential is V_p and the probe potential (bias) is V_b, then there are three regions to consider [36]:

Saturation

The first two regions to consider are the cases where the plasma potential is either much smaller, or much larger than the probe bias.

If the probe potential is much lower than the plasma potential ($V_p \gg V_b$), all electrons are repelled from the probe and the collected current is known as the *ion saturation current*. According to theory, at a large negative potential, the probe

should register a small current that is independent of bias voltage. It is only when the bias voltage is made equal to the plasma potential that ions start to be repelled and the collected current deviates from the value of the ion saturation current. However, in reality it is sometimes the case that the ion current will increase linearly with applied voltage even in the case there ($V_p \gg V_b$). This is due to the fact that the bias on the probe causes electrons to be repelled and a positively charged layer to form around the probe known as the sheath. The thickness of this sheath layer increases with probe voltage hence increasing the radial extent to which the probe can capture ions. The ion saturation current can be defined as:

$$I_{is} = \frac{1}{4} e n_i v_{i,th} A_{probe} \tag{3.22}$$

where $v_{i,th} = \sqrt{8kT_i/\pi m_i}$ is the thermal velocity of the ions. If the electron temperature is much greater than the ion temperature, the area of the sheath becomes much larger than the area of the probe surface due to the fact that the Debye length (λ_D) depends on electron temperature ($\lambda_D = \sqrt{\epsilon_o kT_e/e^2 n_e}$). In this case, ions will be repelled by the large positively charged sheath and the only ions that will register a current signal on the probe will be those that have acquired a velocity equal to what is known as the *Bohm velocity* [1]. In this case, the ion saturation current takes a different value:

$$I_{is} = 0.6 e n_i \sqrt{\frac{kT_e}{m_i}} A_{probe} \tag{3.23}$$

In a very similar way, when the probe bias is much higher than the plasma potential ($V_p \ll V_b$) the probe will register the electron saturation current given by:

$$I_{es} = \frac{1}{4} e n_i v_{e,th} A_{probe} \tag{3.24}$$

It can be seen that in this case, the thermal speed of the electrons will be ∼200 times higher than the thermal speed of the ions (for example, argon) owing to the differences in their mass. It should then be expected that the electron saturated current should be larger than the ion current by a factor of 200. In practice, it is found that the electron to ion saturation current ratio is mass dependent but is typically in the range 100 - 500.

Transition

In the region where the probe potential and the plasma potential are not too different from each other, the current induced in the probe will be highly dependent on the probe voltage. The electron current induced in the probe in this region is given by:

$$I(V_b) = I_{es} e^{-e(V_f - V_b)/kT_e} \tag{3.25}$$

The ion current collected by the probe in this region is given by:

$$I(V_b) = -I_{is} e^{-e(V_f - V_b)/kT_i} \tag{3.26}$$

Where V_f is the potential at which the probe collects no current. However the ions are assumed to remain cold and so ($I(V_b) \simeq -I_{is}$). The measured current is the summation of both the electron and ion currents and so,

$$I_{electron} = I_{measured} - I_{is} \tag{3.27}$$

Thus,

$$ln|I - I_{is}| = \frac{q}{kT_e}(V_b - V_f) \tag{3.28}$$

Where e is the electric charge and $q = Ze$ is the ion charge state. It can be seen from Equation 3.28 that the electron temperature can be directly calculated from a plot of $\ln|I - I_{is}|$ vs $(V_b - V_f)$. Knowing the electron temperature, the density can then be calculated from the electron saturation current.

Orbital Motion Theory

The above analysis, which is known as Langmuir Analysis, allows for the calculation of electron temperatures and densities from a measured I-V curve. However, the theory makes the assumption that every electron or ion that falls into the region of extent of the sheath will be collected by the probe. However, it could be the case that an ion/electron will enter the sheath region but not be collected by the probe. Figure 3.3.1 below shows a toy calculation of the trajectory of two silicon ions in the field of a Langmuir probe biased to -80 V. It can be seen that particles of a very high kinetic energy can pass into the Debye sheath and not be collected by the probe. Similarly, the initial kinetic energy of the ions could be such that the ions penetrate the Debye sheath and enter into a stable or unstable orbit of the probe. If the initial kinetic energy of the ion is given by $\frac{1}{2}mv_o^2$, the conservation of energy gives $\frac{1}{2}mv_o^2 = -qV_o$. If V_p is the probe voltage, h_a is the distance of closest approach and h_o is the initial vertical distance from the probe to the ion, conservation of momentum and energy gives [37]:

$$\frac{1}{2}mv_o^2 = \frac{1}{2}mv_a^2 + qV_a = -qV_o \tag{3.29}$$

and

$$h_a v_a = h_o v_o \tag{3.30}$$

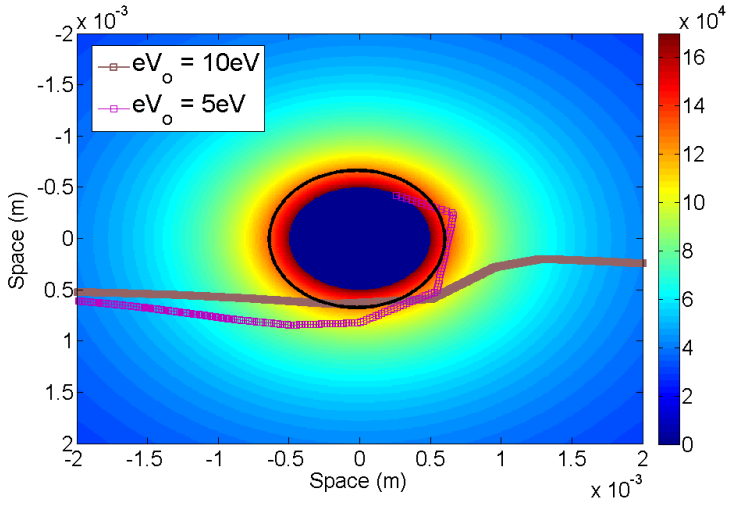

Figure 3.2: Calculation of the trajectories of two ions moving in the field of a Langmuir probe. Both ions had the same initial starting location (x_o=-4.8 mm, y_o=0.5 mm). The black circle around the probe shows the extent of the Debye sheath.

Solving for h_o gives:

$$h = h_a \left(1 - \frac{V_a}{V_o}\right)^{1/2} \tag{3.31}$$

If $a < r_p$ where r_p is the probe radius, then that ion is collected by the probe and a current is measured. The contribution to the current for ions within a small velocity range is then given by:

$$dI = 2\pi r_p l q (1 - \frac{V_{r_p}}{V_o})^{1/2} dn \tag{3.32}$$

where l is the length of the probe. For a Maxwell-Boltzmann distribution of ions,

$$dn = n_o \left(\frac{m}{2\pi kT}\right) e^{mv^2/2kT} 2\pi v dv \tag{3.33}$$

which gives,

$$dI = \frac{2n_o r_p lmq}{kT} v^2 e^{mv^2/2kT} (1 - \frac{V_{r_p}}{V_o})^{1/2} dv \tag{3.34}$$

Setting $\eta = qV_p/kT$, the total current is then found by integrating dI to yield:

$$I = 2\pi n_o r_p leq \left(\frac{kT}{2\pi m}\right)^{1/2} \left(\frac{2\sqrt{\eta}}{\sqrt{\pi}} + e^{\eta}\text{erfc}(\sqrt{\eta})\right) \tag{3.35}$$

At large η, $[2\sqrt{\eta}/\sqrt{\pi} + e^{\eta}\text{erfc}(\sqrt{\eta})]$ approximates to $2(1+\eta)^{1/2}/\sqrt{\pi}$ to give,

$$I = 2\pi n_o r_p leq \left(\frac{kT}{2\pi m}\right)^{1/2} \frac{2}{\sqrt{\pi}} \left(1 + \frac{qV_p}{kT}\right)^{1/2} \tag{3.36}$$

Figure 3.3 shows graphically the approximation for large η. From Orbital Motion theory, a plot of I^2 vs V_p will give a linear region when $\eta > 2$. Again, once the ion saturation current is subtracted to give the electron current, the slope of this linear region will yield the electron density and once that is known, the intercept will yield the temperature. A sample analysis is given graphically in Figure 3.4

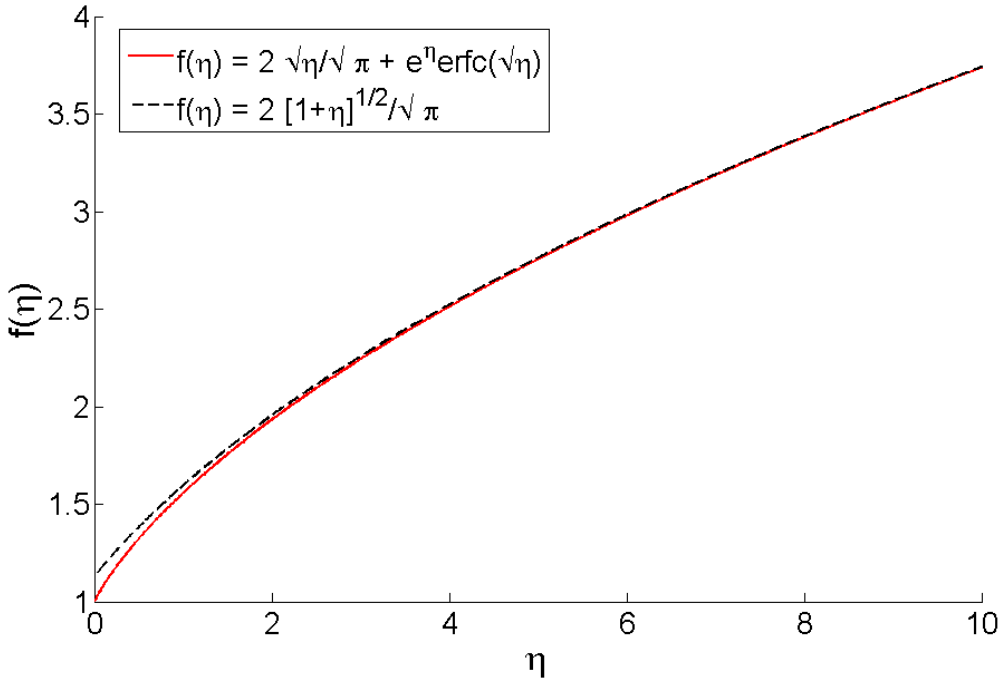

Figure 3.3: Plot showing how Equation 3.35 reduces to Equation 3.36 with large η

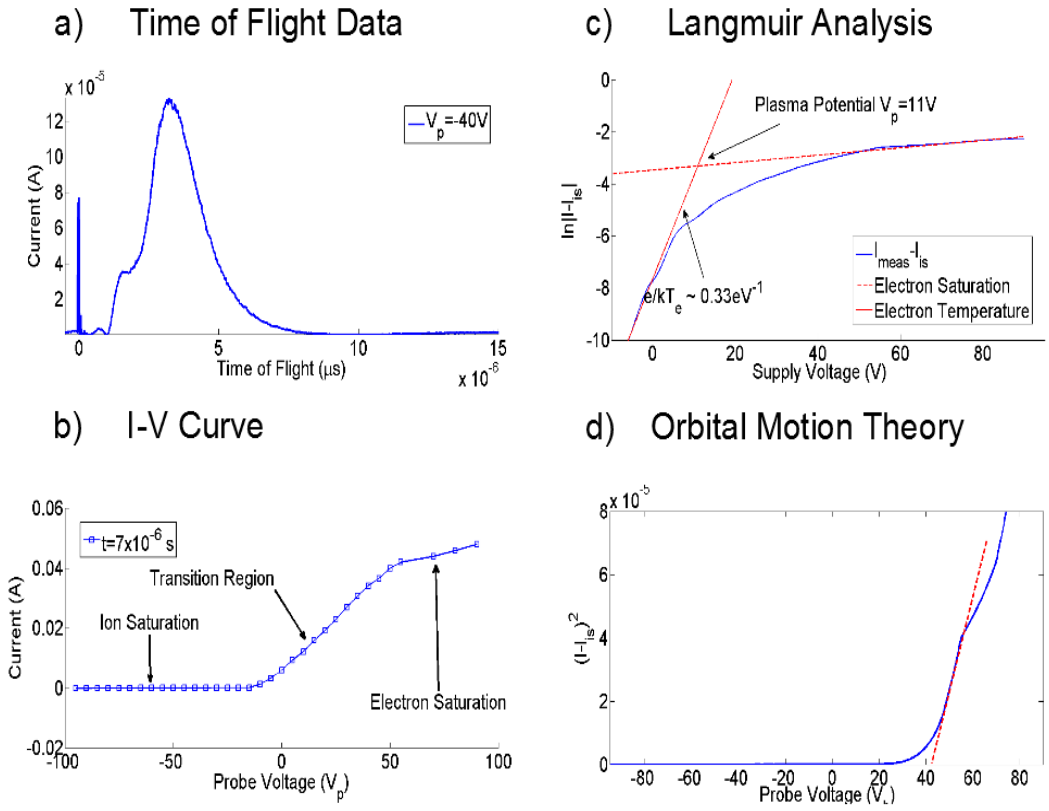

Figure 3.4: An example of the analysis procedure for the Langmuir probe. a) a time of flight trace is determined directly from the probe for a variety of probe voltages. b) at a particular time, the current versus probe voltage is plotted. c) the ion saturation current is subtracted and the log of the current is plotted against the probe voltage. d) the square of the electron current is plotted against voltage.

3.4 Experimental setup

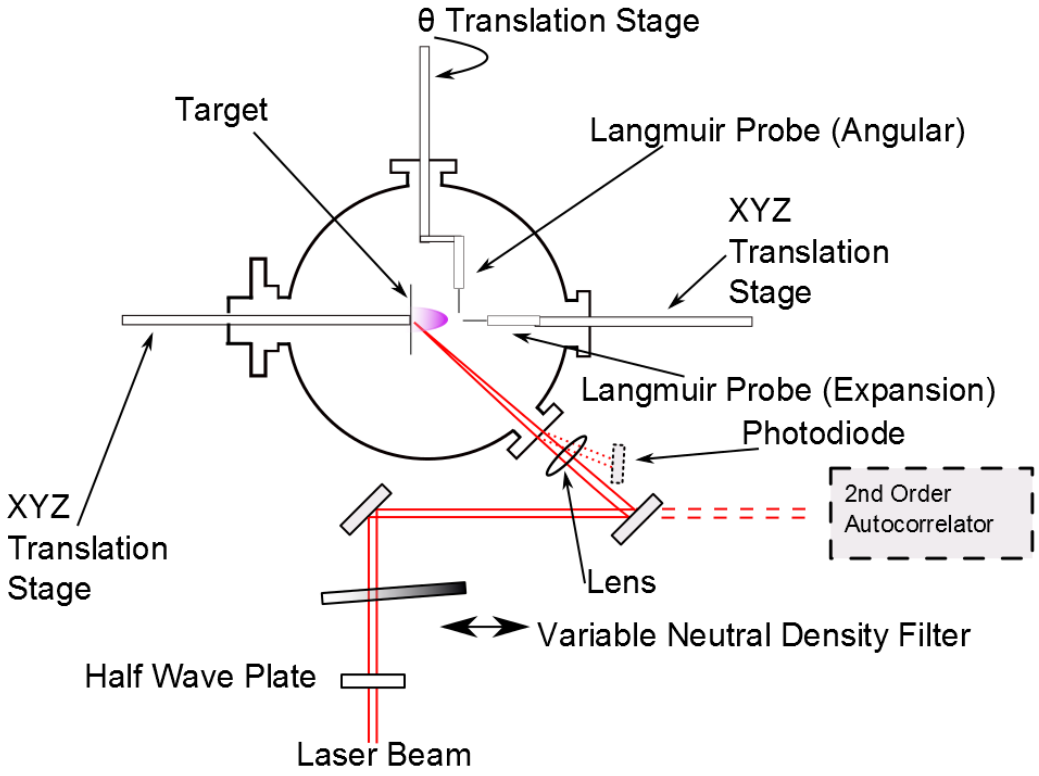

Figure 3.5: Experimental schematic

The laser system

The experimental system for this work is shown in Figure 3.5. The laser system has been described in greater detail in chapter 2. The output of the Coherent Legend Elite was 1 ± 0.1 mJ and the pulse width was measured to be 32 ± 5 fs. The pulse energy of the laser was varied using a continuously variable neutral density filter. It was confirmed through direct measurement that the broadening of the pulse did not vary as a function of lateral position of the neutral density filter. The laser was passed through an uncoated, 5 mm BK7 vacuum window and focussed at a 45^o de-

gree angle onto the target with a 250 mm plano-convex lens. The reflection from this window was used to trigger a photodiode which was connected to a Tektronix TDS 3012 300 MHz oscilloscope. The purpose of the photodiode was to provide a trigger pulse or t_o for the oscilloscope and also to measure the variation in the pulse energy on a shot to shot basis. A half-wave plate was placed in the path of the beam to rotate the polarisation of the laser beam. The energy loss through the half-wave plate, the window and the mirrors gave an on-target pulse energy of 750 μJ. To measure the pulse broadening, the pulse width was measured directly at the output of the amplifier and then again after the beam had travelled freely through air a distance of 3 m and found to change by 1 fs on average which is within the margin of error of the autocorrelator (in the absence of optical components). The optical layout was re-created just after the output of the amplifier on a flat optical table and the pulse width was measured using the APE Pulsecheck (see Chapter 2) after each optical component using a glass slide pick-off. It was found that the pulse broadened by a total of 30 fs after transmission through the components to give an on-target pulse width of 62 $fs \pm 5$ fs. The optical leakage through the last routing mirror (shown in Figure 3.5) before the vacuum chamber was used to trigger the autocorrelator to monitor the variation in the pulse width over time.

The vacuum system

The vacuum system consisted of a Kurt J Lesker spherical vacuum chamber (O.D 30 cm). The chamber had 10 centre pointing radial conflat flange ports of various sizes (2 x 150 mm, 4 x 100 mm, 4 x 40 mm). With the exception of two windows (a viewport and a laser window) all other components were home-made or back engineeered specifically for this experiment. The target was mounted onto an in-vacuum manipulator which could move in the x,y and z direction with a precision of $\pm$.01 mm using micrometer translation stages. The angle resolved Langmuir probe was connected to a vacuum manipulator. The vacuum manipulator was connected to a rotational translation stage with a precision of $\pm 1^o$. The other Langmuir probe,

which was used to measure the expansion dynamics, was connected to an in-vacuum XYZ translation stage with a precision of $\pm.01$ mm. The air was evacuated from the chamber using a 'Provac PT50 ' turbomolecular pump backed by an 'Edwards 28' backing pump. The lowest base pressure achieved in the chamber was 5×10^{-6} mbar and typical operating pressures were in this range. High voltage vacuum compatible BNC feedthroughs were used to bias each Langmuir probe separately. Both the main vacuum chamber and the target were electrically grounded. The vacuum system is photographed in detail and shown in Figure 3.6.

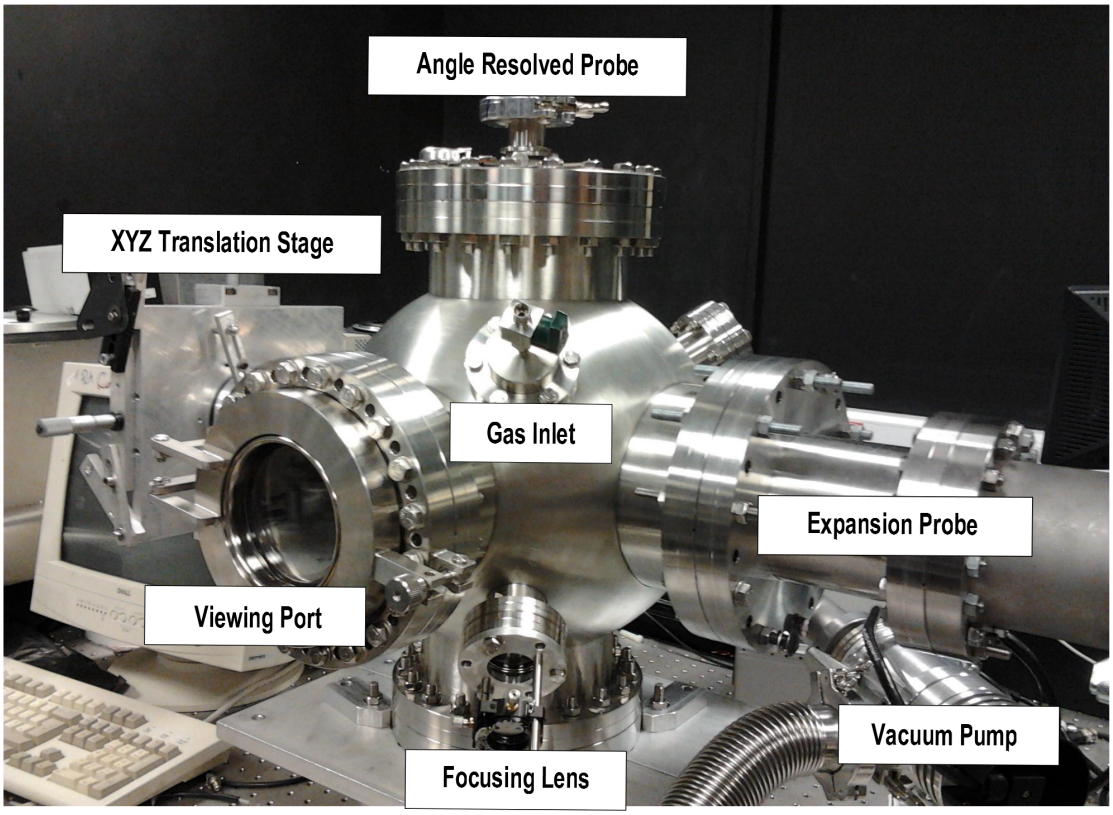

Figure 3.6: Photograph of experimental setup.

The Langmuir probe

The Langmuir probes used in this work were home made and constructed specifically for these experiments. In terms of composition and construction, the probes were identical. Each probe consists of a 0.5 mm thick, 4 mm long tungsten wire tip connected to a long co-axial cable. The probes were biased independently using power supplies with maximum potential of ±400 V and 1 A full scale current. One probe (the 'Expansion Probe') was placed facing the centre of the target in the direction of the plasma expansion. The probe was connected to an XYZ translation stage which had a full Z-direction range of 500 mm in steps of no less than 1 mm. The second probe ('Angular Probe') was placed perpendicular to the plasma expansion, a distance of 50 mm from the target. This probe was connected to a rotational translation stage with a precision of $\pm 1^o$. Another purpose of having two probes was to have a reference. During one set of experiments, say the angle resolved experiments, the other probe would be placed at a fixed position and distance from the target at a fixed bias to monitor and ensure that the ablation conditions were constant. Care was taken to ensure that the bias on the reference probe did not interfere with the plasma nor the measurement probe. To ensure that the probes did not talk to each other, a variety of tests were performed. Namely, the probes were separated in space and the reference probe was not heavily biased (just enough to reject electrons). Extensive testing was done to ensure that the signals collected by the measurement probe were the same whether the reference probe was in place or not. It was also noted that two probes could be brought quite close to each other before they started interfering with each other and that this distance depended on laser intensity and probe voltage. However, even in the most extreme circumstances (highest intensity, maximum bias), the probes could be brought within 5 mm of each other. In practice the probes were generally kept more than 5 cm apart and the voltage of any probe during all experiments never exceeded ±250 V. In this way, it was assumed that the reference probe did not interfere with the measurement probe and gave an accurate depiction of the ablation conditions. Of course, this was only useful during experiments that measured the current as a function of some

probe variable. Once it was verified that reference signal remained constant, this technique was not used for intensity and polarisation measurements. The probes were connected to an oscilloscope through a 'Bias Tee' circuit which is described in detail below. The data were then saved from the scope to a computer using a custom written labview program in ASCII format which was then post-analysed in MATLAB. A photograph of one of the Langmuir probes used is shown in Figure 3.7.

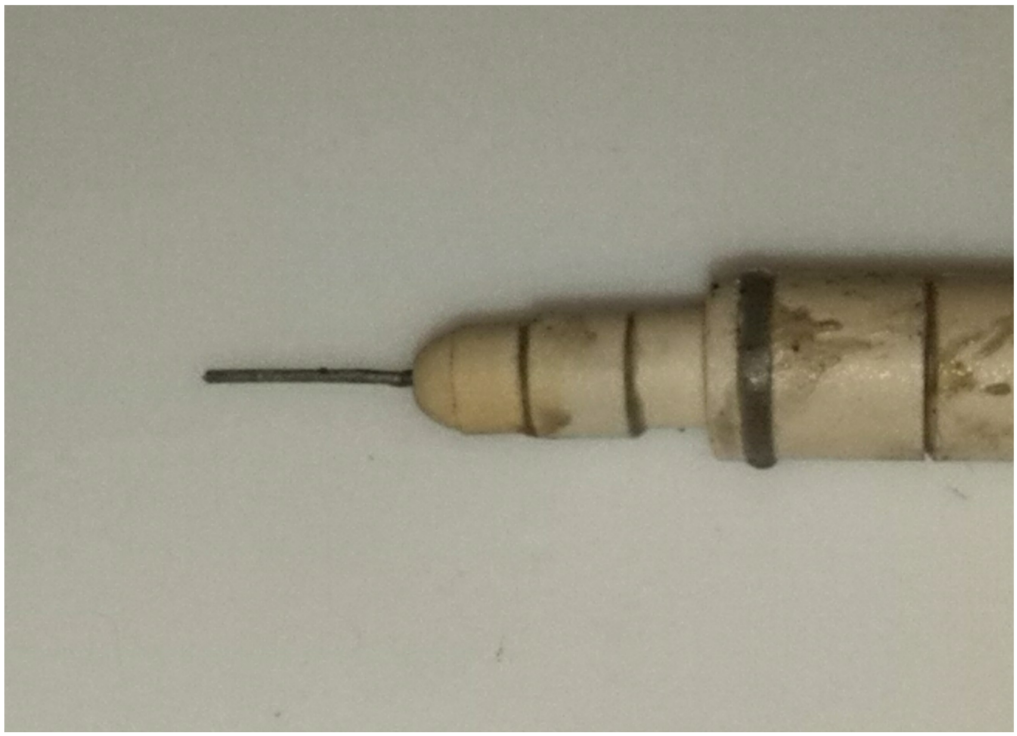

Figure 3.7: Photograph of Langmuir probe used in this experiment.

From time to time the probe became coated in by plasma deposited material and needed to be cleaned with alcohol. Evidence of this deposition is visible on the teflon jacket surrouding the probe in Figure 3.7.

Signal Acquisiton

The read-out circuit used for each probe is shown in Figure 3.8.

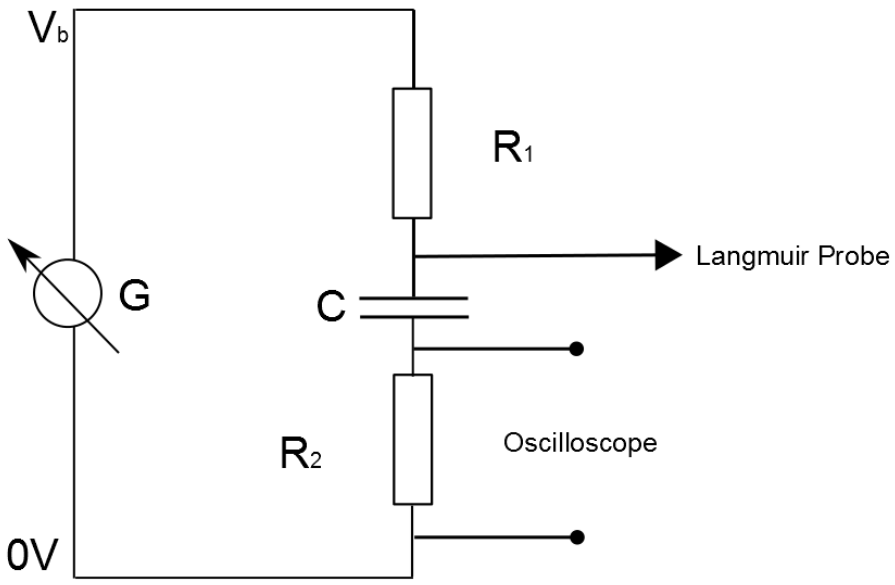

Figure 3.8: Read-out detection circuit for Langmuir probes. For these experiments, R_1 = 1.1 kΩ, R_2=50 Ω, C=1.1 μF.

When ions/electrons strike the probe, the current from the plasma splits into two paths, one through R_1 and the other through R_2. To calculate the current, the measured voltage drop across the oscilloscope is divided by the equivalent resistance to give:

$$I_{probe} = \frac{V_{meas}}{R_{eq}} \tag{3.37}$$

where R_{eq} is found by $R_{eq} = \frac{R_1 R_2}{R_1 + R_2}$

Experimental conditions

Figure 3.9 shows a typical ion signal collected by the Langmuir probe. Two peaks are clearly visible in the time of flight signal.

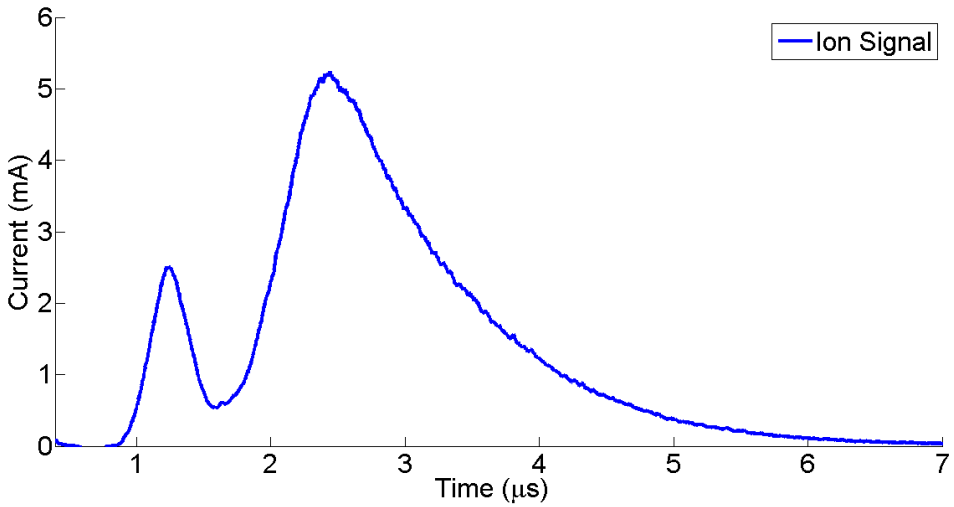

Figure 3.9: An example of a raw time-of-flight or TOF signal obtained with a negatively biased Langmuir probe. The applied bias was -100 V.

The on-target spot size was measured using optical microscopy to be $\sim 6 \times 10^{-4}$ cm^2 (shown in Figure 3.10 for an on-target pulse energy of 750 μJ. The appearance of the second peak in ultrafast ablation experiments has been reported in the literature in both Langmuir probe and Faraday cup measurements [7, 9]. Various papers have attributed the fast peak to impurities on the target surface [6]. Other papers have attributed the peak to space charge effects resulting from electrons in excess of the Fermi energy escaping far from the target surface and causing an electrostatic force acting on the ions and removing them from the lattice [9]. To investigate the nature of the fast peak, the laser was fired at the same spot on the target with a repetition rate of 1 kHz. The fast peak was observed to remain even after 300 laser shots indicating that the fast peak does not appear to be due to contamina-

tion. The shot to shot ion signal was found to vary greatly in the first 10 or so shots. After this the ion signal was found to remain relatively constant for $\sim$ 100 shots. At above $\sim$ 100 shots, the ion signal started to reduce rapidly, possibly due to cratering and confinement effects. The fast ion peak was observed to diminish more slowly as a function of laser shot than the slow ion peak. The ion signals were acquired by firing the laser at a rep rate of 1kHz and delaying the triggering of the oscilloscope such that the scope only started collecting after shot number 20. The ion signals recorded represented the average of 16 laser shots. It was determined by direct observation that the ion signal remained relatively constant during shots 20 - 36. This was observed to be true regardless of the on-target energy of the laser pulse.

Efforts were made to install a Pockels cell to control the number of shots / rep-rate directly. However, the resulting drop in energy / distortion of the beam profile / broadening of the pulse meant that the averaging of multiple shots approach was more convenient. The target was translated 1mm in either the vertical or horizontal direction such that the laser struck a fresh surface for each measurement.

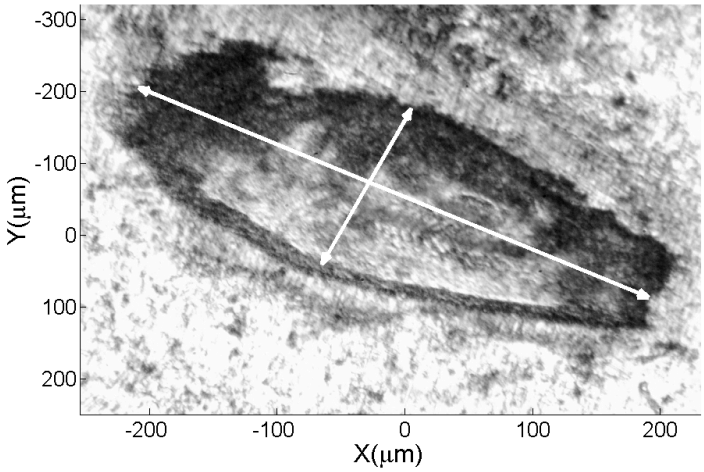

Figure 3.10: Microscope image of laser spot after $\sim$1000 shots. Estimated spot size is $6 \pm .04 \times 10^{-4}$ cm^2

3.5 Results: Ion and electron behaviour with fluence

In a first experiment, the ion and electron signals were measured as a function of laser fluence for silicon-targets. To measure ions, the probe voltage was set to -30 V and to measure electrons the probe was set to +30 V. All fluence measurements were made on the angle-resolved probe which was placed a distance of 50 mm from the target surface and at an angle of 0^o from the target normal. Time-of-flight traces for silicon ions as a function of laser fluence are shown in Figure 3.11

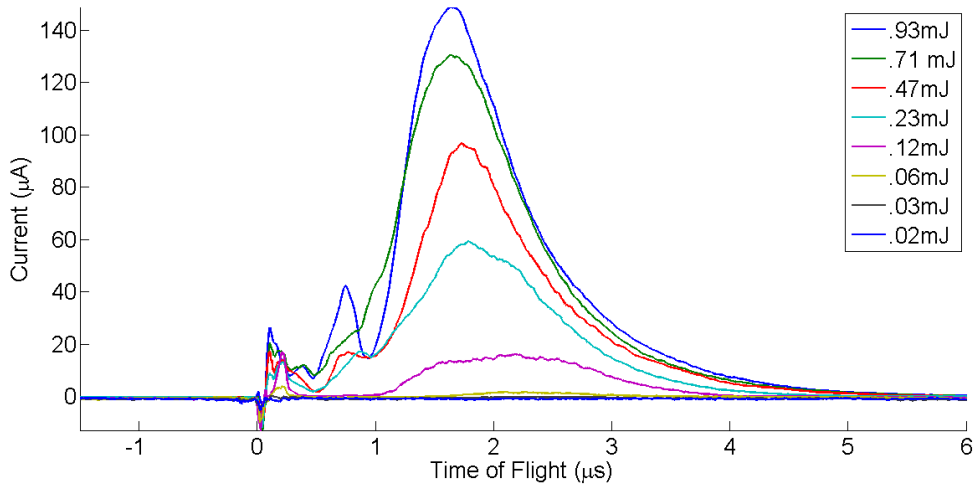

Figure 3.11: Time-of-flight (TOF) traces as a function of fluence for silicon ions showing appearance of double peaked structure.

From Figure 3.11 it is seen that three structures appear in the time of flight signals. The first, which is a generally broad feature appears at a time-of-flight of ~ 2 μs, is generally attributed to heavier, slower components of the plasma which appear due to thermalisation of the lattice [38]. The most probable velocity of this feature tends to increase as a function of fluence. When the fluence is increased, a narrower, higher energy feature becomes apparent at ~ 0.8 μs. This feature becomes sharper and better resolved as a function of increasing fluence. From the data, it

is unclear if the peak velocity of this feature changes with increasing fluence. A third feature is visible at $t < 0.4\mu$s. This feature which oscillates both positive and negative even though the probe bias is negative, has been reported in the literature before as being due to waves of high energy electrons / ions escaping from the plasma core [33, 39, 40]. The data in Figure 3.11 is in general agreement with data presented in the literature on ultrafast laser ablation [38]. Looking to the electrons, a similar trend appears, the electron signal is consistently higher than the ion signal and the peak velocity of the electron current increases with laser fluence.

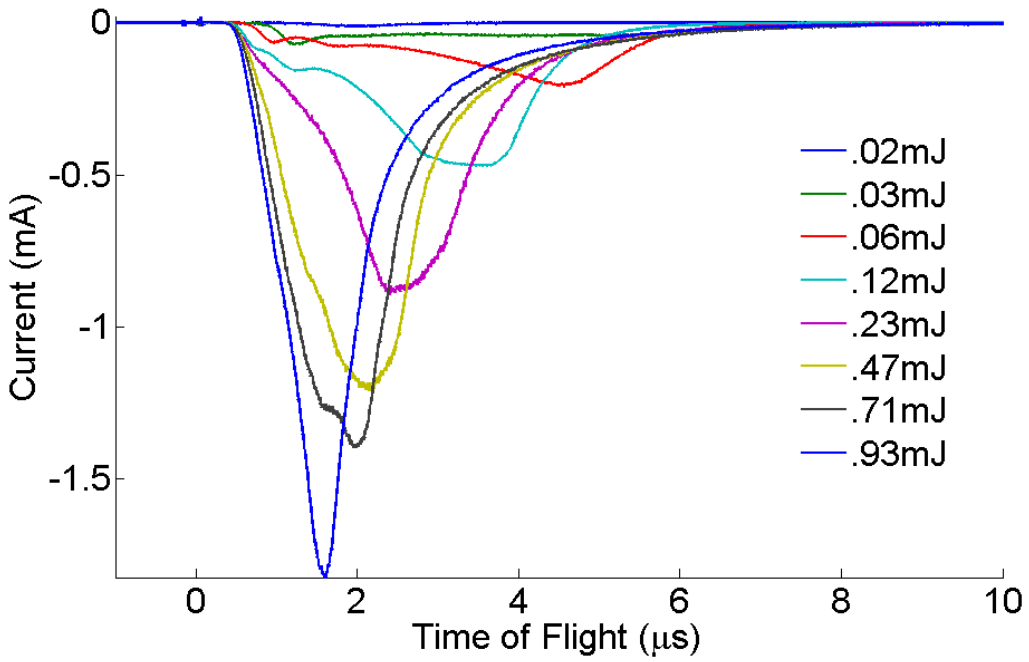

Figure 3.12: Time-of-flight traces with varying laser energies. Probe voltage now +30 V

In Figures 3.13 and 3.14, the particle yield as a function of intensity shows two separate sub-linear regimes for the slow peak of both the electrons and the ions, as predicted by the two temperature model (Section 1.3). Fitting a straight line to a semi-log plot of both regimes in the electron and ion yields gives a threshold fluence of ~ 66 mJ/cm^2.

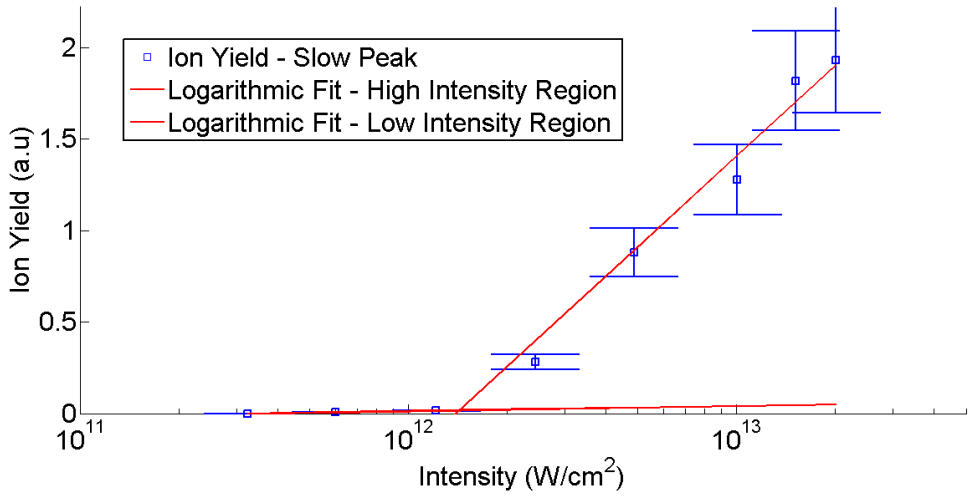

Figure 3.13: Ion yield as a function of intensity for the slow peak in the ion TOF signal

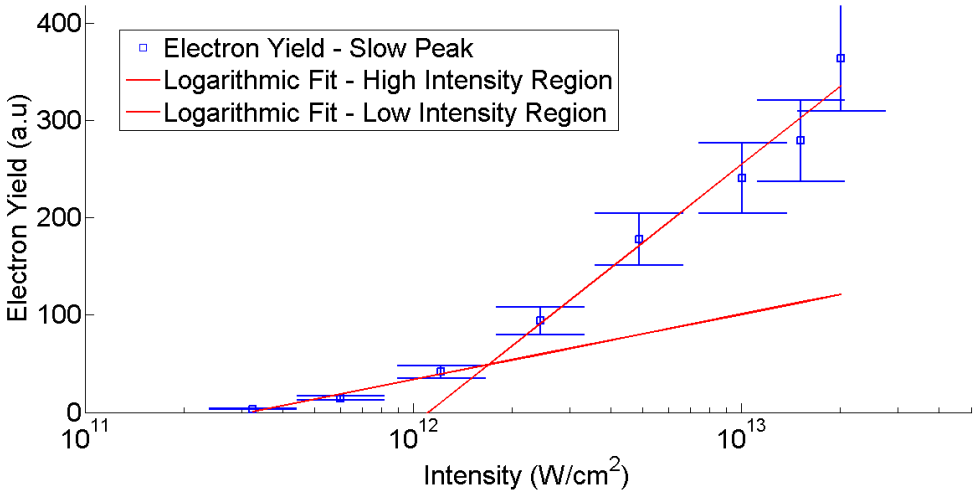

Figure 3.14: Electron yield as a function of intensity for the slow peak in the electron signal.

A different trend is shown in the case of the fast peaks as a function of fluence (Figure 3.15). In this case, the yield for both ions and electrons follows a straight line dependance on laser fluence, which is an indication that the fast peak is produced by non-thermal means.

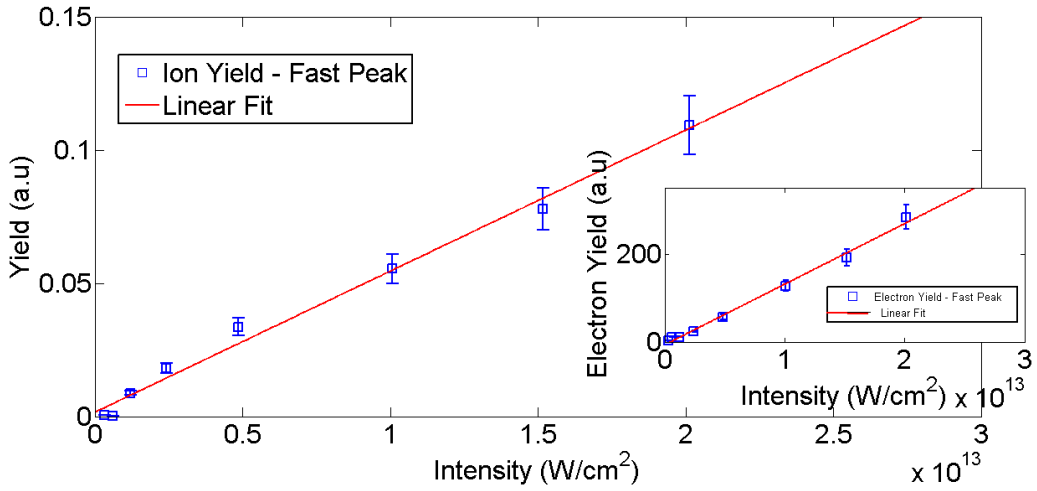

Figure 3.15: Ion yield as a function of intensity for the fast peak in the ion signal. Inset: Electron yield for fast peak as a function of fluence.

One interesting contrast between the time-of-flight distributions of ions and electrons is in the kinetic energy difference between the fast and slow peaks. It is seen from Figures 3.16 and 3.17 that there is almost a constant velocity difference between the fast and slow peaks in the ion signals, however for the electrons, the peaks both tend toward the same kinetic energy as laser fluence increases.

A mechanism that can explain the bi-modal structure of the plume is the creation of a time-dependent ambipolar electric field. Electrons that are heated to in excess of the Fermi energy can escape far from the target to distances comparable to the Debye Length λ_d. This can create a space charge layer which accelerates a small fraction of ions. The remaining plasma, dubbed the 'core', undergoes thermalisation and hydrodynamic expansion [22]. This model can be elucidated by treating the

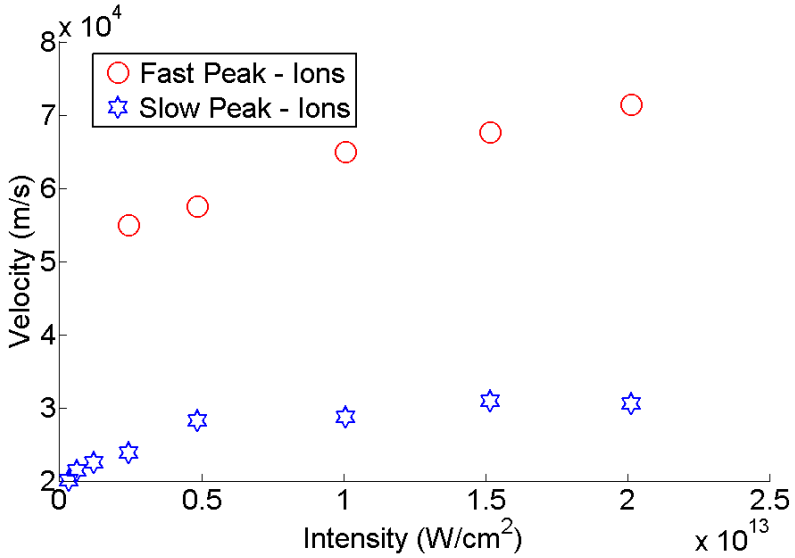

Figure 3.16: Peak velocity for fast and slow components of ion signal

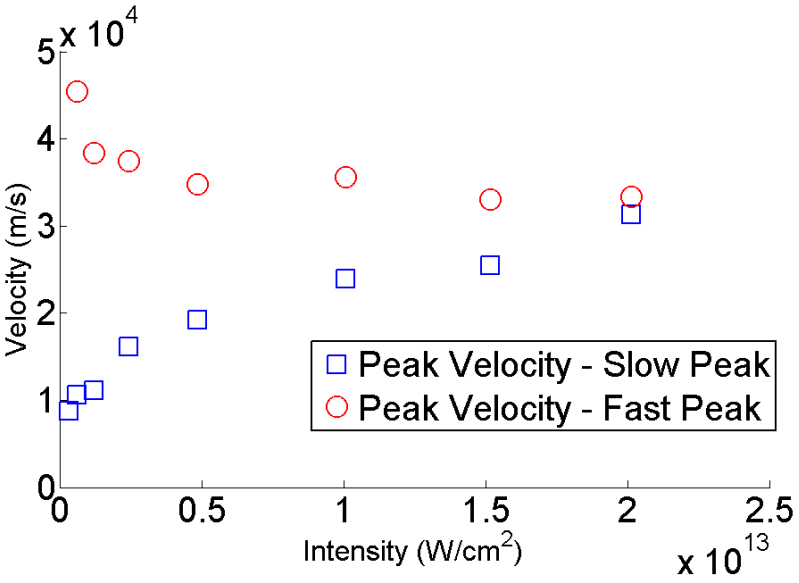

Figure 3.17: Peak velocity for fast and slow components of electron signal

escaping electrons and accelerated ions as two plates of a parallel capacitor. If the area of these plates is assumed to be the spot size of the laser, the electric field can be

written as $eN_e/\epsilon A$, where N_e is the number of electrons. At the highest laser energy (1 mJ), the number of particles, N_e is found by integrating under the fast peak and dividing by the electron charge and then normalising for the angular acceptance of the detector. The crude assumption is made that the angular acceptance is found by finding the angle subtended by an arc equal in length to the probe diameter at a radius equal to the target-probe distance. That is, ϕ = s/r = 0.5 mm / 50 mm = 0.01. From this, a value of $N_e \simeq 2 \times 10^{10}$ is found. The gain in kinetic energy is then found by the work-energy theorem to give $KE_{gain} = Ze^2N_e\lambda_d/\epsilon A$. The Debye length ($\lambda_d(m) = 7.4\sqrt{T_e(eV)/n_e(/cm^3)}$) is found to be 40 nm assuming a density of 10^{16} $/cm^3$ and an electron temperature of 3 eV (these assumptions are validated in later experiments). This leads to a gain in kinetic energy of a singly charged ion of $\sim$ 600 eV. From Figure 3.11, kinetic energies of 700 eV and 120 eV are found which is in general agreement with the capacitance calculation [38].

3.6 Results: Angular emission from Si ablation

3.6.1 Angular dependence of ion emission

The angular distribution of the ion emission was measured using the angular probe described previously. The laser intensity was kept constant at 5×10^{12} W/cm^2 for the whole experiment and all other experimental conditions were the same as in the previous section. In order to increase the visibility of the space charge effects in the probe signals, the probe voltage was set to -100 V. Figure 3.18 shows the time-of-flight distributions for different probe angles with respect to the target normal.

In some cases, the high kinetic energy peak was blended somewhat into the low KE peak and needed to be deconvolved. This was achieved by constructing a mathematical fit to the experimental trace which consisted of a Gaussian term (to describe the high KE peak) and a shifted Maxwell-Boltzmann term (to describe the low KE peak). The ion yield (integrated area) for each peak is plotted in Figure 3.19 and shows similar angular distributions for both peaks. The results show that the ions

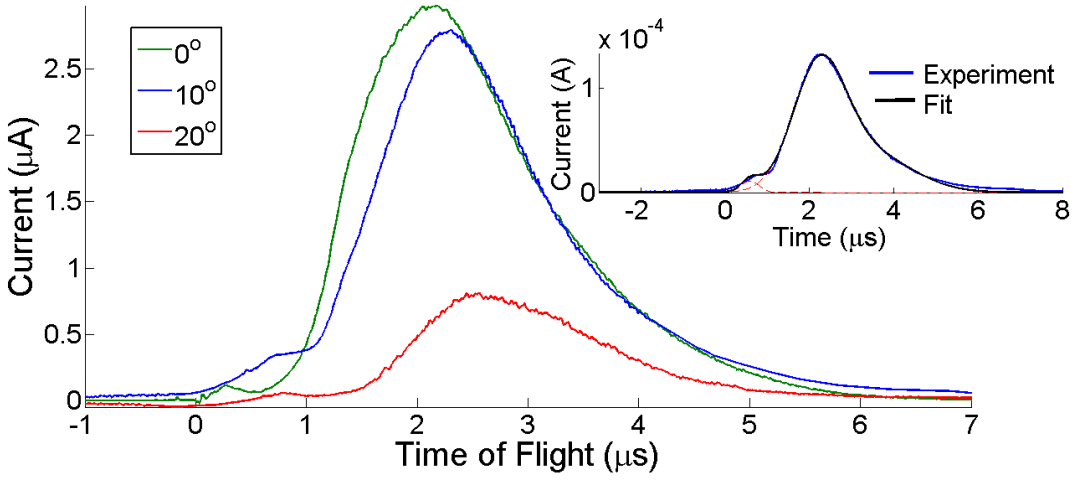

Figure 3.18: Variation in the ion time-of-flight distribution for various detection angles. The intensity in this case was 5×10^{12} Wcm^{-2} with a probe bias of -100 V. Also shown is an example of the deconvolution procedure to calculate the high KE peak areas (inset).

in fs-laser produced plasmas are emitted in a narrow cone about the target normal. The solid lines in Figure 3.19 represent Gaussian or quadratic fits to the experimental data. The ion signals are emitted in a cone of FWHM $\pm 20^o$ which is generally in-line with literature values for angular emission in fs laser plasma experiments [13, 9]. One possible reason for the narrow cone of emission is the fact that electrons are heated to a very high energy before any heat conduction to the lattice can occur. This creates a steep pressure gradient normal to the target resulting in a preferred emission in that direction. Similarly, some ions are removed and accelerated due to electrostatic forces from the high energy electrons which will also be favoured along the normal direction where the dot product of the electrostatic force and the area vector of the target is high. The estimated emission angle of the higher KE peak is found to be the same as the low KE peak indicating that the expansion dynamics of both ion species are similar. The data supports the hypothesis that the emission for both the thermal and non thermal ion species is driven by pressure gradients created by the laser-target interaction. From Figure 3.18, it can be seen that the maximum

probable velocity of both ion species falls as the probe is moved from the normal, again these results agree with similar studies presented in the literature.

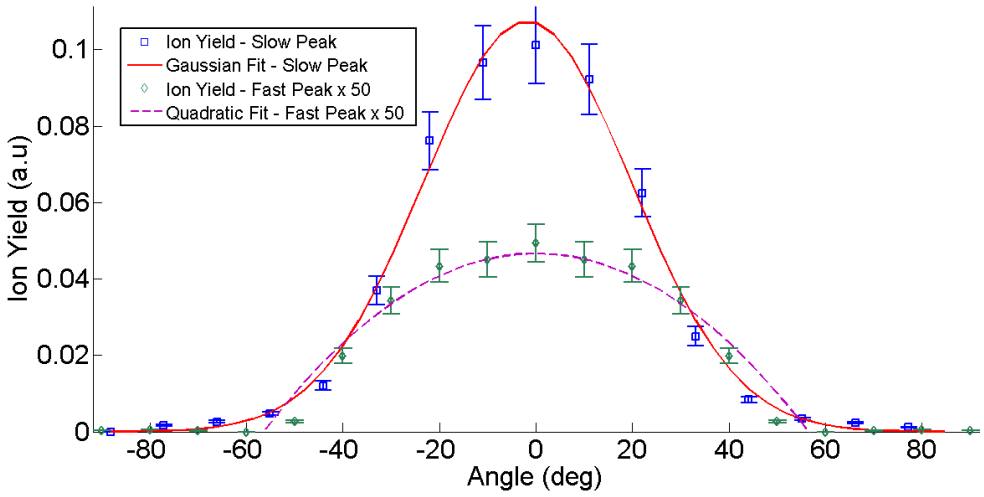

Figure 3.19: Angular distribution for both components of the ion signal. The intensity in this case was 5×10^{12} Wcm^{-2} with a probe bias of -100 V.

3.6.2 Electron angular emission

The time of flight profiles for the electrons is presented in Figure 3.20. Again, a bi-modal structure is seen, and both peaks decrease as the probe is moved from off-normal. For this experiment, the probe voltage was increased to +100 V in order to increase the visibility of the space charge effects and to better resolve the two peaks. The angular distribution of each peak is plotted in Figure 3.21. The angular distributions of the electron yields are not equal. This is in contrast to the ion yields, indicating that the expansion dynamics for each electron component may be driven by different mechanisms. For both electron components, the electron distribution is wider in emission angle that the respective ion case. However, the low KE component of the electron signal is emitted over a much broader angle than the high KE case. The slow peak angular distribution is quite similar to literature values for long pulse laser experiments indicating that the expansion of the low KE electron component is

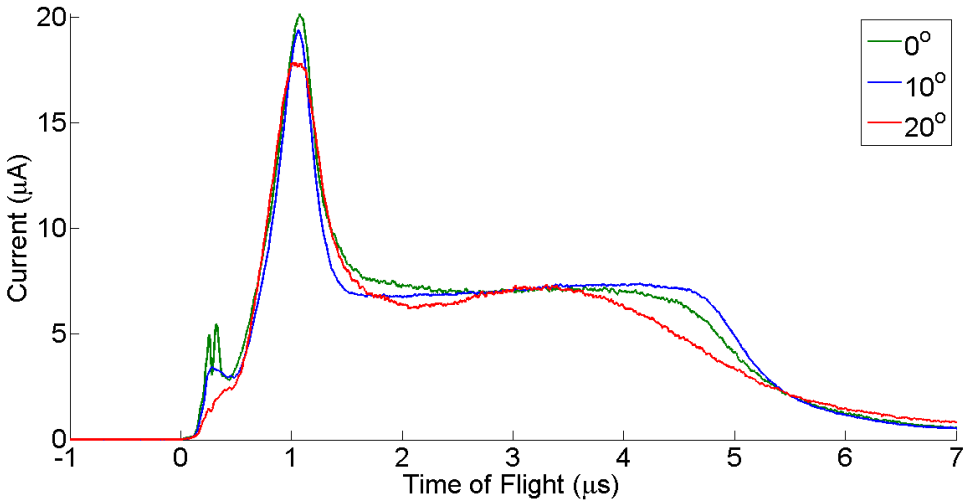

Figure 3.20: Variation in the electron time of flight distribution for various detection angles.

hydrodynamic in nature and so the electrons are emitted isotropically. The narrow, high KE electron signal can be explained by a similar argument made for the ions above. That is, electrons are heated to in excess of the Fermi energy and escape from the target but only within the laser interaction region, explaining the preferred emission along the target normal.

Viewed together, the electron and ion angular distributions paint a picture of plasma expansion that goes as follows. A population of electrons is heated by the laser within the interaction region and expands from the target perferentially in the direction of the normal. These electrons pull a population of ions and accelerate them to a high kinetic energy and thus this population of ions has a similar, but narrower distribution. The remaining electrons then expand isotropically from the target much like a hydrodynamic fluid. This sets up a pressure gradient in the direction normal to the target and ions then expand along the pressure gradient lines producing a second ion distribution which is again emitted heavily in the normal direction. Both a wide and a narrow distribution of electrons was noted for a range of laser intensities and probe voltages. This eliminates the possibility that the two angular distributions

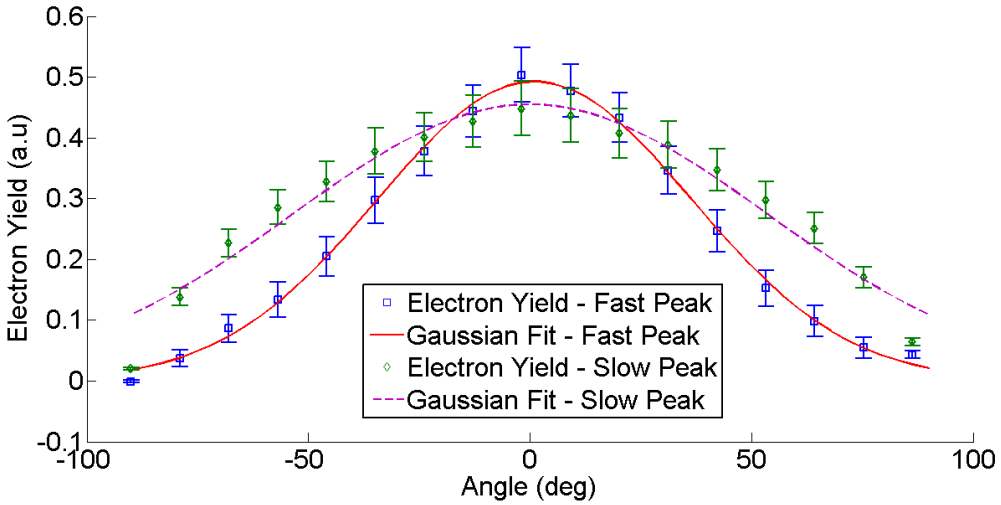

Figure 3.21: Angular distribution for both components of the electron signal.

were somehow caused by distortions due to the high probe voltage.

3.7 Results: Polarization dependence

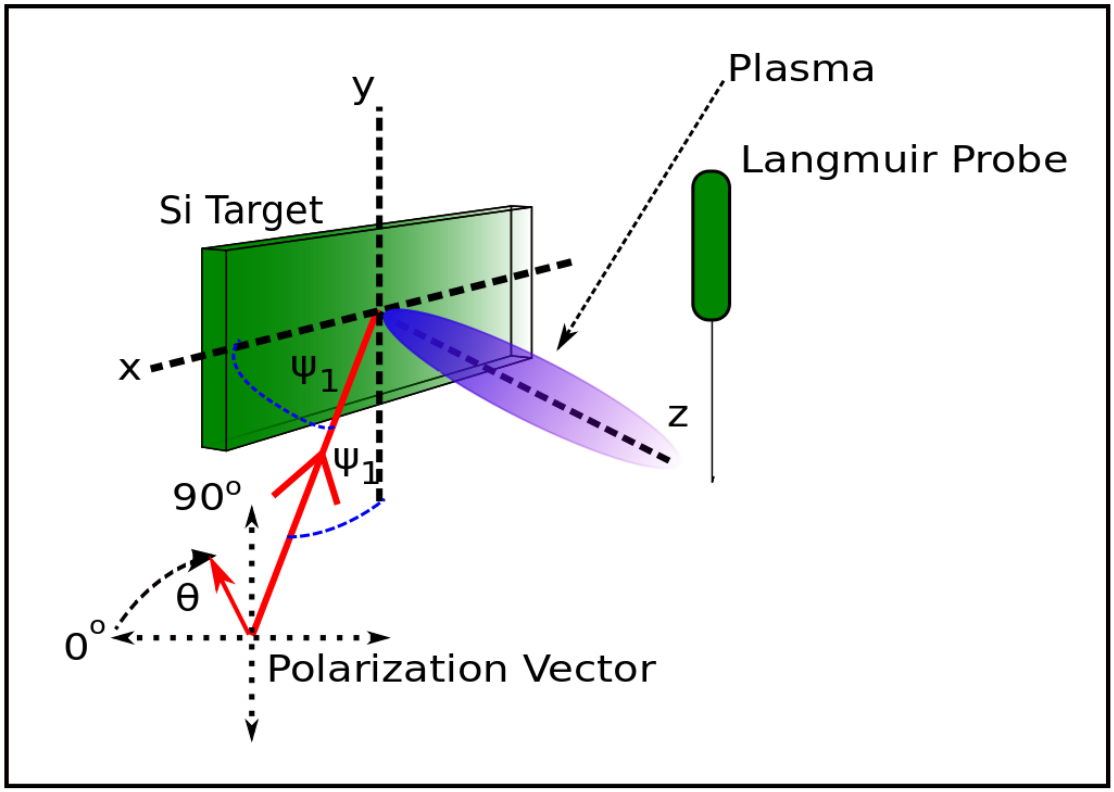

Figure 3.22: Schematic of the polarisation experiment.

Collisional effects, density gradient lengths, energy transport and absorption processes in laser produced plasmas have all been found to vary with the polarisation state of the laser beam [41, 42, 43]. With this in mind, a number of experiments were performed. Both the ion and electron yields from a silicon-target were measured as a function of polarisation state of the laser beam. The experiments were performed at two different laser power densities (5×10^{12} Wcm^{-2} and 2×10^{13} Wcm^{-2}) and two different wavelengths (800 nm and 400 nm). The results were then interpreted in the context of existing physical models [44, 45]. Figure 3.22 shows the experimental configuration for the polarisation experiment. The laser polarisation was rotated using a half wave plate. The target-probe distance was fixed at 5 cm using the angular

probe (orthogonal to plasma flow) and the probe was biased so that it only collected the species under study (ions or electrons).

3.7.1 Ion emission

Figure 3.23 shows the ion signal as a function of laser polarisation. There is a drop in ion yield and most probable kinetic energy as the laser polarisation is rotated from P to S polarisation. Previous studies on the ion emission from ultrafast laser ablated matter have shown the same results [7].

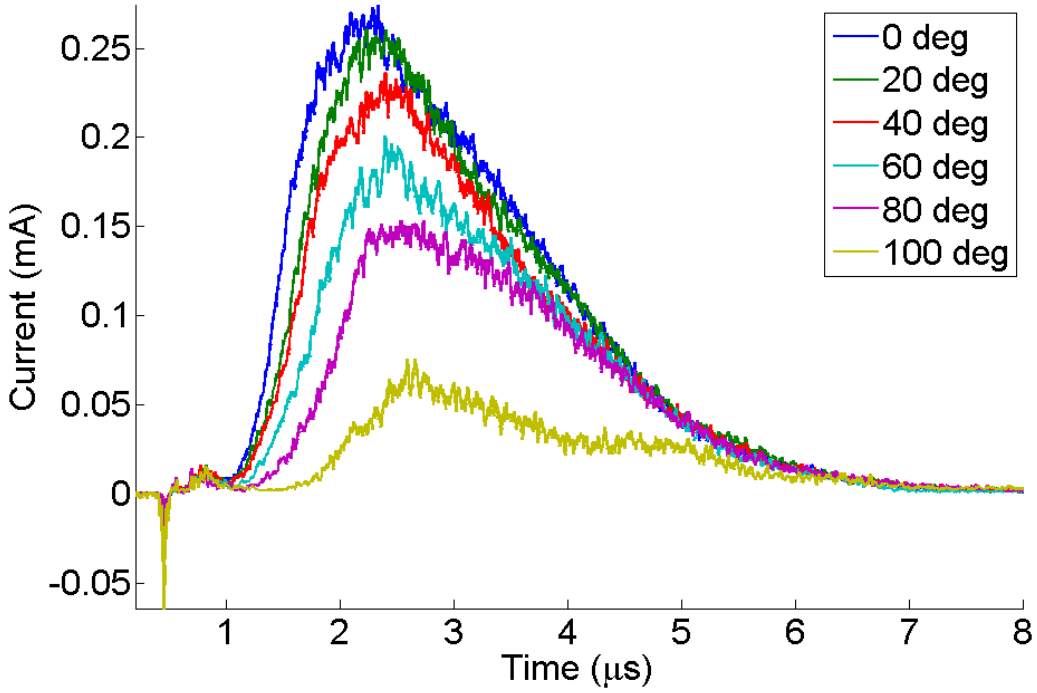

Figure 3.23: Time-of-flight ion distributions for different polarisations.

Again the time of flight distributions show that both the peak yield and the peak velocity are highly dependant on laser polarization. It can be seen that ion emission is much more efficient for P polarization than for S polarization.

The ion yields for the slow peak and the fast peak are plotted as a function of

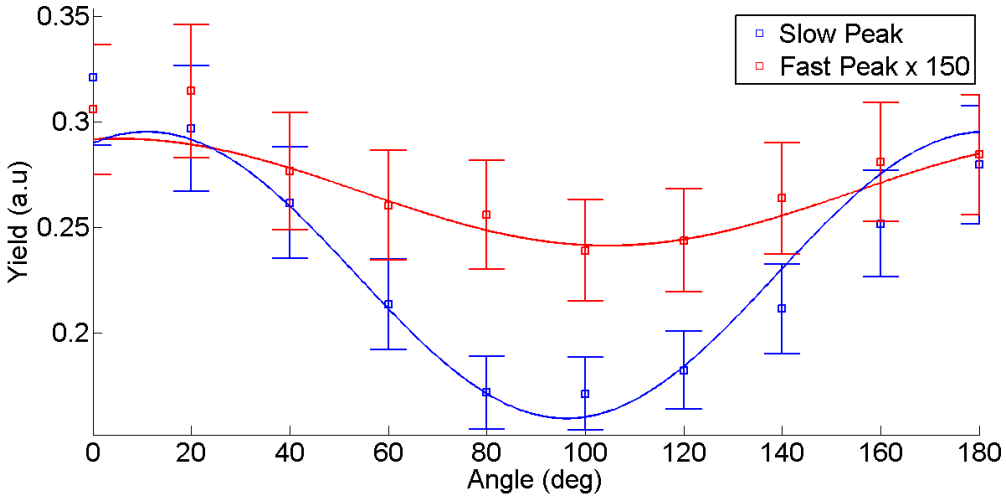

Figure 3.24: Ion yield (Slow and Fast Peak) for different polarisations.

polarisation angle (Figure 3.24). Figures 3.24 and 3.25 show both the yield and the peak ion velocity has a cosine dependence on polarization angle. The solid lines in Figures 3.24 and 3.25 represent fits to the data of the form $f(t) = a_0 + a_1 cos(\omega t)$. For the slow peak the ratio $A_P/A_S \approx 2$ and for the fast peak $A_P/A_S \approx 1.2$ indicates that the fast peak is less dependent on laser polarization than the slow peak. It is somewhat intuititive to think of P polarization being more efficient in generating ions because in P polarization the electric field of the laser penetrates deeper into the target. In previous work, the higher ion yield at P polarization has been attributed to greater resonance absorption and collisional effects taking place than at S polarization [46, 47]. Studies of this kind at different intensities and different laser wavelengths have yielded similar trends and the results are summarised in Table 3.1: If the laser pulse is much shorter than the typical coupling time of the solid, it stands to reason that at most a minimal amount of the laser light interacts with the expanding plasma plume. Therefore, the reflectivity and absorption of the laser beam should be governed strictly by the solutions to Maxwell's equations [48]. However, the ablation will cause an initial increase in the free electron density. This plasma can then absorb further laser light by collisional or resonant means. Reso-

Parameters		*S*		*P*	
		Fast Peak	*Slow Peak*	*Fast Peak*	*Slow Peak*
800 nm	5×10^{12} Wcm^{-2}	0.0010	.17	.0013	.32
	2×10^{13} Wcm^{-2}	0.43	2.3	0.6	2.5
400 nm	5×10^{12} Wcm^{-2}	.0015	.04	.0017	.05

Table 3.1: Summary of the ion yields (arb. units) for different parameters

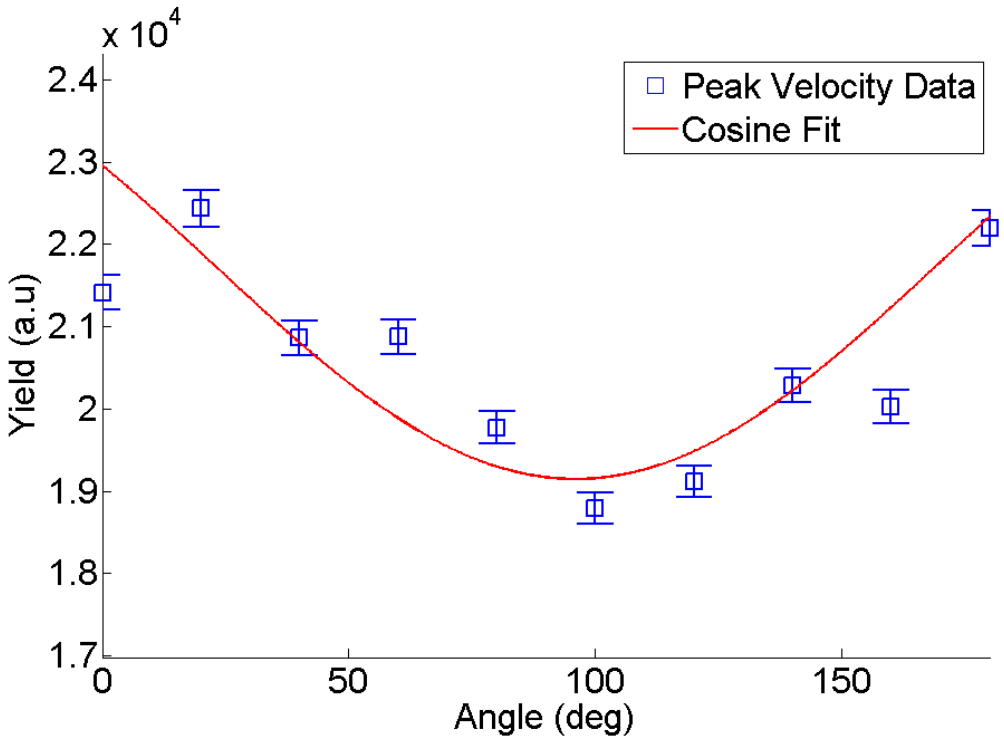

Figure 3.25: Peak ion velocity for different polarisations.

nant absorption occurs when the laser causes oscillations of the electrons along the direction of the density gradient (i.e normal to the target). For this reason, it generally only occurs for P polarised light whereas collisional absorption can occur for both polarisation states (S and P). This is why, in general, P polarised light tends to produce more ions in the ablation process.

Collisional absorption tends to be polarisation independent and so the difference

in the ion yields between P and S polarisation, normalised to the P ion yield will allow for a determination of the resonance absorption contribution. If the ion yield at P polarisation is R_P and the ion yield at S polarisation is R_S, the resonance absorption is given by:

$$\alpha = \frac{R_P - R_S}{R_P} \tag{3.38}$$

The value of α for the different experimental conditions is given in Table 3.2

		α_{fast}	α_{slow}
800 nm	2×10^{13} Wcm^{-2}	0.12	0.08
	5×10^{12} Wcm^{-2}	0.23	0.46
400nm	5×10^{12} Wcm^{-2}	0.12	0.23

Table 3.2: Table showing the resonance absorption factor for different experimental conditions. The pulse width was 66 fs for all measurements

It is seen from Table 3.2 that for both the fast and slow peaks, resonant absorption is greater for the 800 nm, 5×10^{12} Wcm^{-2}. Resonant absorption requires the laser field to penetrate through to an area of high electron density and, once penetration has occured, the plume will gain energy from the laser field through collisional damping mechanisms. The data appears to show little resonant absorption for the slow peak in the high intensity 800 nm case. It is unclear why the high intensity case shows no resonance absorption, however one explanation could be that the strong electric field in the high intensity case makes it difficult for the laser to penetrate through into a high density region, reducing the probability of resonance absorption [49].

3.7.2 Electron emission

The electron signals show an interesting behaviour with regard to varying the polarisation.

The familiar double peaked structure is present in the TOF electron distributions

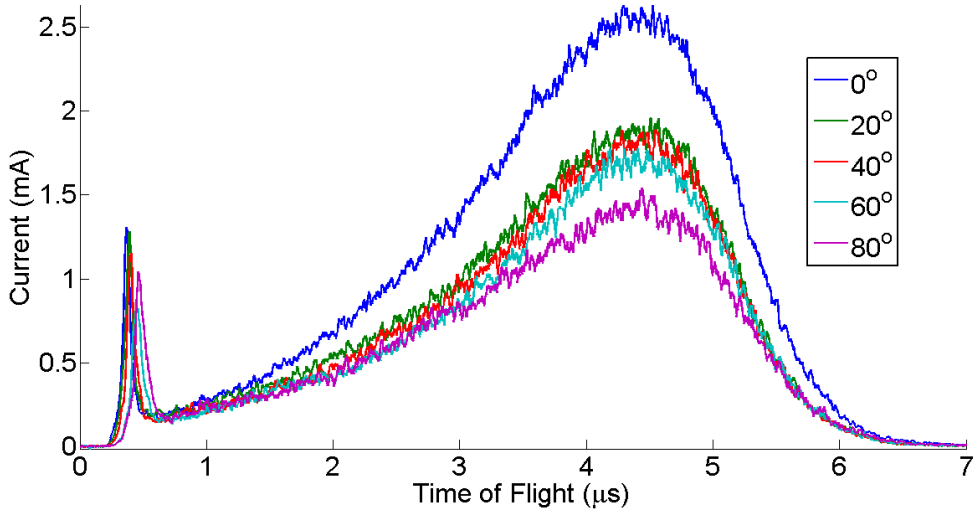

Figure 3.26: Time-of-flight distributions for electron emission

with varying polarisation. However, looking at the electron yield as a function of polarisation (Figure 3.27), an almost "resonant" type feature is visible at a laser polarisation angle of 90^o. In general, the electron distribution signal showed a far smaller signal to noise ratio and far more jitter ($\sim 10\%$ in terms of the peak KE of each peak) than was present in measuring the ion signals. This could be due to the mass difference between ions and electrons meaning that the electron signal is sensitive to instantaneous changes in the probe voltage or other jittering experimental conditions With that in mind, Figure 3.26 represents a typical TOF distribution as a function of polarisation whereas in order to extract the yields, the experiment was run 3 times and the yield of each experimental run was averaged at each polarisation to produce Figure 3.27.

The curious nature of Figure 3.27 is counter-intuitive when considering that, up to now the ion and electron signals have showed (generally) the same behaviour with changing laser / probe parameters. The following tests were performed in order to ensure the validity of the signal.

- The data were collected on both the angular probe (orthogonal to plasma flow)

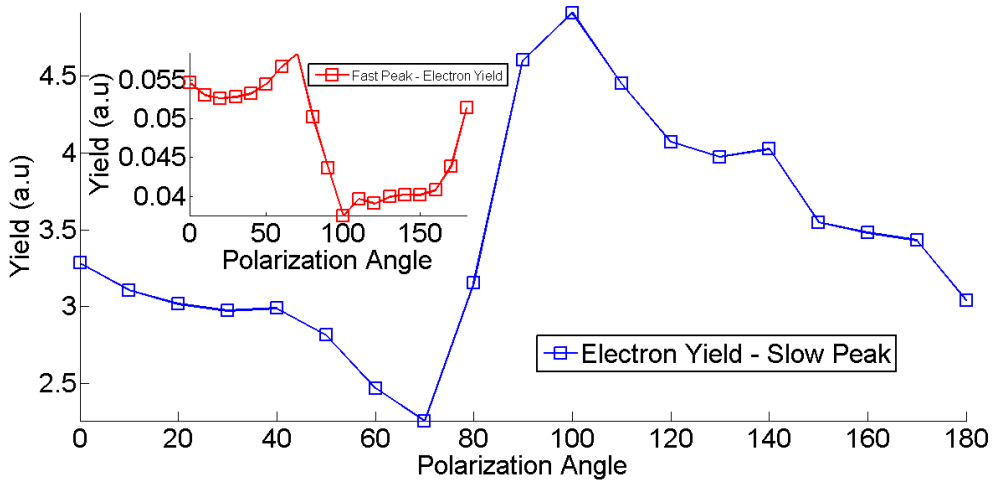

Figure 3.27: Electron yield for different polarisations. (Main: Slow Peak, Inset:Fast Peak).

and the expansion probe (parallel to plasma flow) and showed the same shape in the electron yield as a function of polarisation.

- The data were collected in a linear fashion (that is, the half wave plate was moved from 0^o to 90^o in steps of 5^o and in order of ascending half wave plate angle). The experiment was subsequently repeated in a random fashion (where the data were collected by changing the half wave plate in no particular numerical order). Both data collection methods yielded the same result.

- The data were collected at a variety of probe voltages and the polarisation dependence of the electron yield was found to be independent of the probe voltage above a moderate positive bias (say $\sim$20 V).

Much like the ion data, the polarisation dependence of the electrons was affected by laser intensity and wavelength and this is discussed later on. A study of the polarisation dependence of the electron/ ion signal using a Langmuir probe could not be found in the literature, however various studies have studied the difference in ion emission between S and P polarisation states and have attributed the behaviour

to either resonance effects or particle transport effects [45, 50]. In other studies, the reflection properties of laser produced plasma's are investigated at both S and P polarisation in order to infer information about resonant absorption and collisions. Here, a suggestion is made as to the nature of the electron signal presented in Figure 3.27.

Polarisation dependence of thermal transport.

The most probable velocity of each peak is plotted in Figure 3.28.

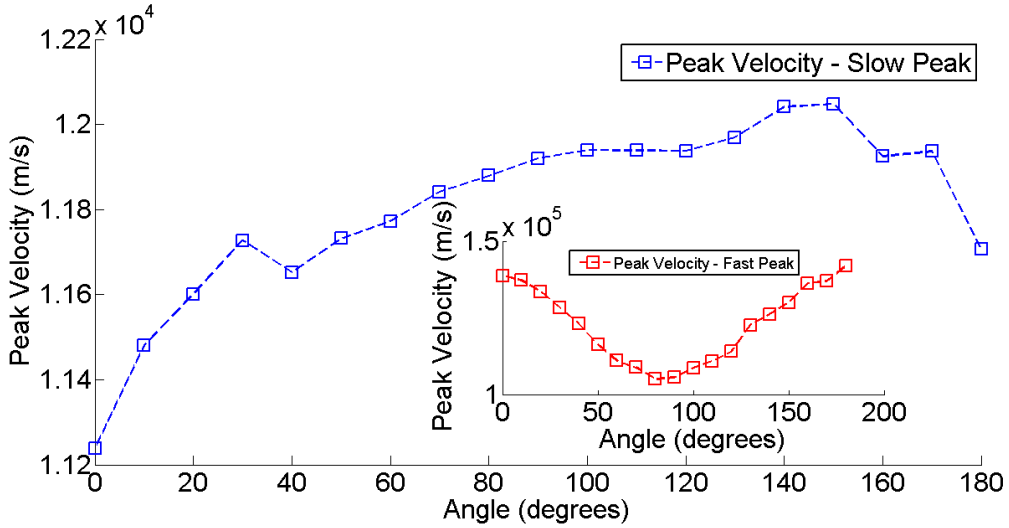

Figure 3.28: Peak electron velocity for various polarisation states. (Main: Slow Peak, Inset: Fast Peak).

The inset of Figure 3.28 shows that the peak velocity of the fast component has a largely similar polarisation dependence to the fast ion component in Figure 3.25. In fact, the ratio $V_{T,i}/V_{T,e}$ is the same for S and P polarisation states (2.21 for P and 2.20 for S). However, the velocity of the slow electron component has a different polarisation dependence than its ionic counterpart. There is a change in the ratio of ion-electron peak velocity from 1.9 to 2.3. It is hypothesised then that for P polarised light there is somehow a reduction in conductivity of the slow electron component. One possible mechanism that can account for this behaviour is the excitation of

electrostatic fields due to resonant absorption. These fields create a potential barrier that reduces the conductivity of slow electron component. In this hypothesis, the fast peak is assumed to be able to easily surmount these potential barriers (as indicated by the invariance of the ratios as a function of polarisation) [45, 49].

In P polarised light at oblique incidence, the laser electric field will have a component along the plasma flow direction and thus will oscillate electrons along the density gradient of the plasma plume. As the field penetrates the plasma, it will cause an oscillation of electrons between areas of varying charge density. This creates a charge density fluctuation in the plume which transfers energy from the incident light field to the plasma in a process known as 'resonant absorption'. The associated potential barrier that is created as a result of this absorption can be given as [45]:

$$e\phi = \frac{1}{2}\left\langle V_\omega^2 \right\rangle \tag{3.39}$$

where $\langle V_\omega^2 \rangle$ is the cycle average velocity of the electron in the laser field. This velocity is found from the ponderomotive force.

$$\left\langle V_\omega^2 \right\rangle = e^2 \left\langle E_\omega^2 \right\rangle / m^2 \omega_{pe}^2 \tag{3.40}$$

Where m is the electron mass, ω_{pe} is the plasma frequency and E_ω^2 is the square of the field inside the plasma plume. Numerical solutions, found in the literature, to the wave equation for the case of a plasma indicate that within the plume, the peak value of the electric field can grow to up to 3 times the incident electric field value [49]. With this in mind, a value of $V_\omega \simeq$ several V_T is readily obtained where V_T is the electron thermal velocity of the slow peak. It is assumed that the fast component of the electron signal is energetic enough to surmount these potential barriers This is assuming $E_\omega = 10^8$ V/m and a plasma frequency equal to the optical laser frequency $\omega_{pe} = 2.3 \times 10^{15}$ rad/s [49].

3.8 Results: Temperature and density analysis using Langmuir probe

In order to characterise the laser produced plasma in terms of density and temperature, the time-of-flight distribution was measured as a function of probe bias. An I-V curve was then generated by picking a specific point in time and plotting the current versus probe voltage. From this I-V curve, the electron temperature and density was calculated from either orbital motion theory (density) or Langmuir theory (temperature). The probe bias was varied from +100 V to -100 V in steps of 2-5 V. Each time of flight trace represents the average of 16 laser shots. An initial 10 or so cleaning shots were fired before each trace was saved. Figure 3.29 shows the time of flight distributions for different probe biases for a laser intensity of 5×10^{12} Wcm^{-2} and a wavelength of 800 nm. The probe - target distance for all experiments in this section was 50 mm using the angular probe (oriented orthogonal to plasma flow).

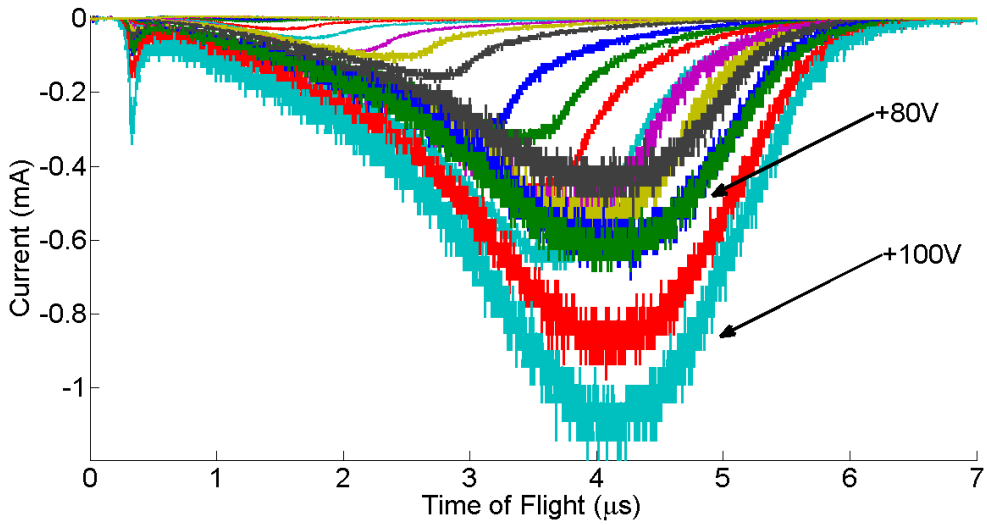

Figure 3.29: The induced current from the plasma as a function of probe bias.

At early times (t<1 μs) two distinct linear regions are found in the $\ln|I - I_s|$ vs V_b

plot indicating the presence of two separate electron populations simultaneously: a "hot" population and a "cold" population. Quite quickly however both components thermalise and become generally indistinguishable. Figure 3.30 shows the electron temperature as a function of time as calculated by Langmuir theory. The presence of two electron populations simultaneously is evidence of a double layer formation in the plasma [33, 51]. In the context of laser plasmas quasi-neutrality means that,

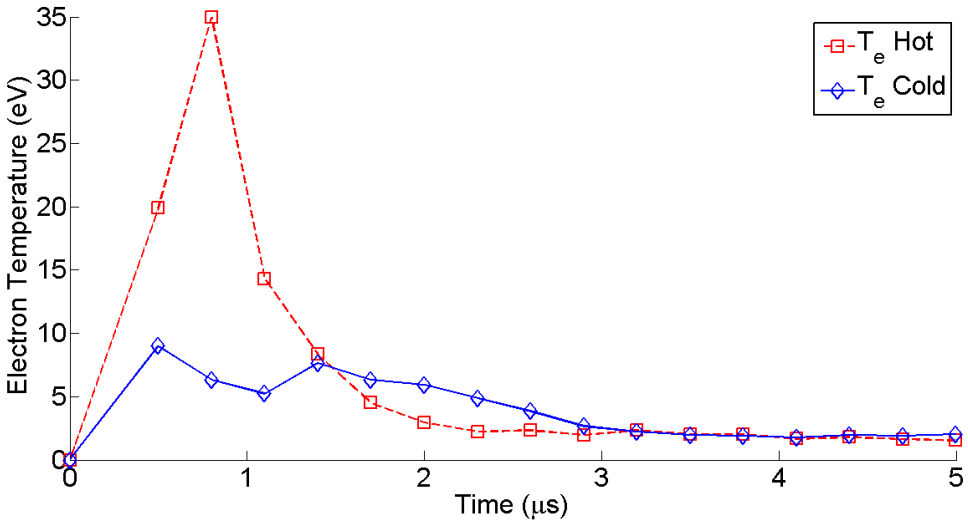

Figure 3.30: Time resolved temperature of Si plasma from Langmuir theory.

while the net charge of the plasma may be zero, the plasma may have a charge when looked at on small length scales on the order of the Debye length. If quasi neutrality is violated over large length scales, a double layer is formed [52]. This double layer is characterised by a number of properties. Firstly, a double layer will cause a discontinuity in the plasma potential and the associated potential drop should be roughly on the order of the plasma temperature [53]. The potential drop across the double layer generates a strong self consistent electric field which will have the effect of accelerating ions and retarding electrons. Thus, multiple electron and ion components are standard features of double layers in plasmas. The earliest descriptions of these double layers date back to Langmuir and a detailed experimental and theoretical treatment is given by Hora specifically in the context of laser produced

plasma [26]. The hypothesis of double layer formation is that it is insufficient to treat the plasma as a single fluid expanding into the vacuum [51]. Thus, a two fluid or multi-fluid model is suggested (comprised of a hot and cold population of electrons) and this model is outlined in some detail in various papers and reports [50, 54]. Outcomes of this model suggest the following: 1) The potential drop across the double layer is equal to the temperature of the plasma and 2) the ratio of temperatures of the two electron populations (T_{hot}/T_{cold}) is an indication of a rarefaction shockwave in the double layer. Specifically, if the plasma is treated as a combination of multiple fluids, rarefaction occurs for a value $T_{hot}/T_{cold} = 5.4$ [50]. Figure 3.31 shows the ratio of both electron temperatures as a function of time, indicating that a rarefaction occurs for $t \approx 500$ ns. This result indicates that the plasma is indeed made up of multiple electron fluids and may go some way to explaining the multi-peaked structure seen at early times in (for example) Figure 3.11

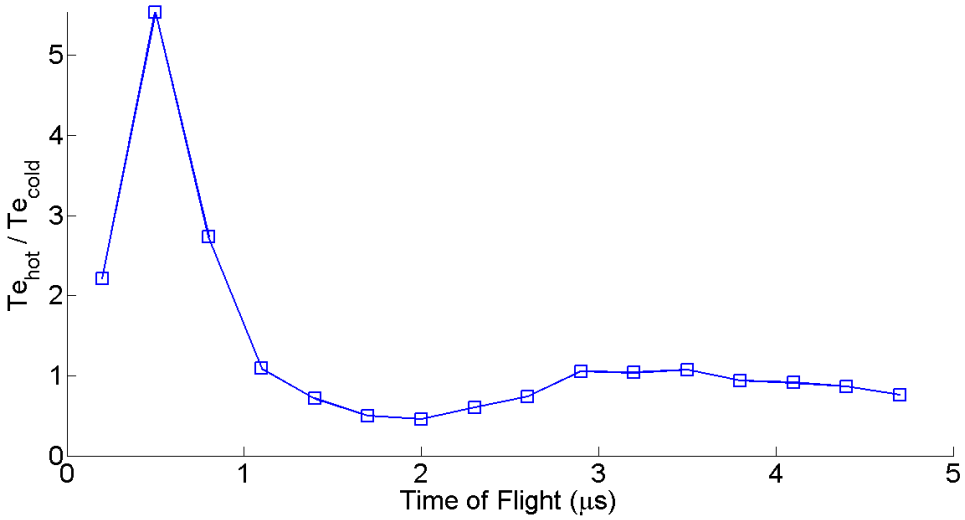

Figure 3.31: Ratio of temperatures revealing possible indication of the presence of a rarefication shockwave within the plasma.

A rarefaction shockwave has been presented in the literature before with long pulse laser plasma experiments [33] and the existance of rarefaction shockwaves in ultrafast laser experiments has been said to be responsible for the formation of a

Newton's rings type pattern on the surface of the laser target [53]. A re-analysis of Figure 3.10 shows the presence of a structure that could be a Newton's rings pattern, however because the experiment was done in averaging mode and not single-shot, it is unlikely that this structure is due to the rarefaction shockwave.

The electron density has been computed using orbital motion theory and again, two distinct linear regions were noticeable in the I^2 vs V_b plot. This measurement is used to determine the self generated electric field within the plasma. Knowing the temperature and the density, the Debye length can be determined from the equation $\lambda_D = \sqrt{\epsilon_o k_B T_e / n_e e^2}$ [24].

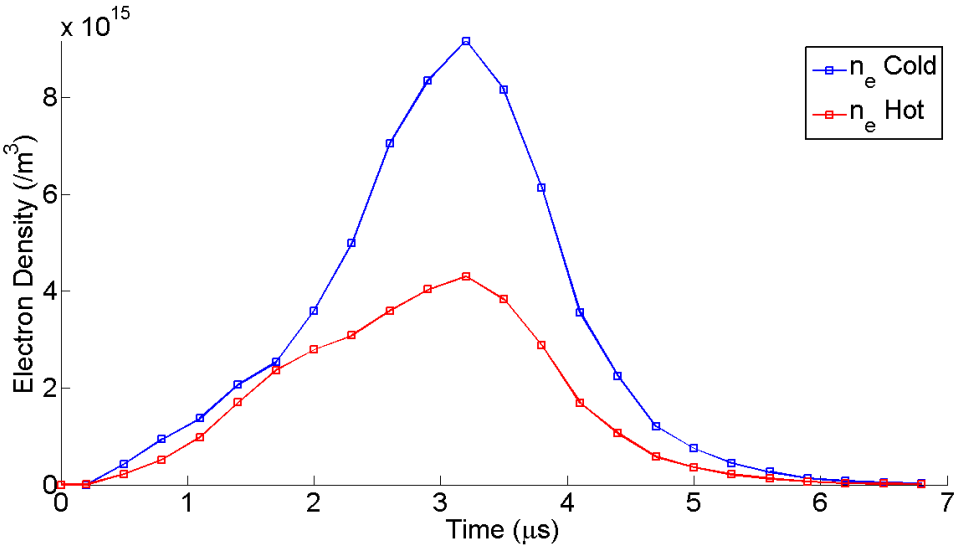

Figure 3.32: Time resolved density of Si plasma from orbital motion theory.

As shown in Figure 3.4, the plasma potential can be found by calculating the point of intersection between the line fitted to the linear portion of the $ln|I - I_{is}|$ vs $(V - V_f)$ curve and the line fitted to the electron saturation region of the same curve. It should be noted however, because of the transient nature of a laser produced plasma, that the value obtained from this calculation does not reveal the plasma potential as traditionally defined but rather a value of the potential associated with the self generated, ambi-polar electric field in the plasma plume that forms due to electron and ion separation. Figure 3.33 shows the calculated plasma potentials for

both the hot and cold electron distributions in the silicon plasma.

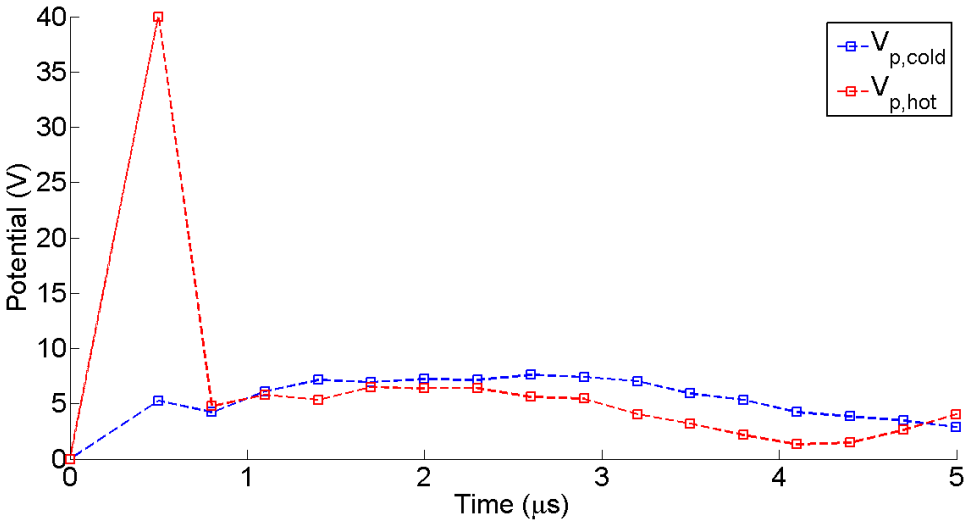

Figure 3.33: Plasma potential as a function of time for $\lambda_{LASER} = 800$ nm, $I = 5{\times}10^{12}$ Wcm^{-2} and probe distance 50 mm

The large potential drop (which is roughly equal to the electron temperature) at early times in the hot electron population is indicative of double layer formation [55]. The electric field generated in the plume is then evaluated by dividing the plasma potential by the Debye length. Figures 3.34 and 3.35 show the Debye length (which is on the order of 10^{-6}m throughout) and the plasma electric field. At $t \approx 1\mu s$ the hot electrons appear to have a large ambi-polar field that is not present in the cold electrons. This is an indication that the hot electrons are subjected to large, (presumably) retarding forces during the early phase of the plasma evolution which explains the equalisation of temperatures and densities at later times. Combining the results of this study with the fluence dependence earlier, it is then perhaps appropriate to consider that the plasma consists of two distinct particle populations - a thermal component (slow) and a suprathermal component (fast). However, these results indicate that the two populations do not in fact exist simultaneously and that the suprathermal component is exhausted of particles relatively quickly. It is presumably the case (and this is studied in the next section) that the suprathermal

particles are subjected to strong forces which cause them to diffuse into the core of the plasma plume.

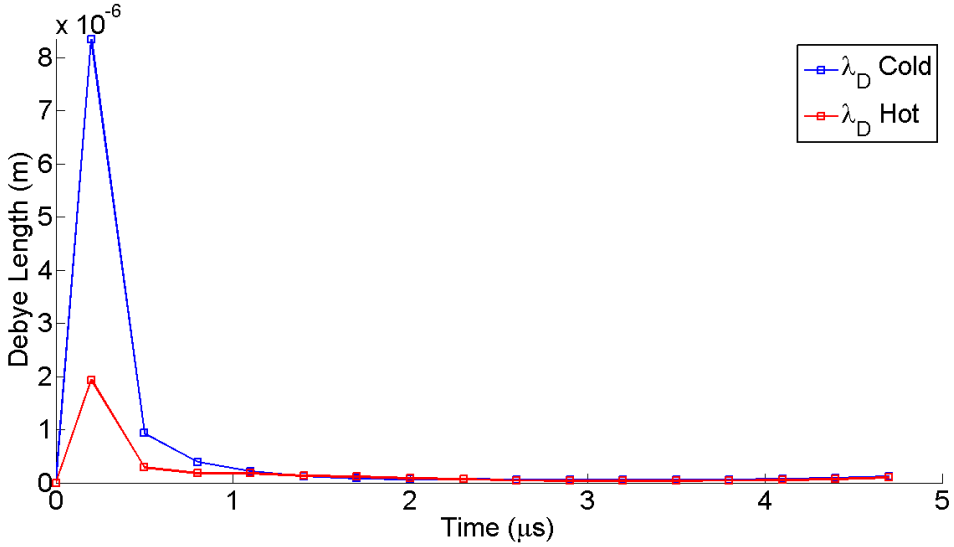

Figure 3.34: Debye length as a function of time for $\lambda_{LASER} = 800$ nm, $I = 5 \times 10^{12}$ Wcm^{-2} and probe distance 50 mm

For comparison, temperature and density measurements were made on a laser produced plasma created using 400 nm laser light with similar pulse widths and intensities (32 fs and 5×10^{12} Wcm^{-2} respectively). The time of flight distributions (shown in Figure 3.36 show a quite similar trend to the 800 nm case with the exception that the fast peak seen around 1 μs is perhaps not as well defined.

Figure 3.37 shows the results of the temperature analysis using Langmuir theory, which indicates the presence of a hot and cold electron population. This suggests the presence of a double layer in the 400 nm plasma but perhaps the double layer is not as well defined as it is in the 800nm case. It is noted that the optical penetration depth is ≈ 2 times smaller at 400 nm than at 800 nm resulting in the situation where roughly the same energy is distributed to a smaller number of particles causing a higher initial plume temperature and thus higher ionization degrees. The higher ionization degree results in a higher number of electrons (the density from OML theory is shown in Figure 3.38). This has the effect of increasing the thermal and electrical conductivity

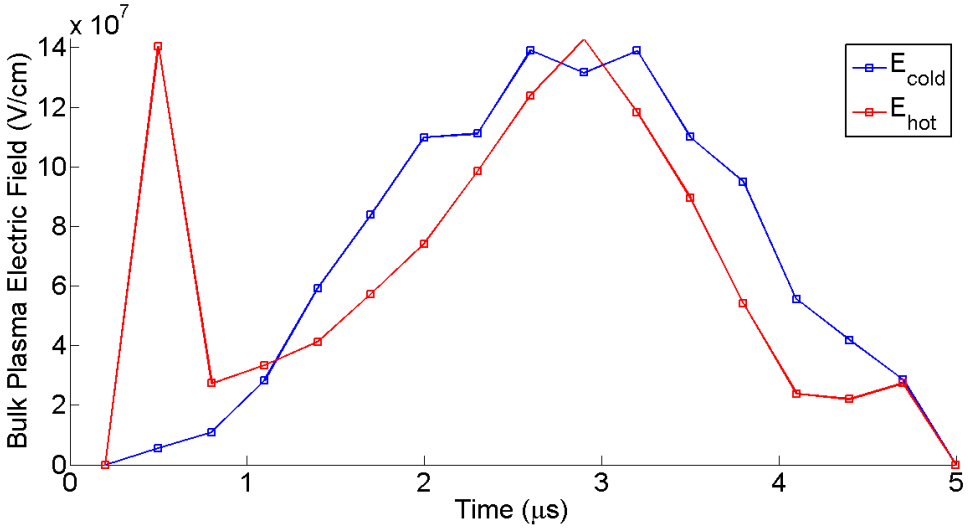

Figure 3.35: Electric rield as a function of time for $\lambda_{LASER} = 800$ nm, $I = 5 \times 10^{12}$ Wcm^{-2} and probe distance 50 mm

between the two electron populations resulting in a thermalisation / equalisation by the time the plasma reaches the probe 50 mm away.

Another possible explanation of the higher density is to consider the fact that for a constant optical geometry, the 400 nm laser light will focus to a beam waist that is smaller than the 800 nm case by a factor equal to the ratio of the wavelengths (≈ 2). Thus the initial size of the plume is a factor of 4 smaller than the 800 nm plume, thus increasing its density. From the data it seems that the formation of the double layer is influenced by the experimental parameters such as optical penetration depth and initial plasma size. It is also concluded that a well formed double layer is characterised by a defined'fast' electron peak. It may be the case however, that the double layer in the case of 400 nm laser light evolves differently than the 800 nm case and that probing the plasma 50 mm away from the target results in measuring a point by which the double layer has either yet to form, or has degenerated. Other factors that can contribute to the amount of 'hot electrons present in the plasma that have yet to be considered include recombination processes such as three body recombination or inverse bremsstrahlung absorption.

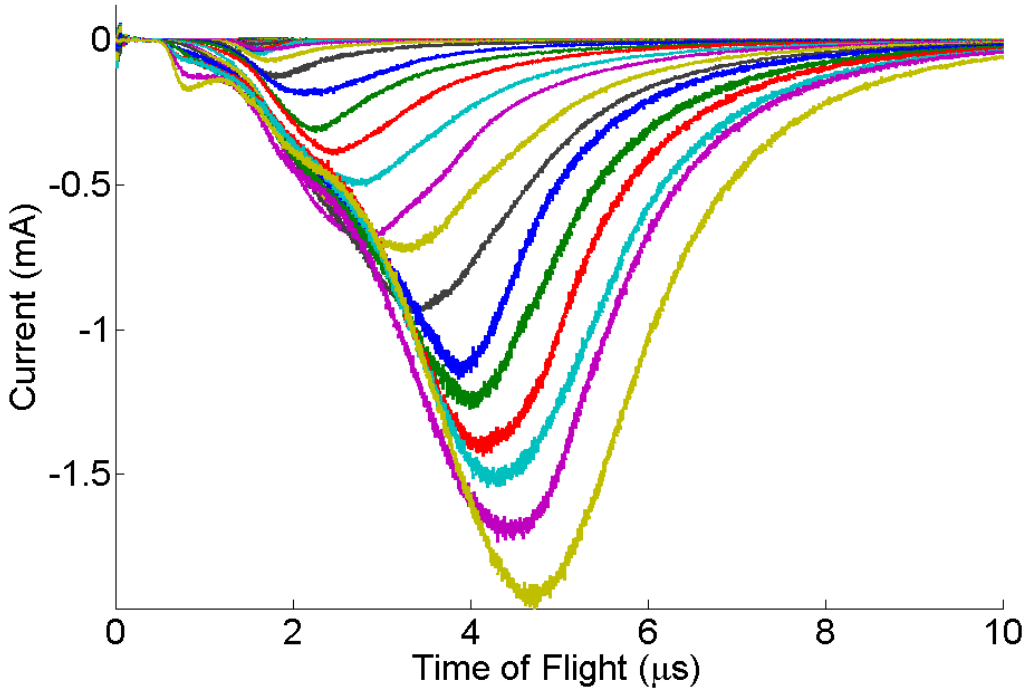

Figure 3.36: Time-of-flight for different bias voltages with second harmonic laser light

In an attempt to further investiage the evolution of the plume, the temperature and density were calculated for a plasma created with 800 nm light, with an intensity of 2×10^{13} Wcm^{-2}. The time of flight distributions are shown in Figure 3.39. In this case, the fast electron peak is not detectable, however the temperature analysis reveals two electron populations with similar temperatures. (Figure 3.40).

Again, it is hypothesised that the high intensity of the laser results in a high electron density target (see Figure 3.40 (inset)) which in turn causes a high electrical and temperature conductivity throughout the plasma resulting in an equalisation of the electron populations.

With regard to recombination, it is noted that three body recombination is described as a process whereby two electrons interacting with each other in the vicinity of an ion can cause one of those electrons to recombine with that ion, the remaining

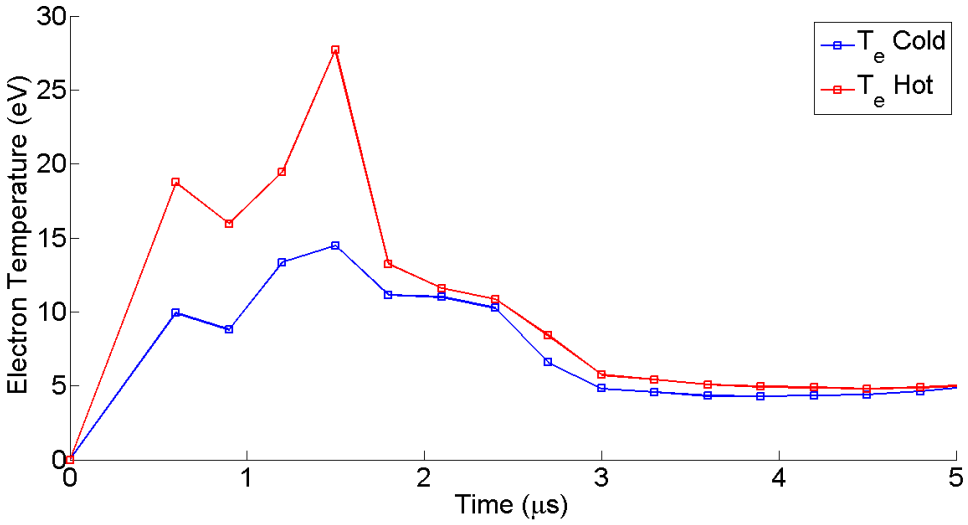

Figure 3.37: Time resolved temperature of Si plasma from Langmuir theory.

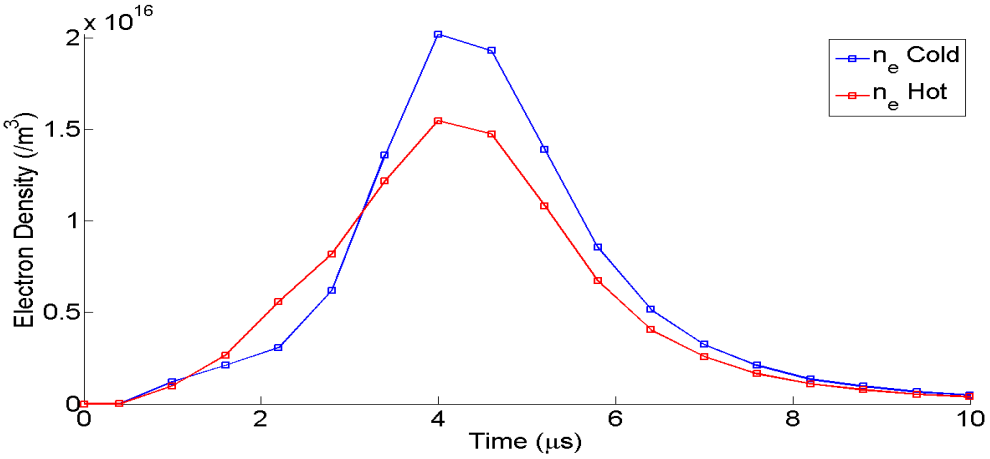

Figure 3.38: Time resolved density of Si plasma from orbital motion theory.

energy is then carried away by the other electron. It is possible for this recombination process to cause electrons to gain temperature and could be a possible explanation of the fast peak observed in the electron signals. However, it is also noted that the rate of three body recombination is given as [56]:

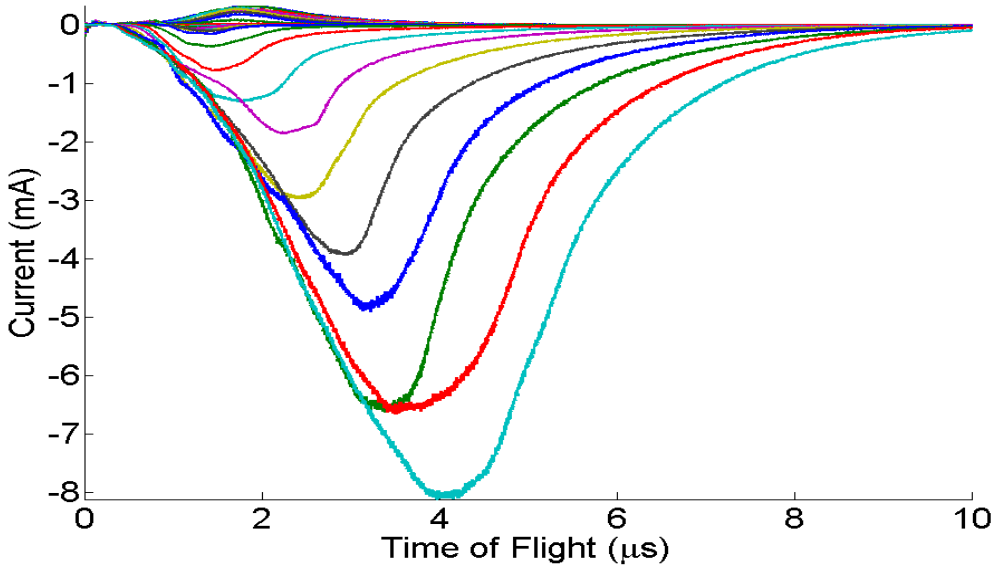

Figure 3.39: Induced plasma current for different bias voltages.

$$R_{3B} = 10^{-26} Z^3 \frac{N_e}{T_e^{9/2}} \tag{3.41}$$

It is then seen that three body recombination should be favoured by a high density, low temperature plasma. The rate of three body recombination should then be highest for the high intensity case reported in Figure 3.40. It seems more likely then that the fast electron peak is produced by rapid heating of electrons to above the Fermi temperature where they escape quickly from the target as predicted by the theories of Gamalay [22] and the experimental evidence of Amoruso [38].

In Figure 3.41, the three measurements are compared side by side when the probe is at 0 V (to follow the change in the floating potential of the probe and hence to infer the structure of the plume). In Figure 3.42 the three measurements are compared side by side when the probe is at a bias of -60 V (to obtain the temporal profile in the ion saturation region) and in Figure 3.43, the tof signals are compared when the probe is at a bias of +60 V such that the electron signal is collected.

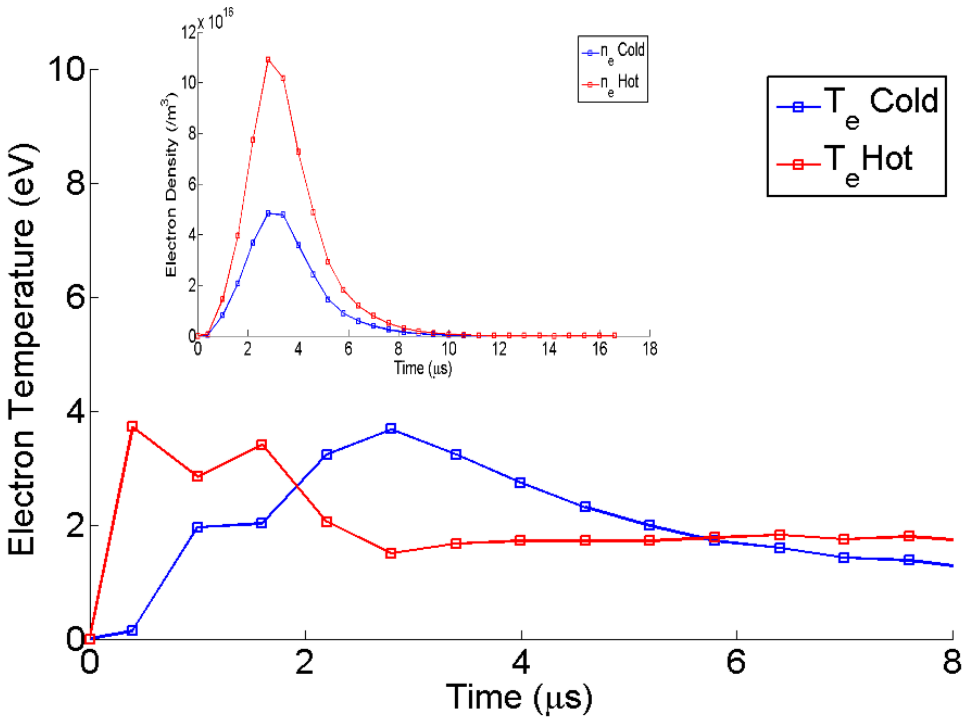

Figure 3.40: Time resolved temperature of Si plasma from Langmuir theory. (inset) density calculated from orbital motion theory. I=2 $\times$ 10^{13} Wcm^{-2}, λ_{LASER} = 800 nm

All three distributions are characterized by a strong prompt electron signal at $\approx$ .2 μs, followed by a multiplicity of ion peaks which suggests plume fragmentation. The strong positive signal at ca. 1 $\mu s < t <$ 2 μs that is visible in panels a) and b) is attributed to an initial excess of ions in the plasma plume. It is noted that this positive signal does not disappear even when the probe is positively biased up to 20 V indicating that this peak can be attributed to an initial violation of charge neutrality in the plume that results in an excess of high energy ions. The fact that this peak is not visible in the 400 nm data could be a further indication that there is no clear double layer formation in this plasma. In Figure 3.42 , the ion saturation signal is shown. It is noted in this case, that there is an inversion of the peak ratios

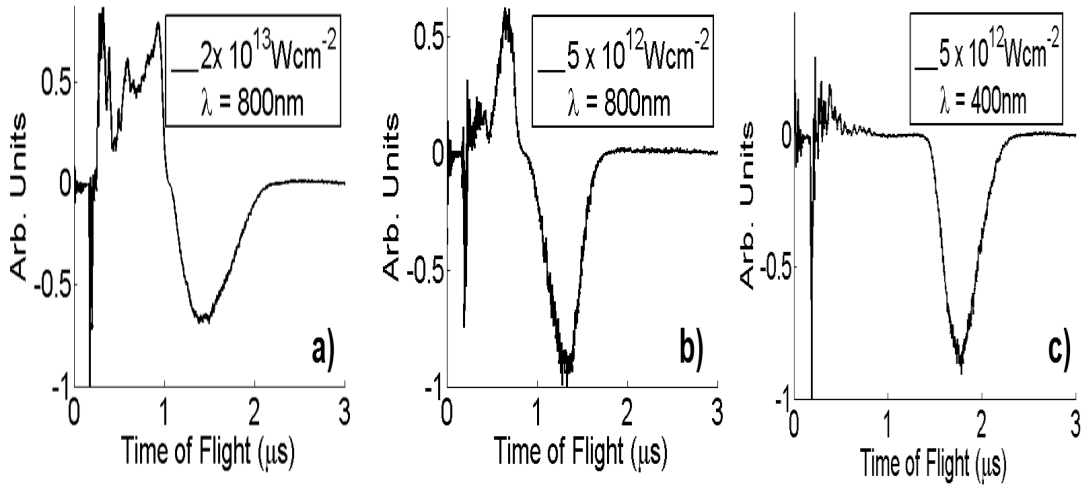

Figure 3.41: Time-of-flight traces for the three experimental conditions with probe voltage 0 V. The distributions have been normalised to their maxima

(N_{fast}/N_{slow}) in case b). It has been suggested [26] that an inversion of the fast/slow ratio is an indication of double layer formation.

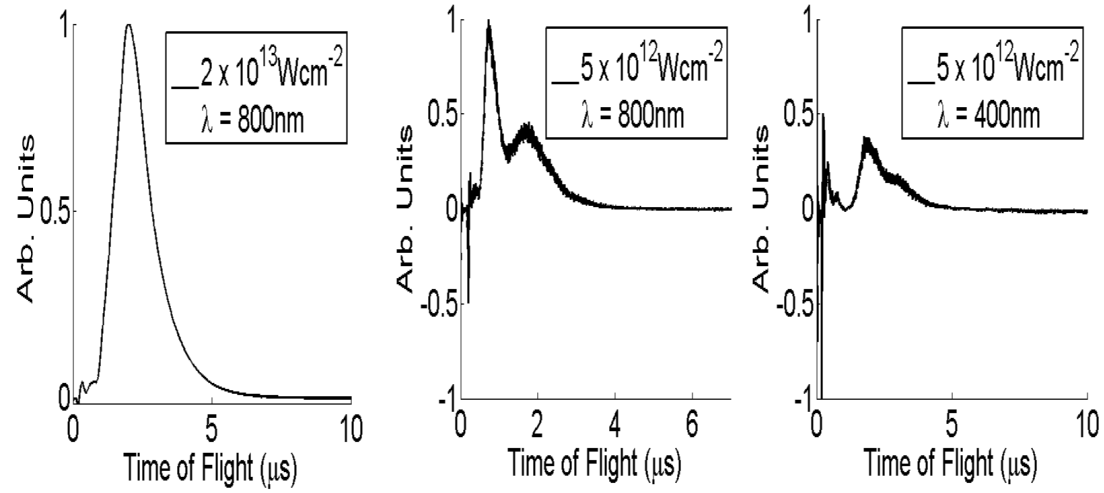

Figure 3.42: Time-of-flight traces for the three experimental conditions with probe voltage -60 V. The distributions have been normalised to their maximum

For the sake of display, the probe electron signals are shown in Figure 3.43. It can be clearly seen in this case that the only clearly visible fast electron peak occurs for case b) which is the experimental conditions that show a strong presence of two distinct electron temperatures. This lends further weight to the idea that a well defined double layer is characterised by a fast electron peak. The difference in most probable kinetic energy for the electron signals in Figure 3.43 is explained by the fact that, as stated before, the 400 nm laser light distributes a similar amount of energy to a smaller number of particles resulting in electrons with higher kinetic energies.

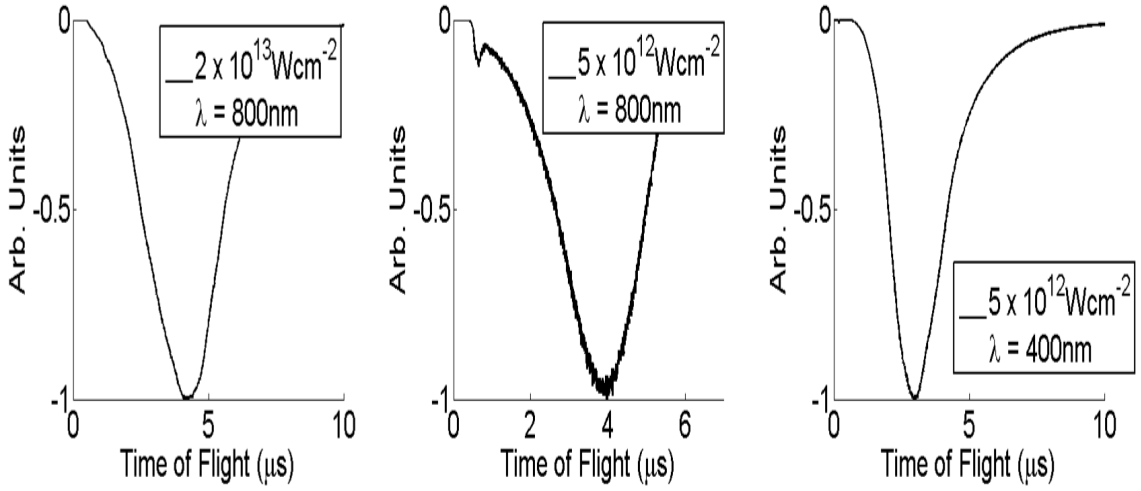

Figure 3.43: Time-of-flight traces for the three experimental conditions with probe voltage +60 V. The distributions have been normalised to their maxima

It appears then, in conclusion, that with the current experimental configuration a well defined double layer is found in the plasma for 800 nm laser light in the intensity region of 10^{12} Wcm^{-2}. However, evidence of a fast electron peak is apparent in the 400 nm data when the probe voltage is very high, indicating that that there may be two electron populations but that these have similar temperatures and densities.

3.9 Results: Expansion dynamics and double layer formation in Si Plasma

3.9.1 Un-biased probe: Expansion data

In an attempt to study the spatial formation of the double layer, another experiment was performed to study the I-V characteristics of a silicon laser produced plasma at various probe-target distances. In this experiment, the expansion probe was used. That is, the probe was placed parallel to the plasma flow direction in contrast to all previous experiments where the probe was perpendicular to the plasma flow. The intensity in these experiments was set to 2×10^{12} Wcm^{-2}. The value was chosen because it was found through trial and error that 2×10^{12} Wcm^{-2} was the highest power density that allowed the probe to be brought within 2 mm to the silicon-target due to the maximum current output of the power supply (33 mA). A higher intensity (or shorter probe - target distance) resulted in saturation of the ion/electron signal and an essential short circuit of the power supply. The specific aims of this experiment were to investigate how the double layer, if formed, varies spatially as a function of the target-probe distance and to also determine whether a double layer is formed at 400 nm at different distances from the target.

Planar expansion of the plasma is assumed. This assumption is based on previous polarisation measurements which indicated that at an intensity of 2×10^{12} Wcm^{-2}, the absorption by the target material is governed by the optical skin effect and the plasma dimension (the initial extent of the plume will be roughly $0.2\lambda_L$ where λ_L is the laser wavelength. This puts the estimation of the plume length at $\approx .4\ \mu m$ which is much less than the laser spot size, indicating planar expansion (planar expansion is assumed for cases where the laser spot size is much greater than the plume length [55]).

In the first part of the experiment, the time of flight distribution of an unbiased Langmuir probe was measured for various probe-target distances for both 800 and 400 nm. This data, shown in Figure 3.44, displays a similar plume structure for both 800 and 400 nm radiation with the exception of a possible narrow electron peak in the

400 nm data which is not present in the 800nm data. Both datasets can be described by the same general features. Firstly, a very prompt peak is noticed which coincides temporally with the photodiode trigger signal. Similarly, the peak does not shift in time as the probe-target distance is changed. It is assumed then that this peak is due to ionization of the probe by EUV/VUV light emitted from the plasma serving as a natural "time zero" for the data set. Secondly, in both datasets, a very fast (ca. 100 ns) electron peak is observed (marked A in the 800 nm data). This is interpreted as being due to a very fast layer of electrons that are quickly heated to above the Fermi temperature and subsequently behave as if they are completely detached from the main plasma. The broad positive feature (ca. 400 ns) is attributed to an excess of ions in the plume indicating a violation of charge neutrality, similar to what was seen in the last section (this is marked B in the 800 nm data). The third feature seen in the datasets (marked C in the 800 nm panel) is a broad, slightly negative signal that is most visible at small probe-target distances. This is attributed to electrons in the plume that are attached to the main core of the plasma plume but have a high temperature. Because of this high temperature they are able to 'push' through the positive sheath that is formed around the probe due to the excess of ions in the plume [33].

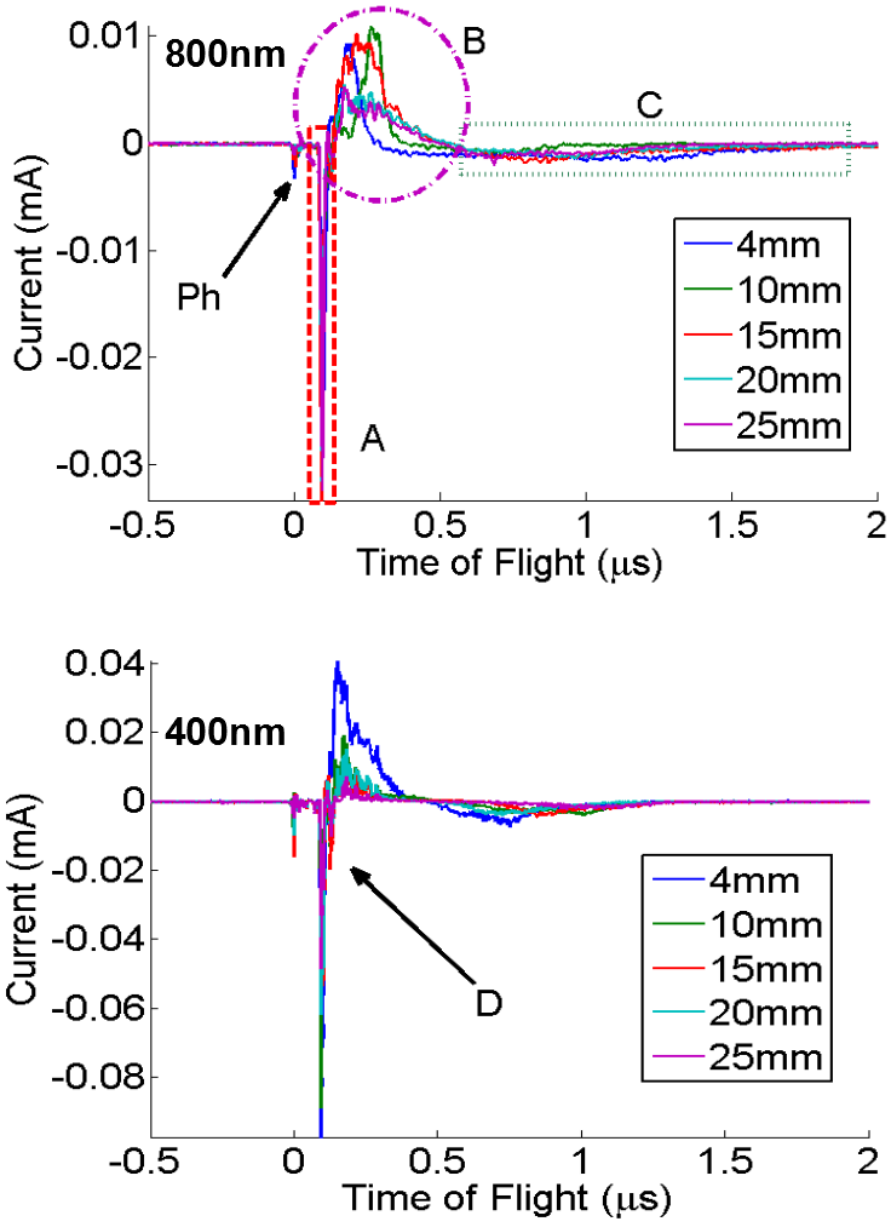

Figure 3.44: Time-of-flight as the probe is moved further from the target with both 800 nm and 400 nm light.

3.9.2 4 mm I-V expansion data

In a second part of the experiment, the I-V behaviour of the plasma was studied at various probe-target distance values. Figure 3.45 shows the time of flight distribution for a target-probe distance of 4 mm. For clarity, only the probe voltages ±100 V are shown.

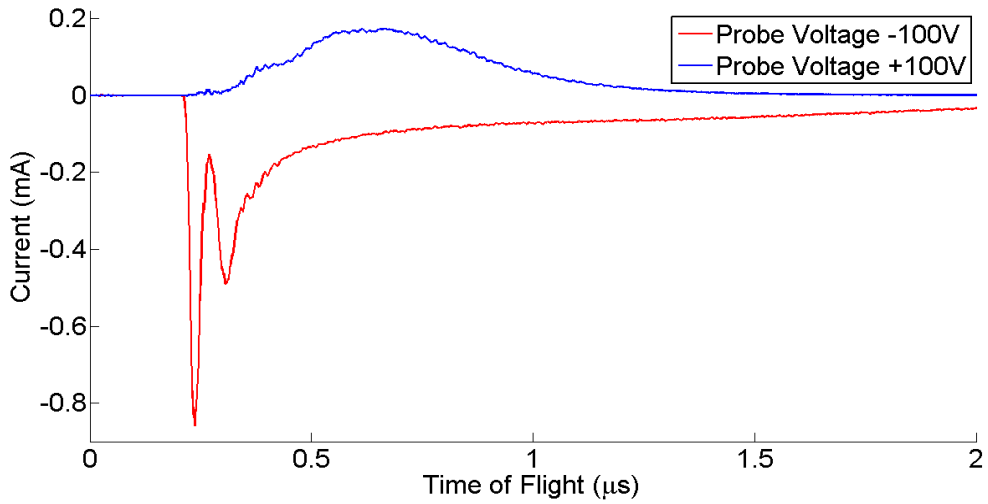

Figure 3.45: Time-of-flight traces for a probe-target distance of 4 mm. Only ±100 V is shown.

From Figure 3.45, it can be seen that two distinct fast electron peaks appear followed by a third very gradual slow component. For the ions, there are two distinct features, a fast ion signal which arrives at approximately the same time as the fastest electron peak. A slower, broader component is then visible at later times (ca. 0.6 μs). At times corresponding to the peak time of each feature which, from Figure 3.45, is 0.21 μs , .29 μs (fastest electron features), 0.61 μs (slow ion feature) and 1.3 μs (slow electron feature), the current versus probe voltage is plotted in Figure 3.46.

The times 0.21 μs, 0.29 μs and 1, .3 μs all show I-V dependent behaviour which is analysable by Langmuir theory. However, at .61 μs, there is a strong linear relationship between applied voltage and induced current indicating ohmic behaviour of the

plasma in this region. A linear fit to the 0.61 μ s data (shown inset in Figure 3.46) returns a slope whose reciprocal is 1.0×10^6 Ω. A Langmuir analyis of the 0.21 μs data returns an electron temperature of 5.5 eV and a plasma potential of 14 V. The 0.29 μs data returns a plasma temperature of 5.2 eV with a plasma potential of 14 V. For .67 μs, the analysis returns a temperature of 2.1 eV with a potential of 7 V. Thus, the data behaves as if there are two distinct electron populations separated by an ohmic conductor. The potential difference ($\Delta V = V_{0.29\mu s} - V_{1.3\mu s}$= 7 V),indicates that the electromotive force (EMF) generated by this potential difference will have the effect of accelerating the slow electron component. The thermal and electrostatic equilibrium between the two fast electron peaks seems to suggest that these two peaks are part of a single fast electron component which has a drop in density in the middle. The small temperature drop in the fast electron feature between $0.21\mu s$ and 0.29 μs is explained by calculating the difference in electron density at the two times. An OML theory analysis of the electron densities reveals an electron density of 2.6×10^{15} m^{-3} for the 0.21 μs peak and 1.1×10^{15} m^{-3} for the 0.29 μs peak indicating that the electron cloud in the plume expands as the plume propagates and cools in the process of expansion.

3.9.3 10 mm I-V expansion data

The experiment was repeated with a target probe distance of 10 mm. An ohmic region is again found at .87μs which is the temporal region in between the two distinct electron regions. A linear fit to this data returns a slope whose reciprocal is $5.1 \times 10^5\Omega$ indicating an increase in the conductivity of the ohmic region at 10 mm.

For the $.28\mu s$, $.0.40\mu s$ and $2\mu s$ peaks which represent the two fast electron components and the slow electron component, a Langmuir analysis is viable. The fast electron component is found to have a temperature of 4.2 eV and a potential of 19 V. The next electron peak (at a time of 0.4 μs) is found to have a temperature of 3.2 eV and a potential of 14 V. The slow electron component is found to have a temperature of 2.1 eV and a potential of 7 V. The main difference, then, between the plasma at 4 mm and 10 mm seems to be the creation of a potential difference

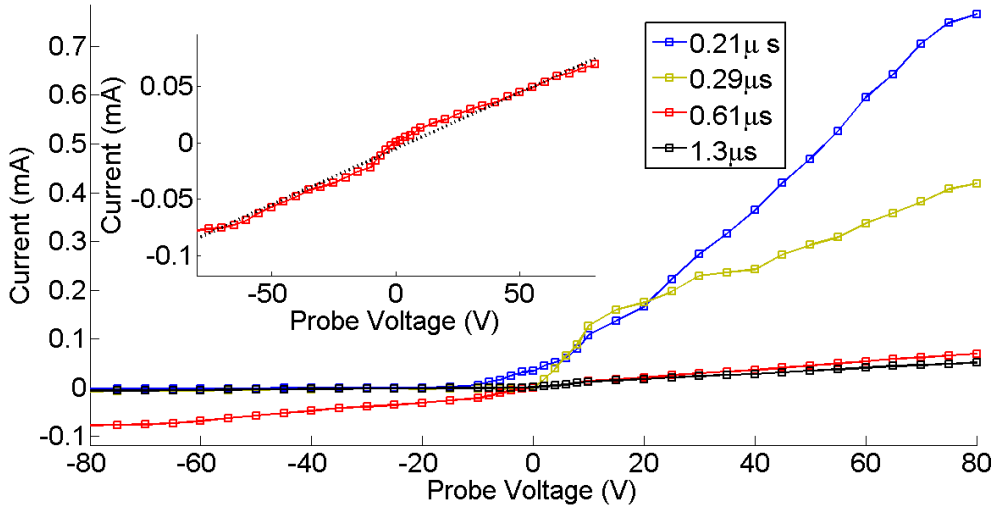

Figure 3.46: I-V characteristics for the data in Figure 3.45. Shown inset is the ohmic behaviour at $0.61\mu s$

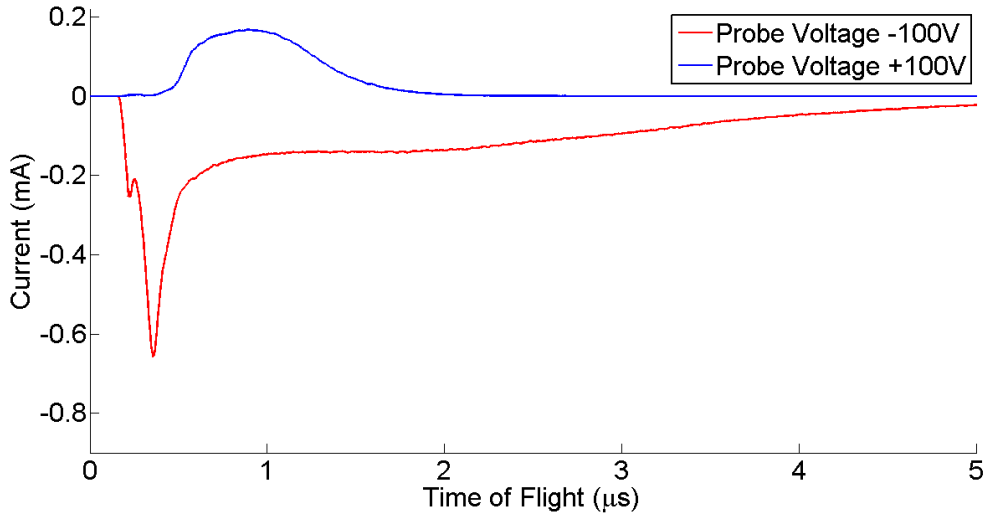

Figure 3.47: Time-of-flight traces for a probe-target distance of 10 mm. Only ±100 V is shown.

between the first two electron peaks which is presumably due to the Coulombic repulsion between the two peaks. In general the 10 mm data behaves very similarly to

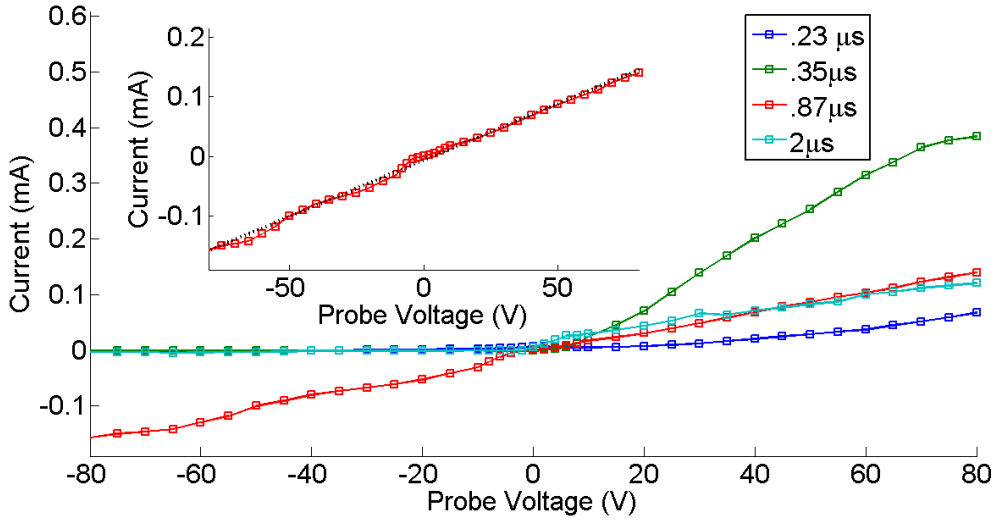

Figure 3.48: I-V characteristics for the data in Figure 3.47. Shown inset is the ohmic behaviour at 0.8 μs

the 4 mm data however the changes in temperature and potential and general shape of the electron / ion current signals suggest the formation / evolution of thermal and potential gradients in the plume. The hypothesis is then that as the plume expands forward it splits into quasi-neutral sub-bunches due to the formation of thermal and potential barriers. The expansion process is further studied by studying the plume behaviour at 15 mm

3.9.4 15 mm I-V expansion data

3.9.5 25 mm I-V expansion data

At 25 mm, the familiar dual peak structure in the electron / ion plume is observed. It also appears that the plume has expanded and cooled. No Ohmic region is present, and an analysis of temporal regions which correspond to similar velocities as the previous three sections result in individual component temperatures of 0.9 eV (for the feature at $\approx 0.59\mu$s, 1.1 eV (for the feature at ≈ 1.5 μs) and 0.7 eV for the feature at ≈ 4 μs. The feature at 1.5 μs (where again it is noted that this feature has

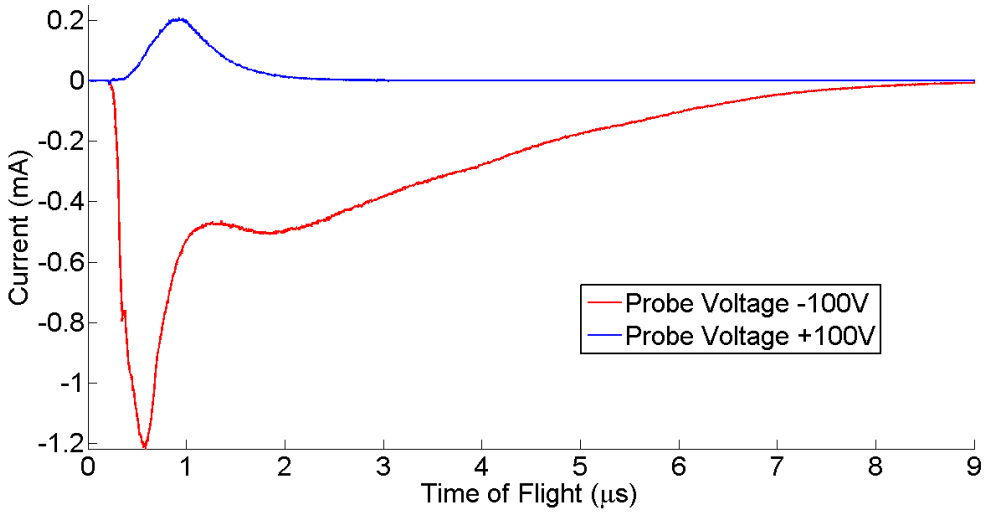

Figure 3.49: Time-of-flight traces for a probe-target distance of 15 mm. Only ±100 V is shown.

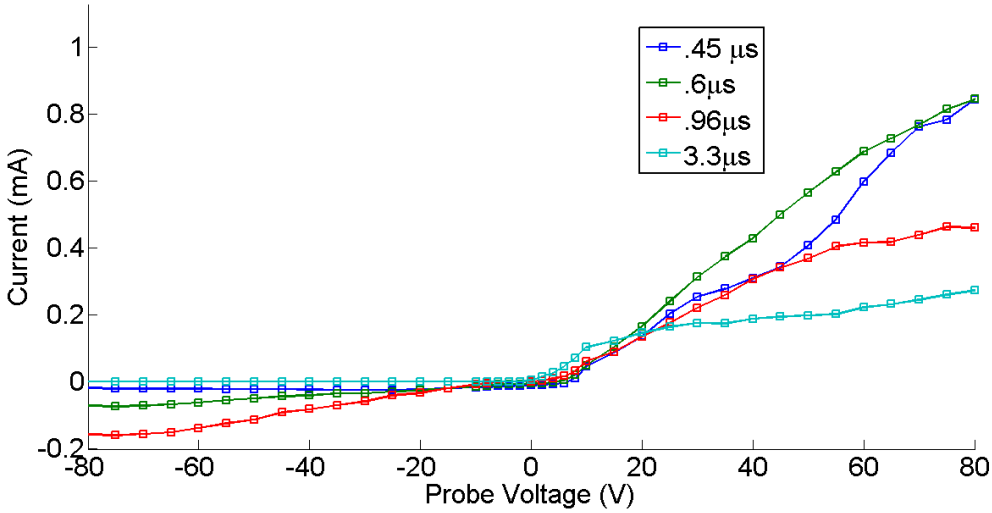

Figure 3.50: I-V characteristics for the data in Figure 3.47.

a velocity on the order of that of the ohmic regions in the 4mm and 10mm data), a double layer is again visible however the temperatures are somewhat closer (0.7 and

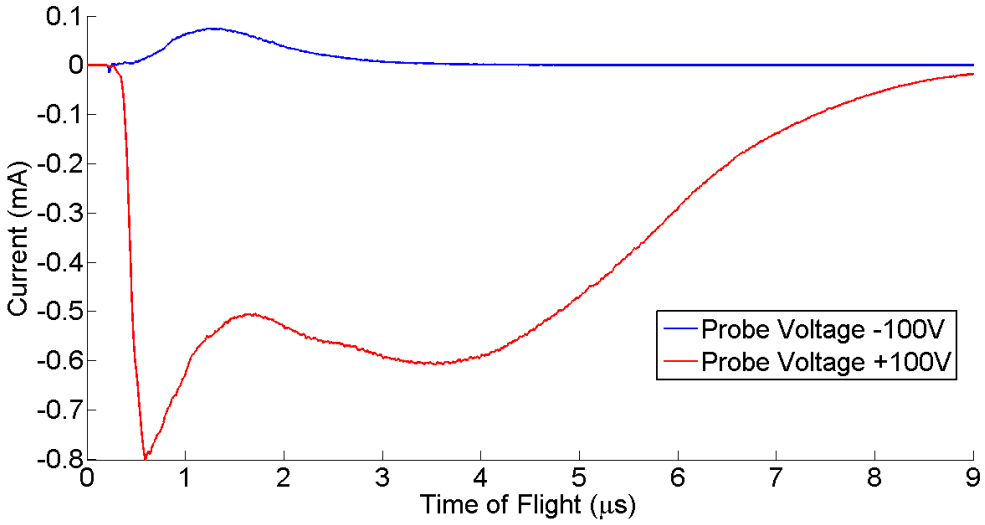

Figure 3.51: Time-of-flight for a probe-target distance of 25 mm. Only ±100 V is shown.

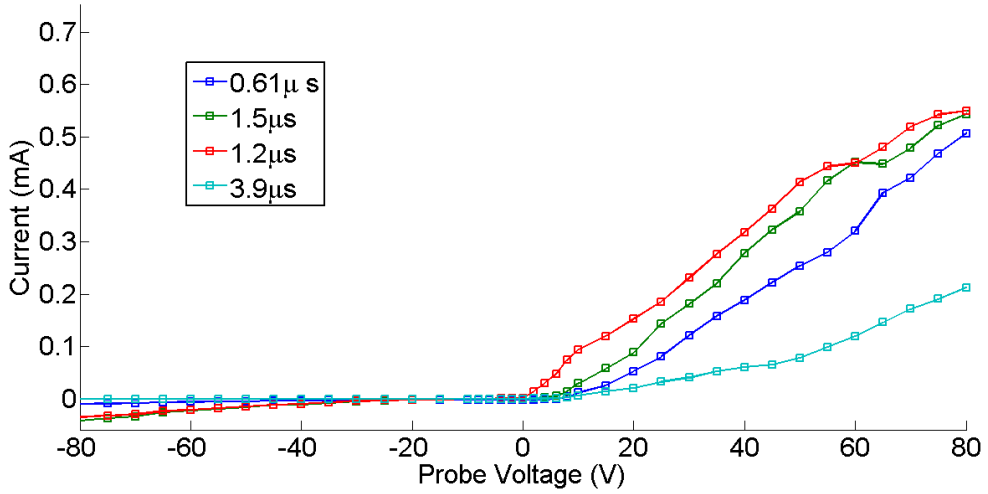

Figure 3.52: I-V characteristics for the data in Figure 3.51.

2.7 eV), as are the potentials (4 V and 15 V).

3.9.6 Expansion data for ablation at 400 nm

The time-of-flight signals for target-probe distances of 10 mm and 25 mm are shown in Figures 3.53 and 3.54.

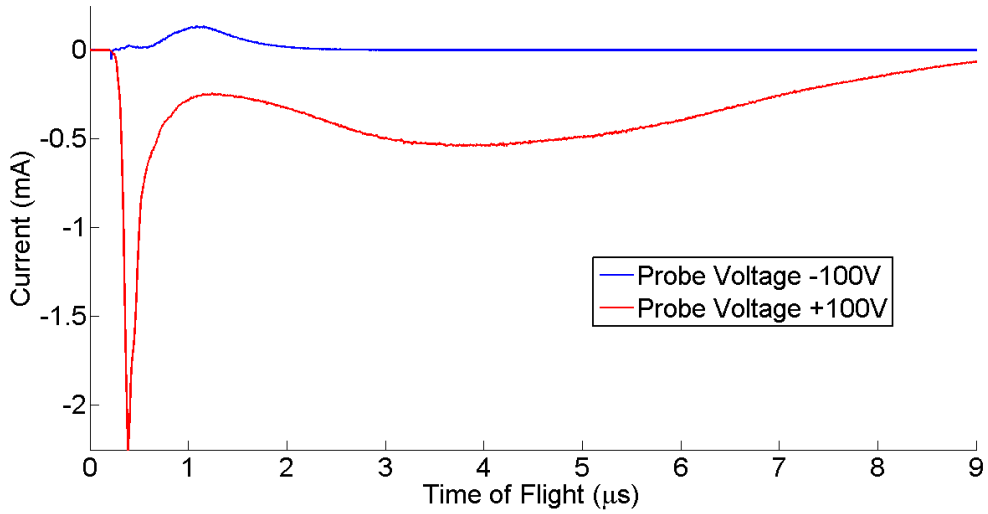

Figure 3.53: Time-of-flight traces for a probe-target distance of 10 mm with 400 nm laser light. Only ±100 V is shown.

The qualitative behaviours of the electron and ion signals are the same at 400 nm and 800 nm. However, at 10 mm target-probe distance, the 400 nm data shows no ohmic region (in contrast to the 800 nm data) and also only a single fast electron component. The temperature gradient between the two electron components is roughly the same as the 800 nm case although the overall temperature is lower (the temperature varies from 3 eV to 1.2 eV between 0.5 and 5 μs). The plasma potential was found to vary from 32 V at 0.5 μs to 10 V at 5 μs. At 25 mm, the plasma has a near uniform potential (11 V).

It is clear from the data then that the plasma expansion behaviour is much different at 400 nm than at 800 nm and this goes some way to explaining why a strong double layer is present in the 800 nm case and not the 400 nm case. Further study is required to fully explain the expansion dynamics however it appears that

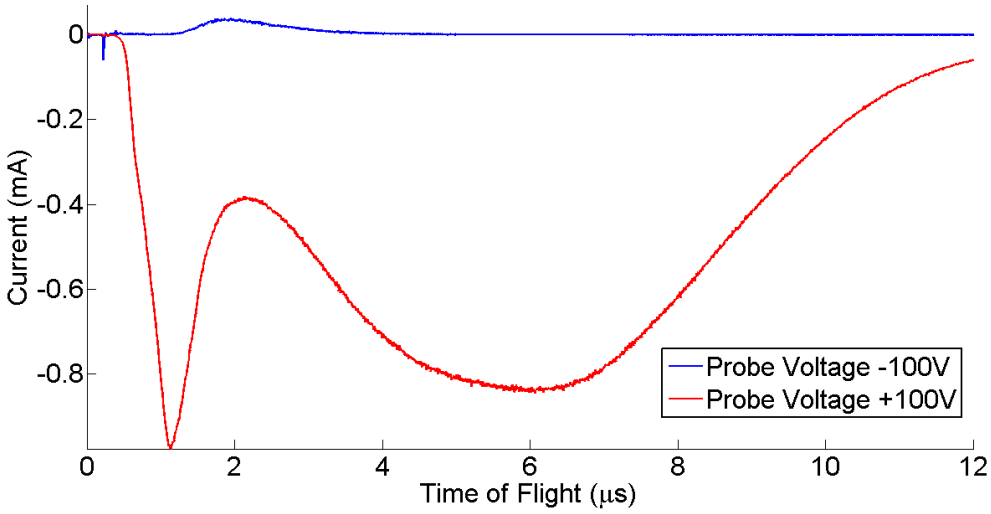

Figure 3.54: Time-of-flight for a probe-target distance of 25 mm with 400 nm laser light. Only ±100 V is shown.

the double layer in the 800 nm case is driven by a strongly ohmic region at early expansion phases in the plume.

3.10 Summary and future work

In summary, ultrafast laser ablation experiments were performed for a silicon-target in the $10^{12} - 10^{13}$ W/cm^2 regime. This is an interesting irradiance region as it overlaps irradiance regions traditionally found in long pulse laser experiments yet the laser fluence is much lower. Using a Langmuir probe diagnostic, features reminiscent of long pulse laser experiments are found such as double layer formation, multiple electron species and ion acceleration. The electron species in the plume are found to behave differently with respect to the laser polarisation state than the ionic counterpart and it is hypothesised that this is due to resonantly excited electrostatic fields which cause a reduction in thermal transport. It is found that the plume expansion is highly dependent on laser wavelength and a highly ohmic region in the expansion of the 800 nm plume is presented as the driving mechanism behind the double layer

formation.

The installation of a single shot capability such as a Pockels cell or a fast shutter [57] in the experimental configuration will allow for a more rigorous study of the plume dynamics. Similarly, the pulse broadening caused by the optics can be reduced by placing the half wave plate before the compressor inside the laser instead of its location in these experiments (just before the last routing mirror).

Bibliography

[1] W. Lochte-Hotlgreven. *Plasma Diagnostics (American Vacuum Society Classics)*. 1995.

[2] D. Strickland and G. Mourou. Compression of amplified chirped optical pulses. *Optics Communications*, **56**:219, 1985.

[3] E.G. Gamaly and A.V. Rode and V.T. Tikhonchuk and B. Luther-Davies. Electrostatic mechanism of ablation by femtosecond lasers. *Applied Surface Science*, **197**:699–704, 2002.

[4] V. Iannotti and S. Amoruso and G. Ausanio and R. Bruzzese and L. Lanotte and A.C. Barone and G. Margaris and K.N. Trohidou and D. Fiorani. Stepwise behaviour of magnetization temperature dependence in iron nanoparticle assembled films. *Nanotechnology*, **24**(16):165706, 2013.

[5] P.B. Corkum and F. Brunel and N.K. Sherman and T. Srinvasanrao. Thermal response of metals to ultrashort-pulse laser excitation. *Physical Review Letters*, **61**(25):2886–2889, 1988.

[6] T. Donnelly and J.G. Lunney and S. Amoruso and R. Bruzzese and X. Wang and X. Ni. Dynamics of the plumes produced by ultrafast laser ablation of metals. *Journal of Applied Physics*, **108**(4):043309, 2010.

[7] S. Amoruso and X. Wang and C. Altucci and C. de Lisio and M. Armenante and R. Bruzzese and R. Velotta. Thermal and nonthermal ion emission during high-

fluence femtosecond laser ablation of metallic targets. *Applied Physics Letters*, **77**(23):3728–3730, 2000.

[8] S.I. Anisimov and B.L. Kapeliov and T.L. Perelman. Electron-emission from surface of metals induced by ultrashort laser pulses. *Zhurnal Eksperimentalnoi i Teoreticheskoi Fiziki*, **66**(2):776–781, 1974.

[9] B. Verhoff and S.S. Harilal and A. Hassanein. Angular emission of ions and mass deposition from femtosecond and nanosecond laser-produced plasmas. *Journal of Applied Physics*, **111**(12):123304, JUN 15 2012.

[10] S. Darvishi and T. Cubaud and J.P. Longtin. Ultrafast laser machining of tapered microchannels in glass and pdms. *Optics and Lasers in Engineering*, **50**(2):210–214, 2012.

[11] S. Amoruso and R. Bruzzese and N. Spinelli and R. Velotta and M. Vitiello and X. Wang and G. Ausanio and V. Iannotti and L. Lanotte. Generation of silicon nanoparticles via femtosecond laser ablation in vacuum. *Applied Physics Letters*, **84**(22):4502–4504, 2004.

[12] K.F. Al-Shboul and S.S. Harilal and A. Hassanein. Emission features of femtosecond laser ablated carbon plasma in ambient helium. *Journal of Applied Physics*, **113**(16):163–305, 2013.

[13] T. Donnelly and J.G. Lunney and S. Amoruso and R. Bruzzese and X. Wang and X. Ni. Angular distributions of plume components in ultrafast laser ablation of metal targets. *Applied Physics A-Materials Science and Processing*, **100**(2):569–574, 2010.

[14] J. Yang and Y. Zhao and X. Zhu. Transition between nonthermal and thermal ablation of metallic targets under the strike of high-fluence ultrashort laser pulses. *Applied Physics Letters*, **88**(9):094101, 2006.

[15] A.V. Kabashin and M. Meunier. Synthesis of colloidal nanoparticles during femtosecond laser ablation of gold in water. *Journal of Applied Physics*, **94**(12):7941–7943, 2003.

[16] K. Ozono and M. Obara and A. Usui and H. Sunakawa. High-speed ablation etching of gan semiconductor using femtosecond laser. *Optics Communications*, **189**(1-3):103–106, 2001.

[17] F. Garrelie and J.P. Colombier and F. Pigeon and S. Tonchev and N. Faure and M. Bounhalli and S. Reynaud and O. Parriaux. Evidence of surface plasmon resonance in ultrafast laser-induced ripples. *Optics Express*, **19**(10):9035–9043, 2011.

[18] G.O. Williams and G.M. O'Connor and P.T. Mannion and T.J. Glynn. Langmuir probe investigation of surface contamination effects on metals during femtosecond laser ablation. *Applied Surface Science*, **254**(18):5921–5926, 2008.

[19] S. Nolte and C. Momma and H. Jacobs and A. Tunnermann and B.N. Chichkov and B. Wellegehausen and H. Welling. Ablation of metals by ultrashort laser pulses. *Journal of the Optical Society of America B-Optical Physics*, **14**(10):2716–2722, OCT 1997.

[20] D. Perez and L.J. Lewis. Molecular-dynamics study of ablation of solids under femtosecond laser pulses. *Physical Review B*, **67**(18):184102, 2003.

[21] R. Ramis and K. Eidmann and J. Meyer-ter-Vehn and S. Hueller. Multi-fs - a computer code for laser-plasma interaction in the femtosecond regime. *Computer Physics Communications*, **183**(3):637–655, 2012.

[22] E.G. Gamaly. The physics of ultra-short laser interaction with solids at non-relativistic intensities. *Physics Reports-Review Section of Physics Letters*, **508**(4-5):91–243, 2011.

[23] R. Miracoli and D. Mascali and N. Gambino and S. Gammino and L. Giuffrida and L. Torrisi. Plasma plume characterization through the analysis of ion current signals. *Radiation Effects and Defects in Solids*, **165**(6-10):584–591, 2010.

[24] B. Doggett and J.G. Lunney. Expansion dynamics of laser produced plasma. *Journal of Applied Physics*, **109**(9):093304, 2011.

[25] Z. Zhang and P.A. Van Rompay and P.P. Pronko. Ion characteristics of laser-produced plasma using a pair of collinear femtosecond laser pulses. *Applied Physics Letters*, **83**(3):431–433, 2003.

[26] S. Eliezer and H. Hora. Double-layers in laser-produced plasmas. *Physics Reports-Review Section of Physics Letters*, **172**(6):339–407, 1989.

[27] P. Nica and M. Agop and S. Miyamoto and S. Amano and A. Nagano and T. Inoue and E. Poll and T. Mochizuki. Multi-peak structure of the ion current in laser produced plasma. *European Physical Journal D*, **60**(2):317–323.

[28] G. Mainfray and C. Manus. Multiphoton ionization of atoms. *Reports on Progress in Physics*, **54**(10):1333–1372, OCT 1991.

[29] V.S. Popov. Tunnel and multiphoton ionization of atoms and ions in a strong laser field (keldysh theory). *Physics-Uspekhi*, **47**(9):855–885, 2004.

[30] P.P. Pronko and P.A. VanRompay and C. Horvath and F. Loesel and T. Juhasz and X. Liu and G. Mourou. Avalanche ionization and dielectric breakdown in silicon with ultrafast laser pulses. *Physical Review B*, **58**(5):2387–2390, 1998.

[31] A.H. Dogar and B. Ilyas and S. Ullah and A. Nadeem and A. Qayyum. Langmuir probe measurements of nd-yag laser-produced copper plasmas. *IEEE Transactions on Plasma Science*, **39**(3):897–900, 2011.

[32] B. Doggett and J.G. Lunney. Langmuir probe characterization of laser ablation plasmas. *Journal of Applied Physics*, **105**(3):033306, 2009.

[33] S. Tudisco and D. Mascali and N. Gambino and A. Anzalone and S. Gammino and F. Musumeci and A. Scordino and A. Spitaleri. Investigation of laser-produced aluminum plasma. *Nuclear Instruments and Methods in Physics Research Section A-Accelerators Spectrometers Detectors and Associated Equipment*, **653**(1):47–51, 2011.

[34] R.C. Issac and G.K. Varier and P. Gopinath and S.S. Harilal and V.P.N. Nampoori and C.P.G. Vallabhan. Prompt electron emission and collisional ionization of ambient gas during pulsed laser ablation of silver. *Applied Physics A-Materials Science and Processing*, **67**(5):163–165, 1998.

[35] D. Mascali and N. Gambino and R. Miracoli and S. Gammino and L. Torrisi and F. Maimone and L. Tumino. Plasma parameters measurements by means of langmuir probe. *Radiation Effects and Defects in Solids*, **163**(4-6):471–478, 2008.

[36] R.L. Merlino. Understanding langmuir probe current-voltage characteristics. *American Journal of Physics*, **75**(12):1078–1085, 2007.

[37] J.E. Allen. Probe theory - the orbital motion approach. *Physica Scripta*, **45**(5):497–503, 1992.

[38] S. Amoruso and X. Wang and C. Altucci and C. de Lisio and M. Armenante and R. Bruzzese and N. Spinelli and R. Velotta. Double-peak distribution of electron and ion emission profile during femtosecond laser ablation of metals. *Applied Surface Science*, **186**(1-4):358–363, 2002.

[39] S. Amoruso and M. Armenante and R. Bruzzese and N. Spinelli and R. Velotta and X. Wang. Emission of prompt electrons during excimer laser ablation of aluminum targets. *Applied Physics Letters*, **75**(1):7–9, 1999.

[40] R.C. Issac and P. Gopinath and G.K. Varier and V.P.N. Nampoori and C.P.G. Vallabhan. Twin peak distribution of electron emission profile and impact ionization of ambient molecules during laser ablation of silver target. *Applied Physics Letters*, **73**(2), 1998.

[41] F. Dorchies and P. Forget and P. Gallant and Z. Jiang and J.C. Kieffer and H. Pepin and O. Peyrusse. Polarization induced modification of thermal radiative properties of solid density plasmas produced by subpicosecond laser. *Physics of Plasmas*, **8**(12):5239–5243, 2001.

[42] S. Kato and B. Bhattacharyya and A. Nishiguchi and K. Mima. Wave breaking and absorption efficiency for short pulse p-polarized laser-light in a very steep density gradient. *Physics of Fluids B-Plasma Physics*, **5**(2):564–570, 1993.

[43] J.C. Kieffer and J.P. Matte and S. Belair and M. Chaker and P. Audebert and H. Pepin and P. Maine and D. Strickland and P. Bado and G. Mourou. Absorption of an ultrashort laser-pulse in very steep plasma-density gradients. *IEEE Journal of Quantum Electronics*, **25**(12):2640–2647, 1989.

[44] K.R. Manes and V.C. Rupert and J.M. Auerbach and P. Lee and J.E. Swain. Polarization and angular-dependence of 1.06-mum laser-light absorption by planar plasmas. *Physical Review Letters*, **39**(5):281–284, 1977.

[45] J.S. Pearlman and J.J. Thomson. Polarization-dependent energy-transport in laser-produced plasmas. *Applied Physics Letters*, **32**(11):703–705, 1978 1978.

[46] R.P. Godwin and R. Sachsenmaier and R. Sigel. Angle-dependent reflectance of laser-produced plasmas. *Physical Review Letters*, **39**(19):1198–1201, 1977.

[47] H. Cai and W. Yu and S. Zhu and C. Zheng and L. Cao and B. Li and Z.Y. Chen and A. Bogerts. Short-pulse laser absorption in very steep plasma density gradients. *Physics of Plasmas*, **13**(9):094504, 2006.

[48] J.S. Pearlman and J.J. Thomson and C.E. Max. Polarization-dependent absorption of laser-radiation incident on dense-plasma planar targets. *Physical Review Letters*, **38**(24):1397–1400, 1977.

[49] W.L. Kruer. *The Physics of Laser Plasma Interactions*. Frontiers in Physics. Addison Wesley, 1st edition, 1988.

[50] J. C. Kieffer and P. Audebert and M. Chaker and J.P. Matte and H. Pepin and T.W. Johnston and P. Maine and D. Meyerhofer and J. Delettrez and D. Strickland and P. Bado and G. Mourou. Short-pulse laser-absorption in very steep plasma-density gradients. *Physical Review Letters*, **62**(7):760–763, 1989.

[51] S. Eliezer and H. Hora and E. Kolka and F. Green and H. Szichman. How double layers accelerate charged particles. *Laser and Particle Beams*, **13**(3):441–447, 1995.

[52] J.I. Apinaniz and R. Martinez. Theoretical study of ion acceleration by double-layer formation in multicharged laser-produced plasmas. *IEEE Transactions on Plasma Science*, **39**(11):2928–2929, 2011.

[53] N.M. Bulgakova. Possibility of rarefaction shock wave under short pulse laser ablation of solids. *Physical Review E*, **60**(4):R3498–R3500, 1999.

[54] K. Sato and F. Miyawaki. Formation of presheath and current-free double-layer in a 2-electron-temperature plasma. *Physics of Fluids B-Plasma Physics*, **4**(5):1247–1254, 1992.

[55] N.M. Bulgakova and A.V. Bulgakov and O.F. Bobrenok. Double layer effects in laser-ablation plasma plumes. *Physical Review E*, **62**(4):5624–5635, 2000.

[56] P. Yeates and J.T. Costello and E.T. Kennedy. The dcu laser ion source. *Review of Scientific Instruments*, **81**(4):043305, 2010.

[57] L.P. Maguire and S. Szilagyi and R.E. Scholten. High performance laser shutter using a hard disk drive voice-coil actuator. *Review of Scientific Instruments*, **75**(9):3077–3079, 2004.

Chapter 4

Ionization of molecules

This chapter focusses on the development of a linear time-of-flight mass spectrometer based on the designs of Wiley and McLaren [1]. A brief history of time-of-flight mass spectrometry is given as well as an overview of the basic ionization processes found to underpin the interaction of atoms and molecules with intense laser light. To demonstrate the principle of operation of the time-of-flight apparatus, an experiment is performed on an effusive gas jet of N_2. The angular distribution of both the ionized molecule and the atomic fragments is measured by rotating the laser electric field vector with a half wave plate. The results are found to be in excellent agreement with previously published results on similar experiments. The angular distributuon of the singly ionized molecule is found to be isotropic whereas the atomic fragments (N^+, N^{2+} and N^{3+}) is found to be highly anisotropic. It is reasoned that this anisotropy results from dynamic alignment of the ionized molecule pre-dissociation.

4.1 History of TOF-MS

In the late 19th century, Joseph Hittorf set up an experiment. He took a sealed glass vessel and removed the air with a vacuum pump. A metal plate suspended inside the vessel was connected by way of a feedthrough to a power supply, such that the plate could be charged to a high negative potential [2]. A phosphor screen placed at the opposite end of the sealed vessel showed a glow when the plate was charged. Furthermore, the glow was found to shift position under the influence of a magnetic field. Also, a screen placed between the plate and the phosphor resulted in a shadow being cast on the phosphor. It was concluded, then, that the glow was caused by a stream of negatively charged particles. These rays were called 'cathode rays' and eventually led to the discovery of the electron by JJ Thomson [3].

A complementary set of experiments were performed by Gouldstein in 1886. Gouldstein used a perforated cathode to observe a stream of positively charged particles moving in the opposite direction to the cathode rays. These were dubbed 'canal rays' and were found to behave differently under magnetic fields than the cathode rays. Specifically, different parts of the canal rays were shifted by different amounts which suggested that the canal rays did not contain particles which all had the same mass. Similarly, the shift of the canal rays changed depending on what gas was in the glass vessel. These experiments were the foundation of modern mass spectrometry.

By this time, Prout's hypothesis (which states that the weight of all atoms were multiples of the weight of hydrogen) was under threat with the discovery that the atomic mass of calcium was a non-integer multiple of the atomic mass of hydrogen. This new field of mass spectrometry would have a hand in resolving the confusion. Experiments with canal rays from a neon discharge revealed that the neon gas was comprised of atoms with two different masses. This was the first observation of a stable isotope [4].

It was not until Chadwick's discovery of the neutron [5] in 1932 that the true nature of isotopes was revealed. The neutron is a nucleon with no electrical charge. Two atoms can have the same number of electrons and protons but a different number

of neutrons: These two atoms are called isotopes of a particular element. The most stable and abundant isotope needn't be the isotope with an equal number of protons and neutrons. This was the first significant problem solved by mass spectrometry.

Modern mass spectrometry exists in many forms. Static magnetic and electric fields can be used together and separately to analyse an electrically charged species. For example, a travelling positive or negative charge can be deflected by a number of electrically charged plates [6]. By the work-energy theorem the degree of deflection will be determined by the particle's mass to charge ratio. Similarly, a charged plate can accelerate a charged particle by an amount determined by its mass to charge ratio. Its time of flight over a fixed and known distance is then a measure of this mass to charge ratio [6].

Today, mass spectrometers are widely used in both industry and academia. A benchmark paper in 1955 [1] gave an extensive mathematical and experimental description of the resolution limits of time-of-flight devices. In contrast to a particle deflection method, time-of-flight devices have very high or even infinite upper limits on the mass of the detected particles. This makes time-of-flight devices particularly suited to the detection of fragments of biomolecules and large amino-acids [7, 8].

4.2 TOF-MS principle of operation

The essential and basic constituents of a time-of-flight spectrometer are:

- An ionization source
- An extraction region
- A drift region

For the experiments presented here, the source of ionization is laser irradiation of a neutral gas jet. The configuration used in this work is a linear, two stage time-of-flight spectrometer commonly known as a 'Wiley-McLaren TOF'. The basic configuration is shown in Figure 4.1. Ions are created between two biased plates

with a constant electric field E_s between them. The force of the electric field then extracts the ions into the region labelled 'd' where another constant electric field E_d exists. The ions then travel into the drift region D where there is zero electric field. This drift region allows ions of different mass/charge ratios separate in time such that they can be distinguished at the detector "Q".

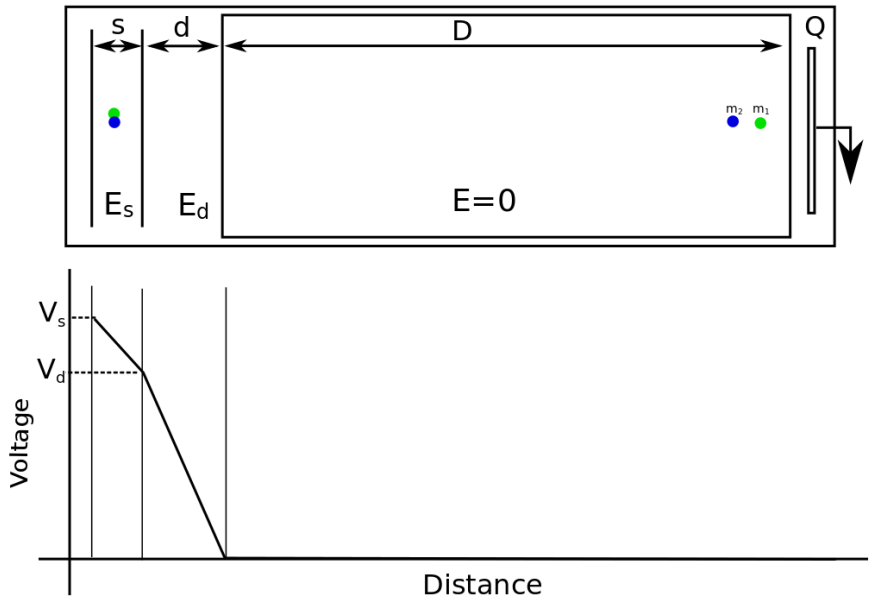

Figure 4.1: Schematic showing the basic configuration of a Wiley-McLaren TOF

The total flight time of an ion from the ionization source to the detector is given by [1]:

$$T = \left(\frac{m}{2q(sE_s + dE_d)}\right)^{1/2} \left(2k_o^{1/2}s_o + \frac{2k_o^{1/2}d}{k_o^{1/2}+1} + D\right) \tag{4.1}$$

where T is the total flight time, m is the ion mass, q is the ion charge, s_o is the initial ionization location and k_o is given by:

$$k_o = \frac{s_o E_s + dE_d}{s_o E_s} = \frac{V_s + V_d}{V_s} \tag{4.2}$$

From Equations 4.1 and 4.2, it is seen that the time of flight of an ion is governed not only by the geometry of the set up (s_o, D, d) but also by the potentials applied to the first two plates (V_s, V_d). In reality, all of the ions with the same mass to charge ratio will not be created at the same point in the extraction field E_s due to the finite spot size of the focal point within the laser. This means that although all the ions are extracted by the same uniform field, the distance they travel (and hence the acceleration they receive) within this field will be different for two ions created at different spatial locations. This will lead to a temporal spread in the ion peak which will limit the resolution. The spatial plane at which these two ions pass each other is governed by the ratio E_s/E_d. The best resolution of a Wiley McLaren TOF is reached when E_s/E_d is tuned such that two ions of the same m/q but created at different points in space will enter the field free drift tube with the same speed. This is known as the "Wiley-McLaren" condition [1].

4.3 Theory

4.3.1 Single photon ionization

Single photon ionization is a process whereby a single photon can interact with a single electron to produce an ion. Work by Einstein [9], which led to him being awarded the Nobel Prize for physics in 1921, describes how this process, known as the photoelectric effect, works. An electron is bound to an atom with a particular binding energy ϕ. This electron can be liberated from the atom by a photon if that photon has an energy which is greater than the binding energy of the electron to the atom. The kinetic energy of this liberated electron will be given by:

$$KE_{electron} = \hbar\omega - \phi \tag{4.3}$$

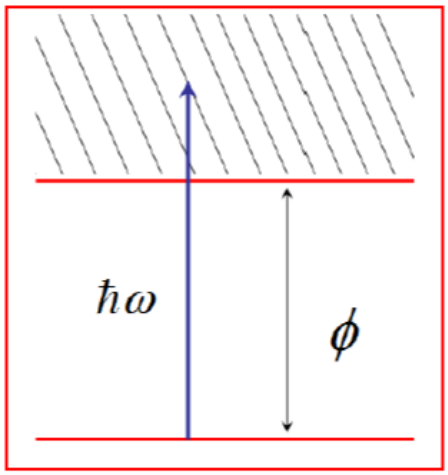

Figure 4.2: Schematic showing the photoelectric effect.

4.3.2 Multiphoton ionization

It is possible to ionize the atom with photons that have a lower energy than the binding energy [10]. A photon whose energy is lower than the binding energy, can transfer its energy to an electron and promote it to some virtual state that lies below the continuum threshold. The lifetime of this state will be governed by the Heisenberg uncertainty principle [10]. The probability of the electron absorbing another photon while in this virtual state will be directly related to the photon density and hence flux. In this way, should the laser be intense enough, an electron can absorb N photons of energy $\hbar\omega$ and reach the continuum. This is known as multiphoton ionization. Should the electron encounter a resonant atomic state along its way to

the continuum, the ionization signal will be greatly enhanced in a process known as Resonance Enhanced Multiphoton Ionization (REMPI) [11]. It was observed in 1979 that an electron that has been liberated from an atom by the absorption of photons can go on to absorb additional photons while in the continuum. This process, known as Above Threshold Ionization, is a direct consequence of the electron being in the presence of an intense laser field [12]. The kinetic energy of the emitted electron will be given in each case by:

$$KE_{electron} = (N + S)\hbar\omega - \phi \tag{4.4}$$

where N is the number of photons required to liberate the electron from the atom and S is the number of additional photons that the electron absorbs while in the continuum.

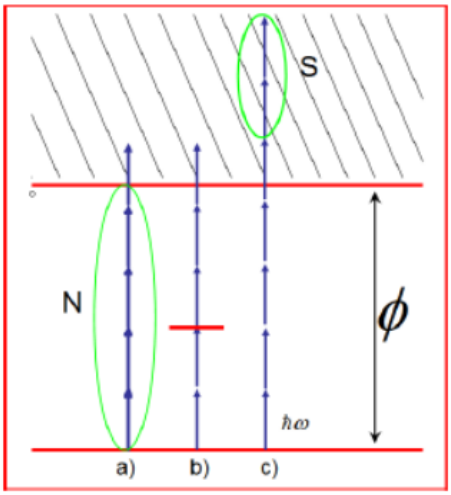

Figure 4.3: Schematic showing a) Multiphoton ionization b) REMPI and c) ATI

4.3.3 Tunnel ionization

There exists another pathway by which ionization occurs and unlike single and multiphoton ionizations, this is method is governed by the strength of the electric field of the laser. It is known as tunnel ionization and occurs when the potential barrier of the electron in the atom is distorted significantly by the intense laser field. An electron sitting in an atom can be viewed as shown in Figure 4.4. The electron will be bound to the atom within some finite, Coulombic potential well.

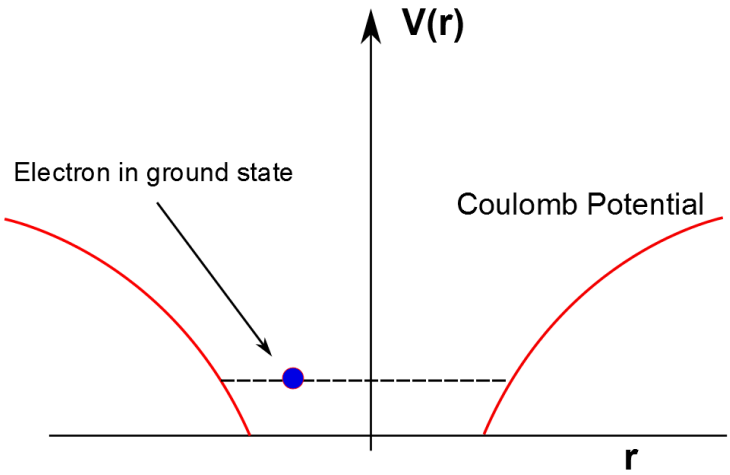

Figure 4.4: Schematic showing an electron sitting in an atomic potential.

The single and multiphoton photon descriptions that were provided above made no mention on how the electric field of the laser distorts the electric field between the electron and the nucleus. This is because multiphoton ionization dominates when the laser field is not strong enough to distort the Coulombic potential [13]. However, at intensities that can be reached by femtosecond lasers (10^{14} Wcm^{-2}), the electric field of the laser is comparable to the electric field between the electron and the nucleus. In this case, the Coulombic potential is perturbed by the strong oscillating electric field and the potential barrier holding the electron is lowered when the electric field reaches a maximum. If the electric field is strong enough, the potential barrier can

be lowered so much that the electron will tunnel through the barrier and appear in the continuum. Because of the oscillatory nature of the electric field, alternate sides of the barrier will be lowered during each half cycle of the laser field and so there is a probability of the electron tunneling through either side of the barrier. This is shown graphically in Figure 4.5.

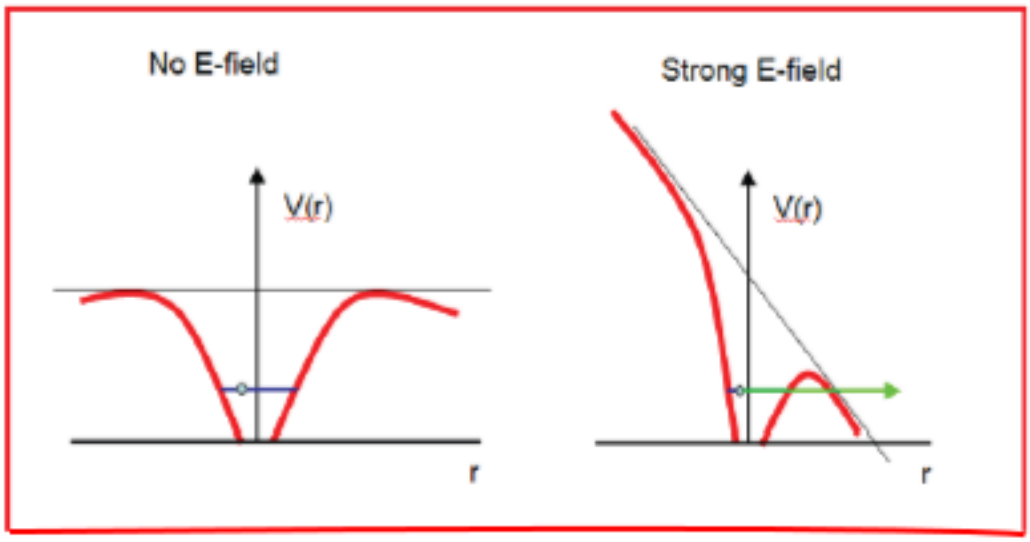

Figure 4.5: Tunnel ionization scheme

A paper by Keldysh [14], described a parameter which allows for the determination of whether tunel or multiphoton ionization will occur. The 'Keldysh parameter' is given in Equation 4.5.

$$\gamma = \omega \frac{\sqrt{2m_e I_p}}{eE} \tag{4.5}$$

where ω is the angular frequency of the laser field and I_p is the ionization of the atom when no laser field is present. E is the strength of the electric field of the laser which is related to the intensity by Equation 4.6:

$$I = \frac{cn\epsilon_o}{2}E^2 \tag{4.6}$$

A qualitative analysis of Equation 4.5 allows the following to be inferred. Firstly, the probability of tunnel ionization occuring will grow with an increasing electric field. This will push the value of the Keldysh parameter down and so tunnel ionization will dominate at low values. In fact, by comparison with experiment, the main conclusion from [14] is a scaling law that if $\gamma < 1$ then tunnel ionization will dominate. If $\gamma > 1$ then multiphoton ionization will dominate. It should also be noted that a low value of ω will also lower the value of γ and favour tunnel ionization. This can be viewed in the following way. The lower the frequency of the laser field, the longer the potential barrier will remain low and the greater the chance of the electron tunneling through to the continuum. In this way, a low frequency laser field will favour tunnel ionization.

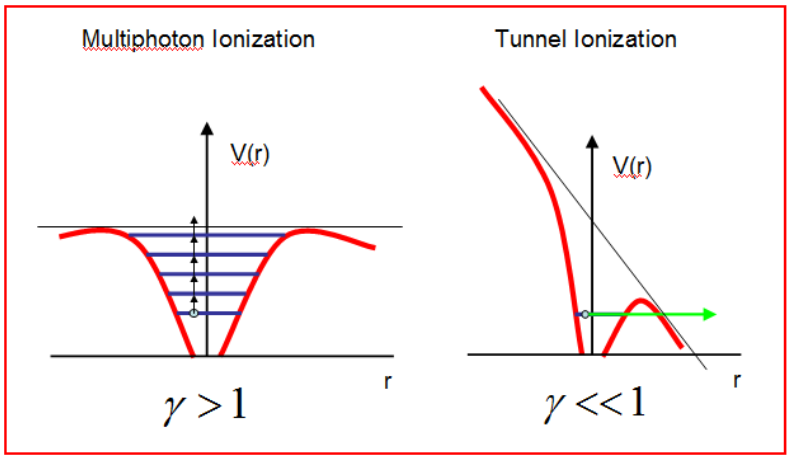

Figure 4.6: Schematic showing the multiphoton and tunnel ionization schemes.

4.3.4 Ionization of molecules

One difficulty in using models of atomic ionization to describe molecular ionization is that a molecule has a large number of degrees of freedom compared to an atom [15]. However a lot of the phenomena that have been observed in atomic ionization have also been observed in molecular ionization. These include: multiphoton ionization [16]; tunnel ionization [15] and above threshold ionization [17]. The extra degrees of freedom that a molecule has (rotational and vibrational) can lead to other phenomena that are not observable in atomic ionization such as fragmentation [18] and dynamic alignment [19].

As an example, angular distribution measurements for N_2 and O_2 targets revealed that the atomic fragments following ionization were strongly peaked in the laser field direction [20]. This study, which used 110 fs, 800 nm laser pulses attributed the strongly peaked atomic ion signal to a dipole alignment induced by the rising edge of the laser field before the field reaches sufficient intensity to ionize the molecule. In another study, the ionization signal of a molecular target was found to be enhanced by orders of magnitude and this was attributed to the laser field stretching the bonds beyond the equilibrium distance where the molecule is more easily ionized [15]. An extension of this phenomenon has been molecular explosion due to the mutual repulsion of the atomic components of the diatomic molecule. Similarly, the field may stretch the bonds of the molecule such that dissocation occurs but without the Coulombic explosion. This is known as 'field induced dissociation' [21].

At the time of the first multiphoton experiments on molecular targets [22], the results were explained using molecular orbit and molecular structure based models. These models found some success at moderate intensities ($10^{12} - 10^{13}$ Wcm^{-2}) where (for infrared laser fields) there is significant competition between the multiphoton and field ionization processes. However, at high intensities, these models break down because the field-molecule interaction becomes the dominant term in the Hamiltonian describing the system [23]. Models based on the Thomas-Fermi-Dirac atomic model

[24] had some further success in describing the ionization/dissociation/explosion processes at high laser intensities. The multielectron dissociative ionization (MEDI) [25] and the field induced Coulomb ionization (FICE) [26] models were introduced to explain the behaviour of the ionization and explosion of diatomic and small molecules [27]. Sophisticated theoretical treatments [23] and experimental techniques [28] have been developed in recent times to fully explain the behaviour of diatomic molecules in intense laser fields.

In this chapter, an effusive N_2 gas jet has been irradiated with laser pulses of duration 60fs at an intensity of 5×10^{14} Wcm^{-2}. The polarisation dependence of molecular and atomic fragment ionic components was studied. In the following sections, the experimental set up is described and following that, the experimental results are presented and discussed in the context of the already well established literature on this subject.

4.4 Experimental setup

The experimental setup used for the laser gas phase experiments in this work is shown in Figure 4.7. Three aluminium plates of diameter 40 mm are mounted onto a vacuum flange with threaded ceramic bars. The plates are then held in place using teflon nuts such that their position along the threaded bars can be set precisely. The plates are connected by the use of a vacuum feedthrough to high voltage power supplies with an operating range of 0-5 kV. The spectrometer is designed to maximise throughput while minimising contributions of ionization from outside the focal volume of the laser. With this in mind, a 4 mm hole was drilled through the repeller plate. An aluminium fitting of outer diameter 4 mm and inner diameter 1 mm is then inserted into the repeller plate. This fitting allows for PTFE tubing which is connected at the other end to a leak valve so that a narrow stream of gas can be pumped into the centre between the repeller and extractor plates. Both extractor plates have a 20 mm hole cut through the centre to allow high throughput. These holes are covered in fine tungsten mesh to ensure uniform electric field lines between the plates. The distance between the repeller and extractor plates is 5 mm. This distance was chosen to minimise contributions from outside the focal volume to the ionization signal [29]. The two extractor plates were separated by a distance of 10 mm. For all experiments, the second extractor plate was grounded at 0 V with respect to the vacuum chamber.

The three plates were mounted using threaded ceramic bars onto a CF-100 vacuum flange. The flange was then inserted into a Kurt J Lesker six way cross vacuum chamber. The entire system was evacuated with a 100 l/s turbo molecular pump to a typical base pressure of 3.5×10^{-8} mbar. Typical operating pressures, with gas in the chamber, were 1×10^{-6} mbar. The laser was focussed into the center of the gas jet using a 200 mm focal length plano convex lens through a vacuum window (see Figure 4.8). The beam was routed into the vacuum chamber using two mirrors such that the beam could be moved laterally along the gas flow direction and the lens was mounted on a high precision XYZ translation stage so that the position of the focus could be optimised for signal collection.

In the gas flow direction, a stainless steel CF-100 vacuum straight piece was

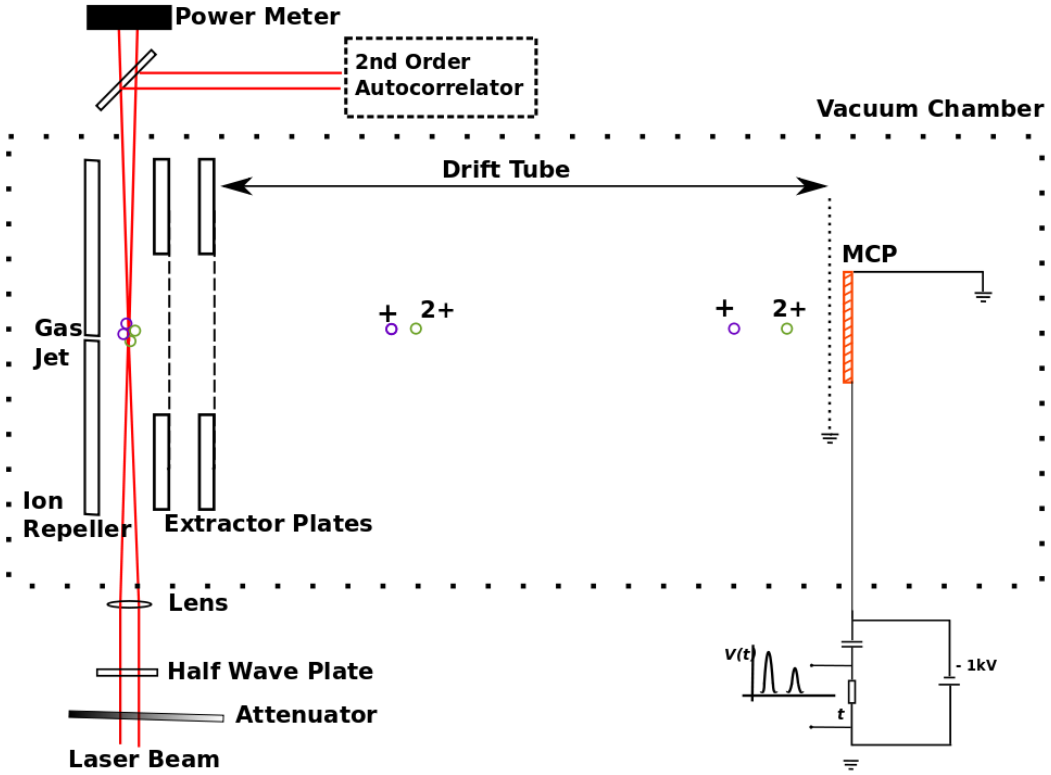

Figure 4.7: Experimental setup for the gas phase experiments in this work.

used to extend the six way cross and make a flight tube for the ions (of roughly 650 mm). At the other end, a home-made, single stage microchannel plate detector (with active area 27.8 mm) was mounted between two metallic ring electrodes onto a CF-63 vacuum flange which contained MHV and SHV feedthroughs to apply a bias to the channel plate. The channel plate configuration is shown in Figure 4.9. The ion signal was measured using a bias-tee arrangement (shown in Figure 4.10). The signal was measured on a Tektronix TDS3012, 300MHz bandwidth oscilloscope and then transferred to computer using a LabView acquisition programme.

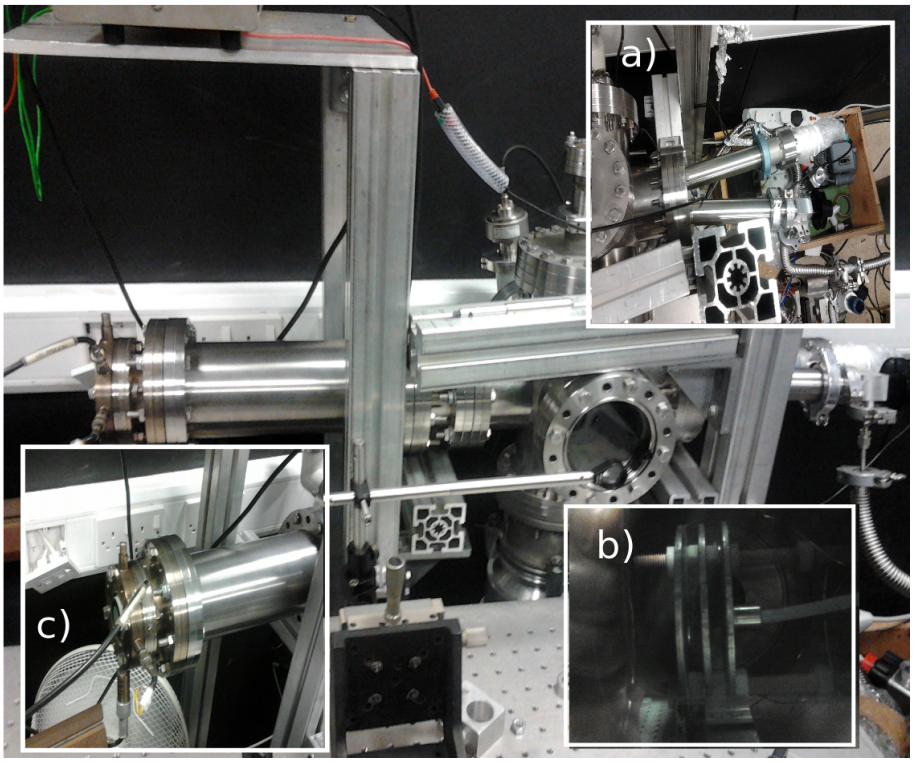

Figure 4.8: Photograph of TOF setup with inset a) gas inlet and voltage feedthrough, b) repeller and extractor plates, c) MCP detector.

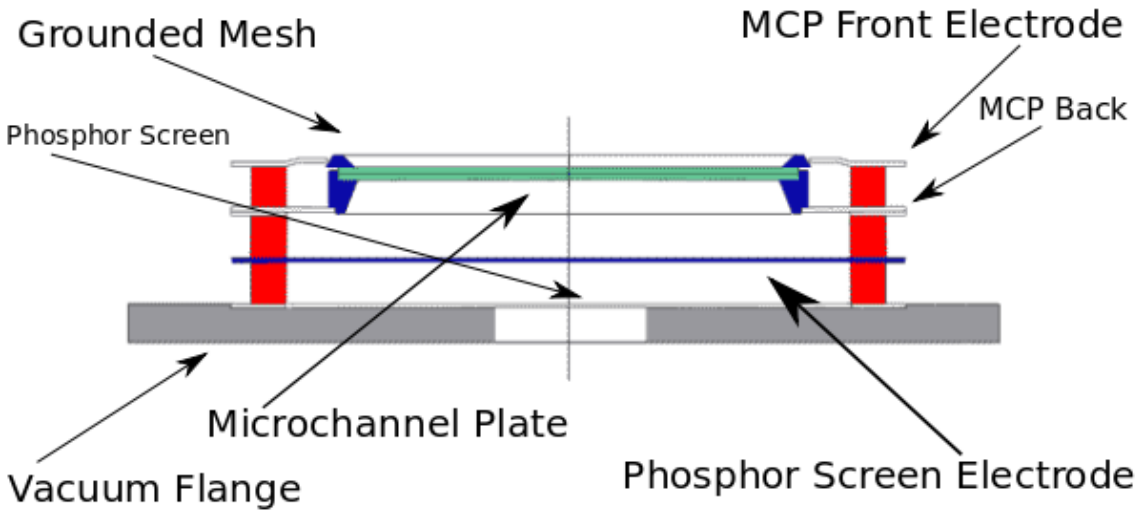

Figure 4.9: Schematic showing configuration of MCP. Adapted from [30]. A phosphor screen was included in the assembly but was not used for these experiments.

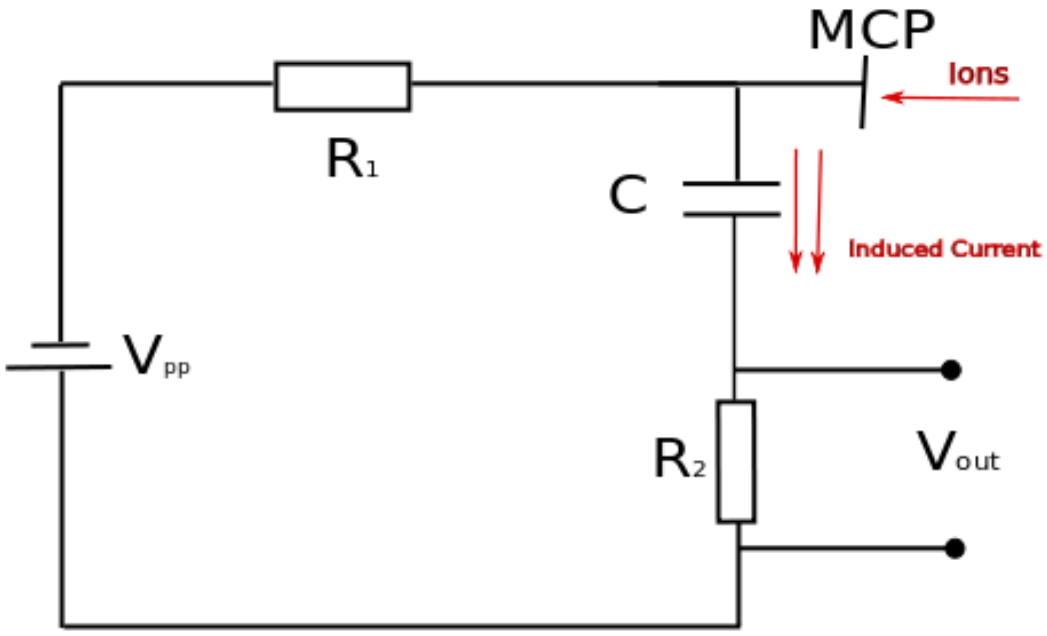

Figure 4.10: Schematic of MCP circuit. $R_1 = 100\ \Omega$, $R_2 = 50\ \Omega$, $C = 100$ nF

4.4.1 Calibration of instrument

Typical time-of-flight spectra for both argon (top) and nitrogen (bottom) gas are shown in Figure 4.11.

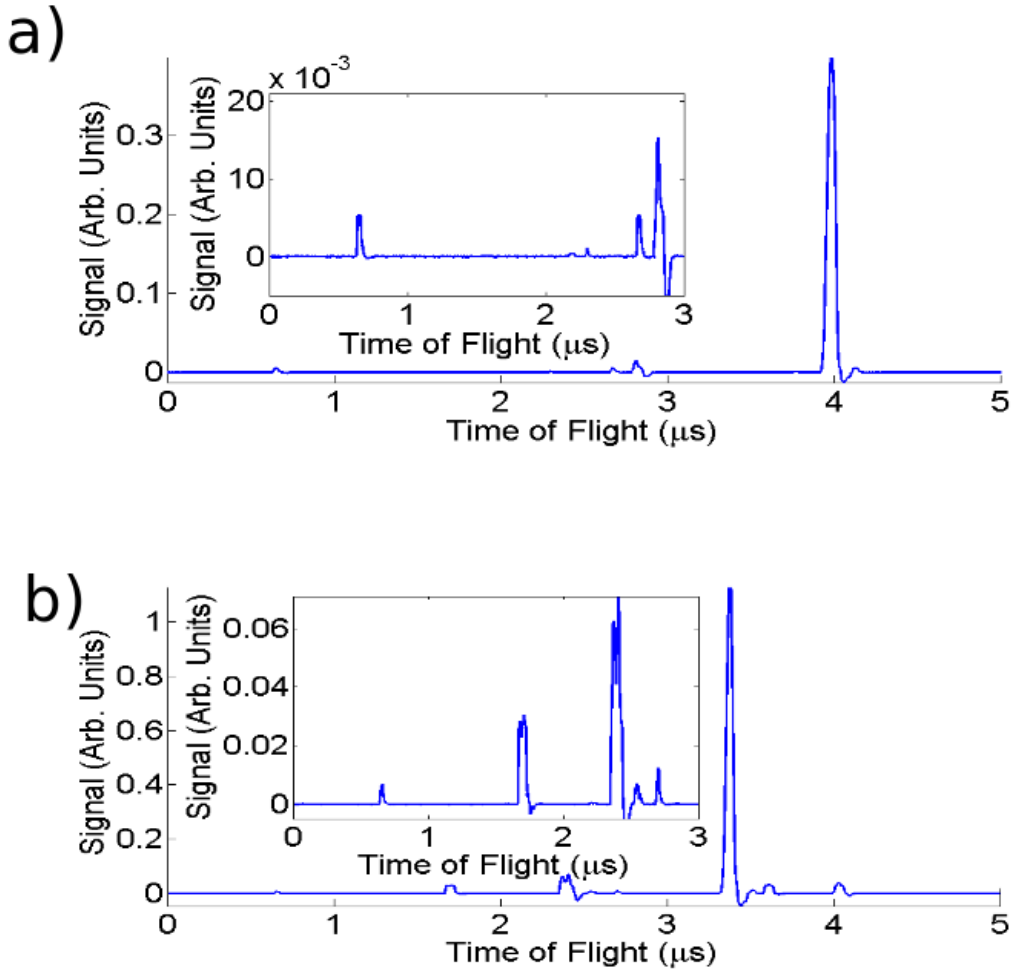

Figure 4.11: Typical time-of-flight signals obtained with the Wiley McLaren TOF spectrometer with a) argon and b) nitrogen. These were taken with both $V_s = 4.2$ kV and $V_d = 4.1$ kV to give an extraction field of 200 V/cm. The chamber pressure was 2×10^{-6} mbar.

In panel a) the peak at $\approx 4\ \mu s$ is assumed to be Ar^+ because it is the dominant peak, varies directly with gas pressure and is the slowest moving component in the TOF signal and therefore is assumed to be argon with the highest mass to charge ratio (i.e m/q = 39). In panel b) the peak at $\approx 3.5\ \mu s$ is assumed to be N_2^+. The peak that appears in both a) and b) at $\approx 0.7\ \mu s$ also appears in the absence of any input gas and is the fastest peak in both cases and so it is assumed to be H^+. These probable peaks are assigned their m/q values (39 for Ar^+, 28 for N_2^+ and 1 for H^+) and plotted against the square of their time of flight (because Equation 4.1 shows that the time of flight is proportional to the square root of the mass to charge ratio). Using these three as data points, a calibration curve to transform time into m/q is found by least squares fitting a function of the form.

$$\frac{m}{q} = AT^2 + B \tag{4.7}$$

Figure 4.12 shows a calibration curve for $V_s = 4.2$ kV, $V_d = 4.1$ kV. Also shown for comparison is a simulation of the TOF using the commercial SIMION software package.

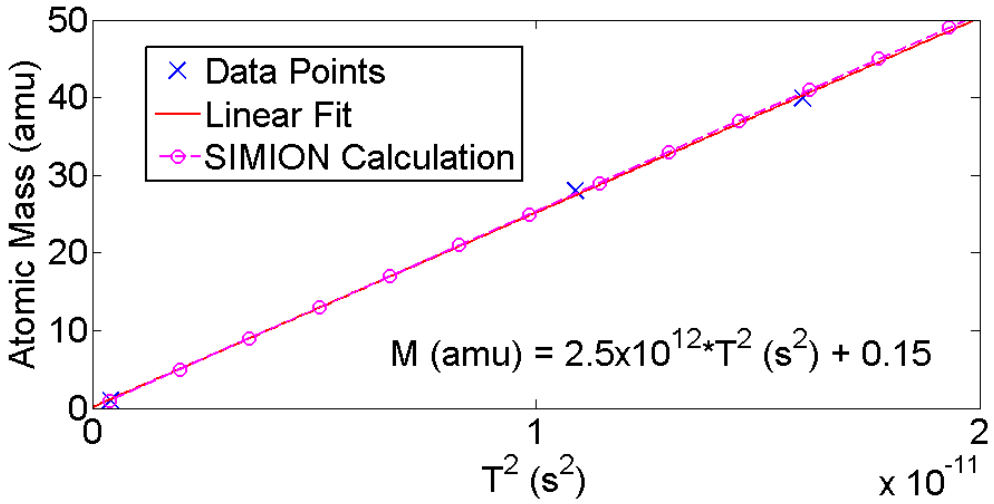

Figure 4.12: Calibration curve for the TOF using $V_s = 4.2$ kV, $V_d = 4.1$ kV

4.5 Results: Photoionization of nitrogen

4.5.1 Polarization studies

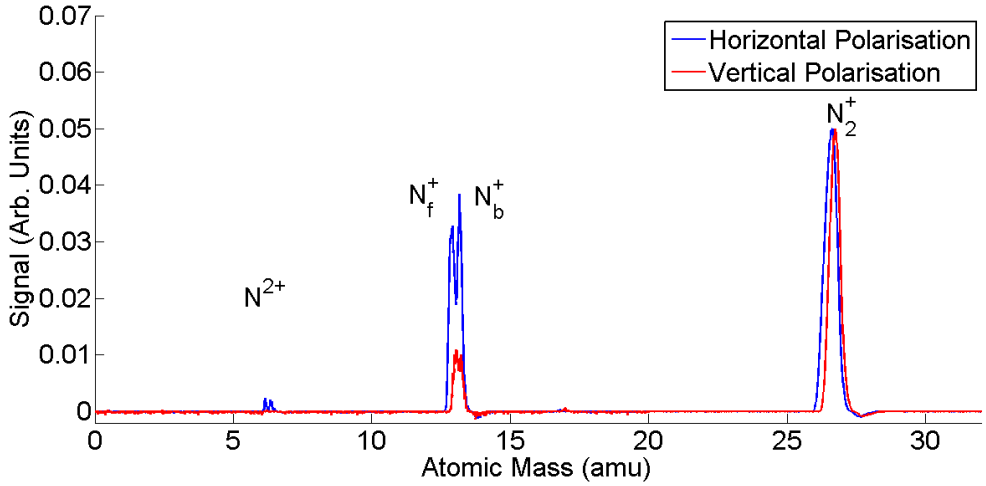

Figure 4.13: Time-of-flight spectra for orthogonal laser polarisations. Horizontal refers to polarisation along the TOF axis, vertical is perpendicular to the TOF axis.

Figure 4.13 shows time-of-flight spectra for two different linear laser polarisation states. Horizontal polarisation refers to the laser polarisation aligned along the TOF axis and vertical polarisation refers to laser polarisation aligned perpendicular to this axis. Figure 4.13 shows that the N_2^+ molecular ion remains relatively un-affected by the laser polarisation. The atomic ions (N^+, N^{2+} and N^{3+} (Figure 4.14)) all show polarisation dependent behaviour. For horizontal polarisation, the atomic ions appear to have a doublet structure consisting of two peaks disposed symmetrically either side of the mass value for that particular ion. This is an indication that the highly charged molecular ion explodes along the laser field direction into two fragments: a forward moving fragment and a backward travelling fragment. The backward travelling fragment is turned around by the electrostatic field between the repeller and extractor plates. The separation in time between the two peaks is indicative of the kinetic energy released in this explosion which is related to the

explosion pathway the molecule followed [31]. For now, the polarisation dependance of the atomic ion is only discussed.

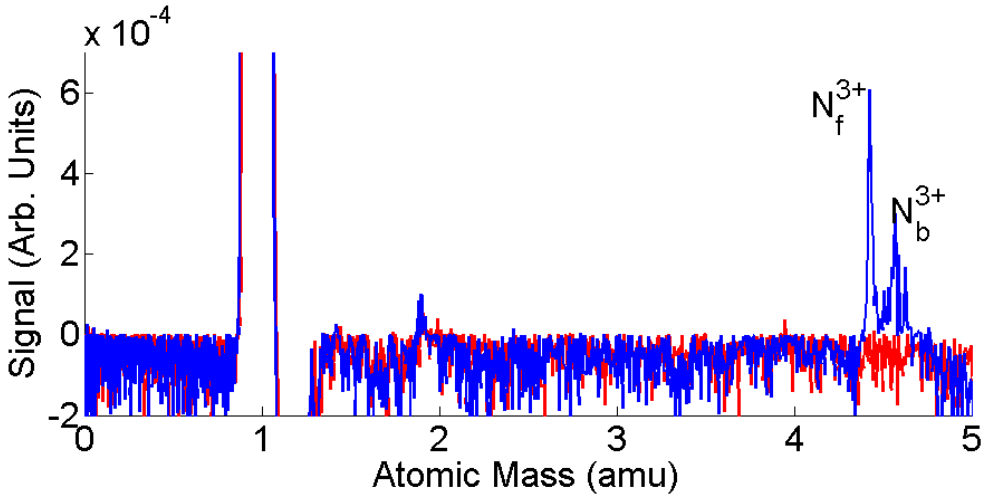

Figure 4.14: The N^{3+} region magnified to show the difference in the ionization signal between horizontal and vertical polarisations.

The polarisation of the laser was rotated through 180^o (where 0^o is horizontal polarisation). Because the time-of-flight detector remained stationary throughout the experiment, rotating the polarisation vector amounts to measuring the ion emission with respect to the laser polarisation vector. The angular distribution of the singly charged molecular ion, and the single, double and triple charged atomic ions (Figures 4.15 - 4.18). The isotropic emission of the molecular ion N_2^+ is consistent with previous studies [32]. The measured FWHM of the atomic ion emission for (N^+,N^{2+},N^{3+}) was $(83^o, 60^o, 50^o)$ which is close to previous measurements [32], [20] of Coulombic explosion of N_2 at similar laser intensities. For vertical polarisation, the signal goes to zero for both N^{2+} and N^{3+} (Figures 4.20 and 4.21) but a significant signal is still measured in the N^+ mass location. Upon closer inspection of the N^+ mass region (Figure 4.19), it is seen that for vertical polarisation, a single peak is visible whose location is at the centre of the split peak structure for horizontal polarisation. If both are created with the same kinetic energy, N^+ will appear at the same time as N_2^{2+} because both species have the same mass to charge ratio.

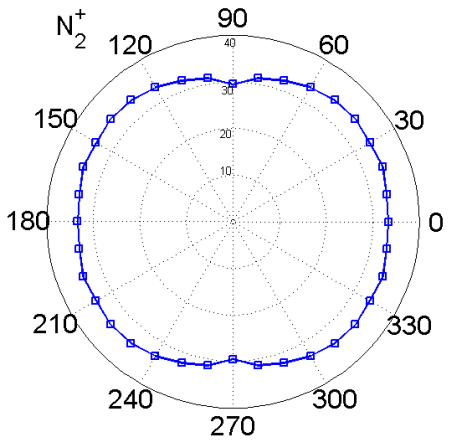

Figure 4.15: Angular distribution of the singly ionized molecule.

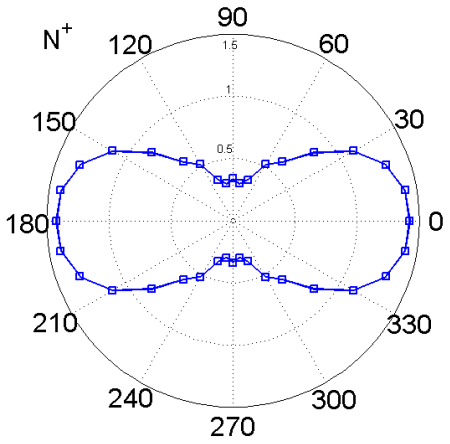

Figure 4.16: Angular distribution of the singly ionized atomic nitrogen.

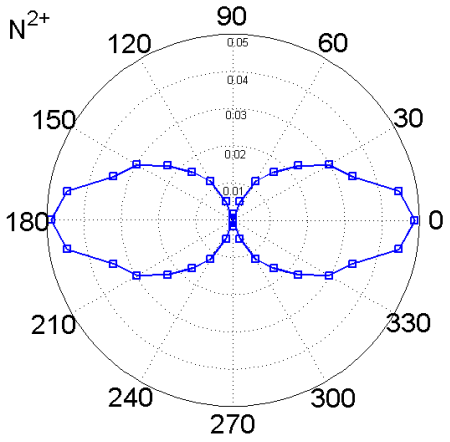

Figure 4.17: Angular distribution of the doubly ionized atomic nitrogen.

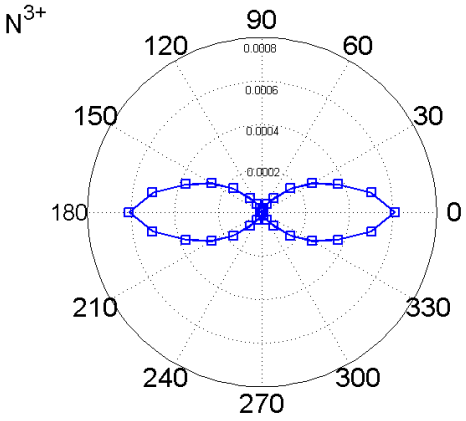

Figure 4.18: Angular distribution of the triply ionized atomic nitrogen.

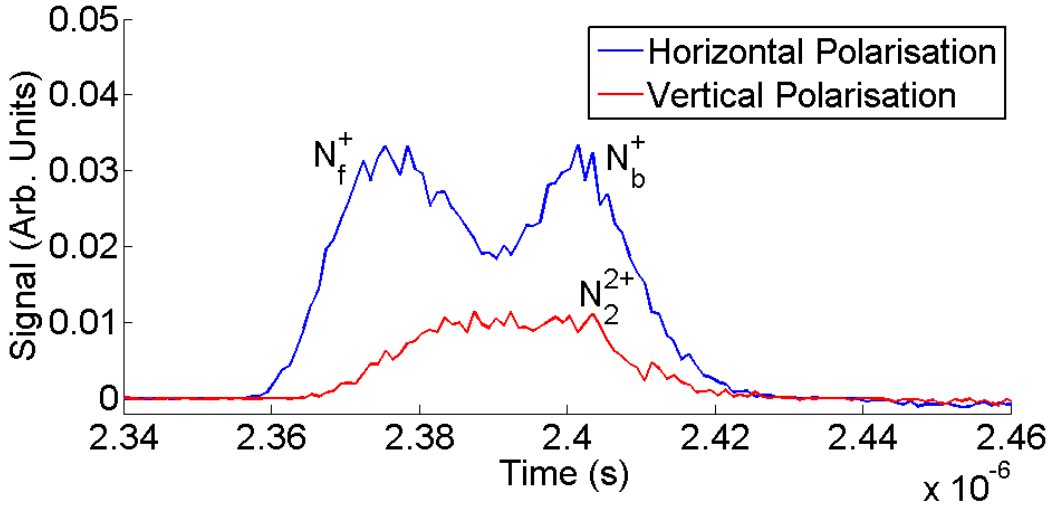

Figure 4.19: The N^+ atomic ion showing both horizontal and vertical polarisation. This shows that at horizontal polarisation the doubly charge molecular ion is visible together with the singly charge atomic ion from the explosion of the molecule.

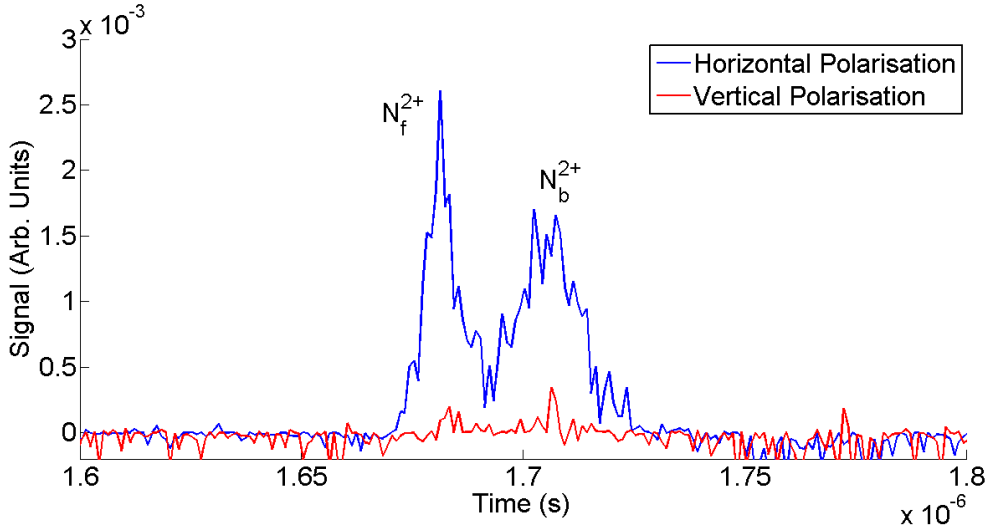

Figure 4.20: The N^{2+} atomic ion showing both horizontal and vertical polarisation. No residual molecular ion is visible at vertical polarisation.

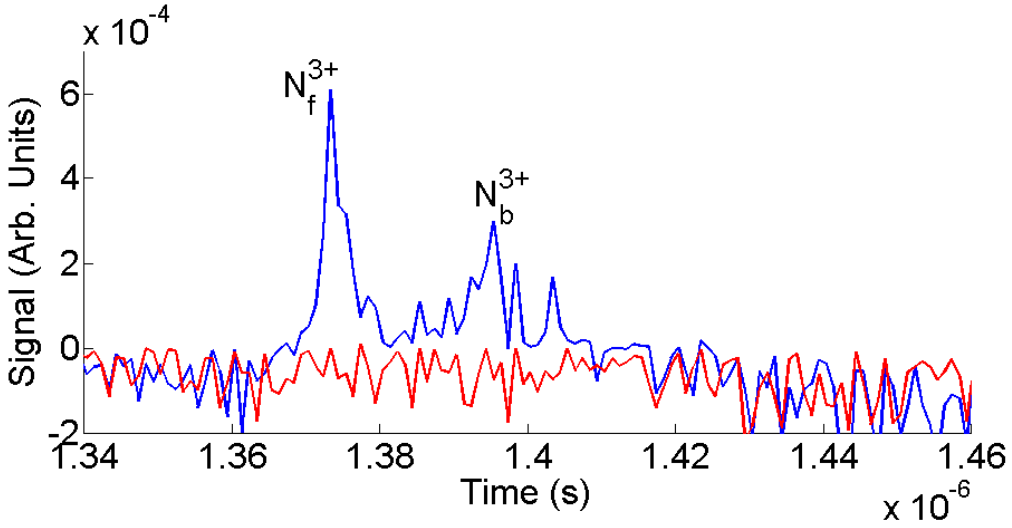

Figure 4.21: The N^{3+} atomic ion showing both horizontal and vertical polarisation.

Thus, it is suggested that in the region of the N^+ ion, the bi-modal structure visible at horizontal polarisation is a blend of both the doubly charged molecular ion and the singly charged atomic ion fragments from the Coulomb explosion process. At vertical polarisation then, only the residual doubly charged molecular ion is visible because the atomic fragments have exploded along the laser field direction and do not reach the detector. Following this argument, the N^{2+} peaks should appear superposed with the N_2^{4+} molecular ion and similarly the N^{3+} atomic fragments should appear with the N_2^{6+} molecular ion. However, at vertical polarisation, no signal could be detected for molecular ions of higher charge than 2+. One possible explanation, and indeed the argument presented in other studies of this kind is that highly charged molecular ions are not stable enough to remain intact and will undergo either dissociation or explosion.

In previous studies of this kind, two arguments have been put forward for the observed anisotropic distribution of the atomic fragments in molecular ionization. Firstly, the effusive gas jet is considered to be an ensemble of randomly oriented molecules. The 'geometric alignment' theory suggests that the ion yield is proportional to alignment between the electric field vector of the laser and the linear molec-

ular axis [19]. According to the field ionization, Coulomb explosion (FICE) model of molecular ionization [26], the threshold intensity for a given explosion pathway (for example $N_2^{2+} \rightarrow N^+ + N^+$) depends on the angle between the laser field and the linear molecular axis. In fact, there is a finite probability that even when the linear molecular axis is perpendicular to the field, explosion will occur. Because no double peak structures are visible even at these high intensities, geometric alignment is unlikely to be the reason behind the observed anisotropy of the atomic ions.

Another explanation for the anisotropy is found in multiple previous studies on this matter [32, 20]. As the laser field reaches its peak, the molecular ion becomes ionized and will hence gain a dipole moment. Post ionization but pre-dissociation / explosion, the molecule will begin to align to the laser field. The strength of the induced dipole moment (and hence the strength of the alignment) will be proportional to the charge state. Hence, the higher charge state atomic fragments will be more strongly aligned to the laser field direction. This effect explains both the anisotropy and the narrowing of the angular distribution in the peaks corresponding to the atomic fragments.

4.6 Summary and outlook

In summary, a linear time-of-flight device has been built and the results of [32] have been reproduced to illustrate the operation of the device. The angular distribution of N_2 molecules has been studied using a half wave plate and found to be isotropic. It is found that when the laser polarisation is along the time-of-flight axis, a split peak doublet appears at mass to charge values corresponding to the first three atomic charge states of nitrogen. It is proposed then that this doublet structure is formed by explosion or dissociation along the laser axis. The angular distribution of the atomic ions is found to be highly peaked along the laser direction and, the higher the charge state, the more strongly peaked the signal is in the laser field direction. By qualitively comparing these results to previous studies and to classical models such as the FICE model that describes laser interaction with molecules, it is concluded that the anisotropy is the result of dynamic alignment of the ionized molecule before the

fragmentation occurs. The measured angular distributions of the atomic fragments are found to be in excellent agreement wtih previous studies.

While it is hard to see scope for unexplored research of in the ionization of nitrogen at these intensity ranges given the exhaustive supply of literature available on the subject, it is noted that no reports could be found where a systematic study of the dissociation of nitrogen is studied as a function of photon energy where the pulse duration is less than 100 fs. The N^+ atomic fragments presented in the section above were assumed to be from a symmetric explosion pathway $N_2^{2+} \rightarrow N^+ + N^+$. However, assymmetric explosion pathways are possible (for example $N_2^{3+} \rightarrow N^{2+} + N^+$. The long established technique of covariane mapping [33] allows for the determination of the correlation between different atomic fragments and so the specific explosion pathway can be determined.

According to the Thomas-Fermi-Dirac model of ionization of nitrogen, initial ionization occurs on the first peak or trough of the laser field [24]. The internuclear separation will increase due to Coulombic repulsion of the two ions. As the field oscillates, charge is transferred between the two ions as the ions move apart and at the point of dissociation, charge imbalance may occur leading to an asymmetric fragmentation. However, if the laser field contains many optical cycles, the charge imbalance will be averaged out and so a symmetric fragmentation is preferred. Thus, a study of this process with three different wavelengths (800 nm, 400 nm, 266 nm) at the same intensity and pulse duration will allow for the system to be studied with laser fields that have different numbers of optical cycles while everything else remains constant. If this study is performed using the co-variance mapping techique, insights could be gained into the nature of this charge transfer as the field oscillates.

Converting the TOF presented here to one which can be used to correlate the atomic fragment patterns to each other or their parent ion would be relatively simple. The main obstacle would be fast acquisition to allow for single shot data collection.

Bibliography

[1] W.C. Wiley and I.H. Mclaren. Time-of-flight mass spectrometer with improved resolution. *Review of Scientific Instruments*, **26**(12):1150–1157, 1955.

[2] F. Mller. Johann wilhelm hittorf and the material culture of nineteenth-century gas discharge research. *Br J Hist Sci.*, **44**(161):211, 2011.

[3] J.J. Thomson. Cathode rays. *Phil. Mag.*, **44**:293, 1897.

[4] F.W. Aston. The mass-spectra of chemical elements. **48**:707, 1919.

[5] A. Brown. The Neutron and the Bomb: a Biography of Sir James Chadwick. Oxford University Press, 1997.

[6] G.J. Tallents. Operation of a 45-degree parallel-plate electrostatic analyzer in laser-produced plasma studies. *Journal of Physics E-Scientific Instruments*, **11**(8):769–772, 1978.

[7] L. Belshaw and F. Calegari and M.J. Duffy and A. Trabattoni and L. Poletto and M. Nisoli and J.B. Greenwood. Observation of ultrafast charge migration in an amino acid. *Journal of Physical Chemistry Letters*, **3**(24):3751–3754, 2012.

[8] C.R. Calvert and L. Belshaw and M.J. Duffy and O. Kelly and R.B. King and A.G. Smyth and T.J. Kelly and J.T. Costello and D.J. Timson and W.A. Bryan and T. Kierspel and P. Rice and I.C.E. Turcu and C.M. Cacho and E. Springate and I.D. Williams and J.B. Greenwood. Liad-fs scheme for studies of ultrafast laser interactions with gas phase biomolecules. *Physical Chemistry Chemical Physics*, **14**(18):6289–6297, 2012.

[9] H. Zenk. Ionization by quantized electromagnetic fields: The photoelectric effect. *Reviews in Mathematical Physics*, **20**(4):367–406, 2008.

[10] G. Mainfray and C. Manus. Multiphoton ionization of atoms. *Reports on Progress in Physics*, **54**(10):1333–1372, OCT 1991.

[11] P. Lambropoulos. Theory of multiphoton ionization - near-resonance effects in 2-photon ionization. *Physical Review a*, **9**(5):1992–2013, 1974.

[12] P. Agostini and F. Fabre and G. Mainfray and G. Petite and N.K. Rahman. Free-free transitions following 6-photon ionization of xenon atoms. *Physical Review Letters*, **42**(17):1127–1130, 1979.

[13] M.V. Ammosov and N.B. Delone and V.P. Krainov. Tunnel ionization of complex atoms and atomic ions in a varying electromagnetic-field. *Zhurnal Eksperimentalnoi i Teoreticheskoi Fiziki*, **91**(6):2008–2013, 1986.

[14] L.V. Keldysh. Ionization in field of a strong electromagnetic wave. *Soviet Physics Jetp-Ussr*, **20**(5):1307, 1965.

[15] T.D.G. Walsh and F.A. Ilkov and J.E. Decker and S.L. Chin. The tunnel ionization of atoms and diatomic and triatomic-molecules using intense 10.6 mu-m radiation. *Journal of Physics B-Atomic Molecular and Optical Physics*, **27**(16):3767–3779, 1994.

[16] C. Cornaggia and P. Hering. Laser-induced non-sequential double ionization of small molecules. *Journal of Physics B-Atomic Molecular and Optical Physics*, **31**(11):L503–L510, 1998.

[17] A. Gazibegovic-Busuladzic and E. Hasovic and M. Busuladzic and D.B. Milosevic and F. Kelkensberg and W.K. Siu and M.J.J. Vrakking and F. Lepine and G. Sansone and M. Nisoli and I. Znakovskaya and M.F. Kling. Above-threshold ionization of diatomic molecules by few-cycle laser pulses. *Physical Review a*, **84**(4):043426, 2011.

[18] P. Graham and X. Fang and K.W.D. Ledingham and R.P. Singhal and T. McCanny and D.J. Smith and C. Kosmidis and P. Tzallas and A.J. Langley and P.F. Taday. Unusual fragmentation patterns from the dissociation of some small molecules. *Laser and Particle Beams*, **18**(3):417–432, 2000.

[19] J.H. Posthumus and J. Plumridge and M.K. Thomas and K. Codling and L.J. Frasinski and A.J. Langley and P.F. Taday. Dynamic and geometric laser-induced alignment of molecules in intense laser fields. *Journal of Physics B-Atomic Molecular and Optical Physics*, **31**(13):L553–L562, 1998.

[20] J. Huang and C. Wu and N. Xu and Q. Liang and Z. Wu and H. Yang Q. Gong. Field-induced alignment of oxygen and nitrogen by intense femtosecond laser pulses. *Journal of Physical Chemistry a*, **110**(34):10179–10184, 2006.

[21] P. Dietrich and P.B. Corkum. Ionization and dissociation of diatomic-molecules in intense infrared-laser fields. *Journal of Chemical Physics*, **97**(5):3187–3198, 1992.

[22] L.J. Frasinski and K. Codling and P. Hatherly and J. Barr and I.N. Ross and W.T. Toner. Femtosecond dynamics of multielectron dissociative ionization by use of picosecond laser. *Physical Review Letters*, **58**(23):2424–2427, 1987.

[23] M. Lezius and V. Blanchet and D.M. Rayner and D.M. Villeneuve and A. Stolow and M.Y. Ivanov. Nonadiabatic multielectron dynamics in strong field molecular ionization. *Physical Review Letters*, **86**(1):51–54, 2001.

[24] M. Brewczyk and L.J. Frasinski. Thomas-fermi-dirac model of nitrogen molecules ionized by strong laser fields. *Journal of Physics B-Atomic Molecular and Optical Physics*, **24**(13):L307–L313, 1991.

[25] C. Cornaggia and J. Lavancier and D. Normand and J. Morellec and P. Agostini and J.P. Chambaret and A. Antonetti. Multielectron dissociative ionization of diatomic-molecules in an intense femtosecond laser field. *Physical Review A*, **44**(7):4499–4505, 1991.

[26] J. H. Posthumus. The dynamics of small molecules in intense laser fields. *Reports on Progress in Physics*, **67**(5):623–665, 2004.

[27] Z.B. Walters and O. Smirnova. Attosecond correlation dynamics during electron tunnelling from molecules. *Journal of Physics B-Atomic Molecular and Optical Physics*, **43**(16):161002, 2010.

[28] A. Hishikawa and A. Iwamae and K. Hoshina and M. Kono and K. Yamanouchi. Coulomb explosion dynamics of n-2 in intense laser field by mass-resolved momentum imaging. *Chemical Physics*, **231**(2-3):315–329, 1998.

[29] S. Larochelle and A. Talebpour and S.L. Chin. Non-sequential multiple ionization of rare gas atoms in a ti : Sapphire laser field. *Journal of Physics B-Atomic Molecular and Optical Physics*, **31**(6):1201–1214, 1998.

[30] http://www.sciner.com/mcp/mcp-assemblies.htm.

[31] C. Cornaggia. Ultrafast coulomb explosion imaging of molecules. *Laser Physics*, **19**(8):1660–1670, 2009.

[32] C.Y. Wu and H.Z. Ren and T.T. Liu and R. Ma and H. Yang and H.B. Jiang and Q.H. Gong. Field-induced ionization and coulomb explosion of nitrogen. *Applied Physics B-Lasers and Optics*, **75**(1):91–96, 2002.

[33] L.J. Frasinski and K. Codling and P.A. Hatherly. Covariance mapping - a correlation method applied to multiphoton multiple ionization. *Science*, **246**(4933):1029–1031, NOV 24 1989 1989.

Chapter 5

Summary and outlook

To summarise, this project can be broadly described as being concerned with performing preliminary experiments in a new laboratory facility in DCU. The project can be further catergorised into three areas: Laser characterisation; Ablation of Solids; Ionization of Gases.

Chapter two introduced and described the physics behind lasing in general, and ultrafast lasers in particular. A detailed description of the mathematics of autocorrelation was given and a design for a cost-effective interferometric autocorrelator was given. The corresponding prototype was tested and there was evidence to suggest that interferometric autocorrelation could be performed using a system that contained no moving parts and utilized largely off-the-shelf, cost effective components. The design consisted of a Wollaston prism which acted as a beam splitter to generate two diverging, orthogonally polarised wavefronts. These wavefronts were re-polarised such that the electric field vectors were aligned and then imaged onto a CMOS array which was coated with an IR-red blocking filter. In this way, the detector was blind to 800 nm radiation but could detect any non-linear interactions that took place in the detector. It was proposed that two photon fluorescence took place inside the IR filter in front of the camera and this was detected by the CMOS arrray. The CMOS array showed a strong non-linear dependence on modelocked laser light across a wide range of intensities. The detector's reponse to 800 nm CW radiation was two orders

of magnitude less. The resulting signal was found to have a peak to background ratio of 7:1 which is very close to the theoretical 8:1 expected according to the mathematical foundations of autocorrelation.

.

Chapter three was concerned with the ablation of a silicon target with an intense ultrafast laser. A history of ultrafast laser ablation was given as well as a detailed description of the operation of a Langmuir probe. Langmuir probe measurements were performed to determine the expansion characteristics of the plume as well as the electron temperature and density. It was found that at high laser fluences, a bimodal structure was visible in both the ion and electron signals. It was demonstrated through fluence measurements that the low KE feature was thermal in nature in that it obeyed the two temperature prediction of two sub-linear regions from which the ablation threshold can be determined. Angle resolved measurements revealed that while the ions are emitted in a narrow cone about the target normal, the electrons are emitted over a wider distribution. Polarisation measurements were also made and from the study of how the ions behaved as a function of polarisation, it was discovered that resonance absorption was heavily dependent on laser intensity and wavelength. The electron behaviour with different polarisation suggested the possiblity of electrostatic potentials being created in the plasma plume which lowers the electrical conductivity of the plasma. Temperature and density analysis of the plume revealed evidence of a double layer formation, but as well as that, there was evidence to suggest that the plume was made up of a multi-fluid structure. Comparisons of Langmuir probe measurments at different probe-target distances revealed that indeed, under certain conditions a plasma which contains multiple electron components is possible. This was discussed in the context of double layer formation in the plasma plume.

While the results are interesting given how they pertain to a set of intensity values that are perhaps of interest to the pulsed laser deposition community, there are many more experiments to perform which could further support or refute the ideas presented in this thesis. Firstly, a complete angle resolved, I-V curve dataset for both S and P polarisations will give further insight into the apparent formation of

a double layer within the plume. A polarisation study of the electrons with different targets would reveal more about the curious nature of how the Si electrons appeared to behave with different polarisations.

Chapter four discussed the construction of a linear time of flight apparatus. Experiments on the explosion of N_2 molecular ions was reported and found to be in good agreement with previous literature values. There is scope for a systematic study of these explosion pathways as a function of photon energy. Similarly, an aperture could be installed just before the drift tube which would limit the detection to a single intensity slice. Then, ionization rates and dissocation pathways could be unambiguously determined without contributions from outside the laser focus.